2017

ENHANCING CONSERVATION WITH HIGH RESOLUTION PRODUCTIVITY DATASETS FOR THE CONTERMINOUS UNITED STATES

Nathaniel Paul Robinson

ENHANCING CONSERVATION WITH HIGH RESOLUTION PRODUCTIVITY DATASETS FOR THE CONTERMINOUS UNITED STATES

By

NATHANIEL PAUL ROBINSON

B. S., Wheaton College, Wheaton, IL, 2004
M. S., University of Montana, Missoula, MT, 2009

Dissertation

presented in partial fulfillment of the requirements
for the degree of

Doctor of Philosophy
in Forest and Conservation Sciences

The University of Montana
Missoula, MT

December 2017

Approved by:

Scott Whittenburg, Dean of The Graduate School
Graduate School

Dr. Brady W. Allred, Chair
Forest Management

Dr. Stephen F. Siebert
Forest Management

Dr. Steven W. Running
Ecosystem and Conservation Sciences

Dr. Mark Hebblewhite
Wildlife Biology Program

Dr. Hugh S. Robinson
Wildlife Biology Program

Dr. Anna E. Klene
Geography

Robinson, Nathaniel, Ph.D., Autumn 2017 Forest and Conservation Sciences

High resolution GPP and NPP for the conterminous United States

Chairperson: Brady W. Allred

Human driven alteration of the earth's terrestrial surface is accelerating through land use changes, intensification of human activity, climate change, and other anthropogenic pressures. These changes occur at broad spatio-temporal scales, challenging our ability to effectively monitor and assess the impacts and subsequent conservation strategies. While satellite remote sensing (SRS) products enable monitoring of the earth's terrestrial surface continuously across space and time, the practical applications for conservation and management of these products are limited. Often the processes driving ecological change occur at fine spatial resolutions and are undetectable given the resolution of available datasets. Additionally, the links between SRS data and ecologically meaningful metrics are weak. Recent advances in cloud computing technology along with the growing record of high resolution SRS data enable the development of SRS products that quantify ecologically meaningful variables at relevant scales applicable for conservation and management. The focus of my dissertation is to improve the applicability of terrestrial gross and net primary productivity (GPP/NPP) datasets for the conterminous United States (CONUS).

In chapter one, I develop a framework for creating high resolution datasets of vegetation dynamics. I use the entire archive of Landsat 5, 7, and 8 surface reflectance data and a novel gap filling approach to create spatially continuous 30 m, 16-day composites of the normalized difference vegetation index (NDVI) from 1986 to 2016. In chapter two, I integrate this with other high resolution datasets and the MOD17 algorithm to create the first high resolution GPP and NPP datasets for CONUS. I demonstrate the applicability of these products for conservation and management, showing the improvements beyond currently available products. In chapter three, I utilize this dataset to evaluate the relationships between land ownership and terrestrial production across the CONUS domain.

The main results of this work are three publically available datasets: 1) 30 m Landsat NDVI; 2) 250 m MODIS based GPP and NPP; and 3) 30 m Landsat based GPP and NPP. My goal is that these products prove useful for the wider scientific, conservation, and land management communities as we continue to strive for better conservation and management practices.

TABLE OF CONTENTS

LIST OF TABLES

Table 2.4: Pearson's r-value, RMSE, bias, and mean absolute bias (MAB) between GPP_{M250} and GPP_{L30} and CONUS flux tower GPP aggregated by land cover. Results include GPP calculated with both the original MOD17 algorithm parameters and optimized parameters produced in this paper. The optimized parameters for both datasets yielded better statistics across all land cover classes except shrublands Pearson's r value.

Table 2.5: Pearson's r-value, RMSE, bias and mean absolute bias (MAB) between flux tower GPP and the MOD17 product, GPP_{M250} and GPP_{L30}. These comparisons use 8-day mean GPP, matching the temporal granularity of the MOD17 product. **Bold** indicates the best statistic.

Table 2.6: Total annual NPP for CONUS in Pg (10^{15} g) carbon for MOD17, NPP_{M250} and NPP_{L30}. Results are shown aggregated across all land cover as well for each class individually.

Table 2.S1: Flux Tower Info

Table 2.S2: Total annual NPP for CONUS in Pg (10^{15} g) carbon for MOD17, NPP_{M250} and NPP_{L30} calculated with respiration as a fixed ratio of GPP and with the MOD17 procedure. Results are shown aggregated across all land cover as well for each class individually.

Table 2.S3: Biome specific properties used in the MOD17 algorithm (Running & Zhao, 2015).

Table 2.S4: Reclassification scheme for National Land Cover Database (NLCD). Grassland and pasture/hay are combined as grassland.

Table 3.1: Total production, average productivity, trends and p-values, and PDE for forests and rangelands across CONUS and for level I ecoregions.

LIST OF FIGURES

composite is processed on the fly and users are notified via email when it is ready to download.

Figure 1.6 The distribution of Pearson correlation coefficients between MOD13Q1 NDVI and Landsat NDVI for each land cover class.

Figure 1.7 Time series of 30m Landsat NDVI and 250m MOD13Q1 NDVI time series from 2013 to 2015, separated by land cover class. After April 2013, the Landsat NDVI time series include data from both Landsat 7 and 8, while before April 2013 they included just Landsat 7 data. Each time series is from a single point, within a homogenous area (i.e., pixels where both Landsat and MOD13Q1 represent the same land cover), sampled at a location indicative of the major land cover classes.

Figure 1.8 (a) Pixel locations in central Washington, USA. Landsat derived NDVI can provide increased detail in heterogeneous landscapes. The difference in pixel shape is due to native projections being transformed to a common projection. (b) Chart for 2015 of a Landsat derived NDVI and MOD13Q1 NDVI time series.

Figure 1.S1 (a) Map of phenocam locations.

Figure 1.S2 (a) Landsat 5 edge removal illustration.

Figure 2.1: Flowchart of the MOD17 GPP and NPP algorithms. The main components are A) GPP; B) maintenance respiration; and C) annual NPP. Adapted from the MOD17 user's guide (Running & Zhao, 2015).

Figure 2.2: GPP_{M250} (A & B) and GPP_{L30} (C & D) relative to GPP_{Flux} (FLUXNET2015, CONUS only). GPP_{250} GPP_{L30} in plots A and C are calculated with the original MOD17 BPLUT parameters, while GPP in B and D use parameters optimized for CONUS and demonstrate improvement.

Figure 2.3: GPP_{M250} (left column) and GPP_{L30} (right column) relative to GPP_{Flux} (FLUXNET2015, CONUS only), aggregated by land cover.

Figure 2.4: Time series of 8-day GPP_{Flux}, MOD17 GPP (500 m), GPP_{M250} (250 m) and GPP_{L30} (30 m) from towers representing the range of land cover classes. Data from two cropland towers (C and D) are plotted demonstrating the range of GPP variability across cropland sites. The GPP_{M250} and GPP_{L30} datasets correspond well with GPP_{Flux} at the ARM flux tower (C; Oklahoma, wheat and soybean) while underestimate GPP compared to GPP_{Flux} at the NE1 flux tower(D; Nebraska, irrigated corn).

Figure 2.5: Time series of NPP anomalies for the MOD17 (500 m), NPP_{M250} (250 m), and NPP_{L30} (30 m) datasets. All three datasets track the interannual variability of NPP with similar magnitudes. Anomalies are calculated as the percent difference from the long-term mean for each dataset and land cover class.

Figure 2.6: Maps of 2010 annual NPP across CONUS at levels of decreasing resolution: (A) NPP_{L30} at 30 m; (B) NPP_{M250} at 250 m; and (C) the MOD17 product at 500 m. Higher resolution reveals greater spatial variability of NPP.

Figure 2.7: Boxplots showing pre- and post-fire NPP dynamics (anomalies) relative to burn severity for a grassland fire (top panels; Lund fire, North Dakota) and an evergreen

needleleaf forest fire (bottom panels; Horse Creek fire, Wyoming) using the MOD17 (500 m), NPP_{M250} (250 m), and NPP_{L30} (30 m) products. The nuances of fire-productivity relationships–increased variability between NPP and burn severity, and the resulting responses of NPP to burn severity, are detected using the medium resolution NPP_{M250} and NPP_{L30} products but are lost with the coarser resolution MOD17 product.

Figure 2.8: Annual NPP for an energy site using the MOD17 product (500 m), NPP_{M250} (250 m), and NPP_{L30} (30 m) datasets. Losses in NPP due the discrete disturbance are reflected in the finer resolution NPP_{L30} dataset , but are absent in the coarser resolution datasets. The time series also demonstrates the historical data available using the full Landsat archive. The relative differences in pixel sizes are shown in the right panel.

Figure 2.9: The GPP/NPP_{L30} datasets permit the tracking of primary production change across broad spatiotemporal scales. Here, annual NPP for a 60 m buffer around Maggie Creek, Nevada is plotted. Restoration activities occurred in 1994 (vertical black line). The pre- and post-restoration mean NPP (dashed lines) along with 95% confidence intervals are shown.

Figure 2.S1: Illustration of the linear ramp functions for scaling minimum temperature and vapor pressure deficit.

Figure 2.S2: Map of individual flux tower sites used for the GPP parameter optimization. The numbers correspond with individual flux towers described in Table 2.S1.

Figure 2.S3: (A) The NLCD within a 1 km buffer of the Wi4 flux tower located in Northern Wisconsin, demonstrating heterogeneous land cover cover at 30 m resolution.

(B) Only FPAR values from pixels of the dominant land cover (evergreen needleleaf forest for this tower) are used in the parameter optimization process.

Figure 2.S4: Time series of NPP anomalies including the MODIS and Landsat derived NPP calculated with respiration as a fixed ratio (50%) of GPP. Using the fixed ratio approach, large anomalies in NPP are reduced for both the MODIS and Landsat derived datasets.

Figure 3.1: Ownership categories across CONUS (a.) and average total annual production from 1993 to 2016 (b.). There is a distinct inverse longitudinal pattern of public land acreage and total production.

Figure 3.2: Time series plots of total production and average productivity across CONUS from 1993 to 2016 for land cover classes combined (a. and b.), forest classes (c. and d.), and rangeland classes (e. and f.). Total production and average productivity on private lands is higher in all cases. Despite noticeable interannual variability, there are no significant temporal trends at the CONUS scale.

Figure 3.3: Ranking of public land acreage by state (a.), level I ecoregion forests (b.), and level 1 ecoregion rangelands (c.) vs the average productivity across public lands. Spearman's rank correlations (ρ) are significant at the state ($\rho = -0.53$; $p < 0.01$) and for rangeland ecoregion levels ($\rho = -0.79$; $p \leq 0.01$) but not forests ($\rho = 0.082$; $p = 0.72$).

Figure 3.4: Percent departure from expected production (PDE) for private lands across level IV ecoregions for forests (a.) and rangelands (b.). PDE highlights the degree to

which total production on private lands departs from the expected production given the respective area.

INTRODUCTION AND OVERVIEW

Background

Human land use practices can greatly alter land cover dynamics and ecosystem processes at a wide range of spatio-temporal scales (Houghton 1994, Ojima *et al*., 1994, Foley *et al*., 2005). The rate and extent of land use and land cover (LULC) is strongly linked to human population growth, economic growth, and technological development (Lambin *et al*., 2001). Over the last few centuries, particularly since the industrial revolution, broad scale human driven environmental change has occurred at unprecedented rates, with estimates as high as one-half of the earth's land surface directly altered by human activity (Vitousek *et al*., 1997). With increasing human population growth over the next century (Mustard *et al*., 2012), continued economic expansion and further technological development, global LULC change is not expected to diminish. Additionally, the impacts of human activities on the landscape often have broader, cumulative effects on ecosystem processes and services, with implications well beyond locally realized direct effects (Allred *et al*., 2015), as energy and nutrient fluxes, water availability, biodiversity, and species distributions may all be altered.

A considerable challenge for conservation is monitoring and evaluating human induced LULC and quantifying these changes in metrics useful for assessing the effects on ecological processes and ecosystem services (Pettorelli *et al*., 2014, Maron *et al.*, 2015). A primary challenge is overcoming divergent scales between the ecological processes and standard approaches to measuring them. Field based measurements are generally not feasible at scales most LULC occurs (Kerr & Ostrovsky 2003). Satellite remote sensing (SRS) datasets and models can overcome these limitations, providing spatio-temporally

continuous datasets across broad extents. However, these data are beset with inherent tradeoffs between spatial and temporal resolutions, spectral sensitivity to ecologically relevant factors, and the representativeness of models to biophysical processes (Kennedy *et al*., 2009). Until recently, analyses across broad spatial or temporal extents have generally limited to data with coarse spatial resolution, while analyses at higher spatial resolutions are conversely limited to finer spatial and temporal extents. Thus, crucial ecological processes occurring across broad spatio-temporal scales and at fine spatial resolutions are often missed (Turner *et al.,* 2003). Additionally, linking SRS data to meaningful metrics that relate to ecological processes and ecosystem services is not always straightforward. As a result, the effective use of these datasets in conservation has been limited.

Terrestrial gross and net primary production (GPP/NPP) are key biological variables that can be modelled using SRS data and process based models (Potter *et al*., 1993, Running *et al.,* 2000). These variables represent the entry point of carbon into ecosystems and quantify the amount of energy available across trophic levels. Thus, GPP and NPP are fundamental ecosystem processes foundational to biodiversity and all ecosystem services (Loreau *et al.,* 2001). GPP and NPP dynamics vary greatly both spatio-temporally and relative to human influence. As such, GPP and NPP are ideal variables for defining healthy ecosystems, assessing change and degradation at broad scales, and quantifying cumulative effects of land management and conservation strategies.

Despite the utility of GPP and NPP, the only existing publically available dataset is the MODIS based MOD17 product (Running & Zhao 2015). While the utility and applicability of this product cannot be overstated, it is fundamentally a global product at

coarse resolution (500 m), limiting its applicability in monitoring at ecologically relevant scales. Recent advancements in geospatial cloud computing technologies, such as Google Earth Engine (Gorelick *et al*., 2016), enable the access and utilization of vast archives of publically available high resolution SRS and other high resolution geospatial datasets. These technologies are facilitating exciting new areas of research and application, integrating SRS for enhanced conservation and management, at scales and resolutions not previously possible. These data are being used to monitor forest change at global scales (Hansen *et al*., 2013), provide detailed datasets of global water occurrence and change (Pekel *et al*., 2016), predict crop yields (Lobell *et al*., 2015), map disease risk (Sturrock *et al*., 2014) and better understand species distributions around the globe (Map Of Life, 2017). In this dissertation, I add to this inventory of high resolution, broad scale, and highly relevant products. Capitalizing on these technologies, I create the highest resolution datasets of GPP and NPP available for the conterminous United States (CONUS), based on the MOD17 algorithm.

Research Objectives

The main objective of this study is to create GPP and NPP datasets that better match the resolution of conservation and land management. To achieve this, I:

(i) Develop a methodology for creating high resolution, spatially continuous and temporally regular Landsat NDVI mosaics that integrate into the MOD17 algorithm as the underlying inputs (FPAR and LAI) of vegetation dynamics.

(ii) Develop and validate high resolution GPP and NPP datasets for CONUS, integrating the MOD17 algorithm into Google Earth Engine, replacing model inputs with higher resolution datasets and parameterizing the model with locally optimized parameters.

(iii) Demonstrate the applicability of the products for use within conservation and management.

Summary Overview

I divide this dissertation into three chapters. Each chapter is the subject of a peer-reviewed journal submission, and as a result, is a distinct entity, but contributes to the primary objectives.

Chapter 1: Landsat derived normalized difference vegetation index (NDVI) for the conterminous United States

Satellite derived vegetation indices (VIs) are broadly used in ecological research, ecosystem modeling, and land surface monitoring. The NDVI, perhaps the most utilized VI, has countless applications across ecology, forestry, agriculture, wildlife, biodiversity, and other disciplines. Calculating satellite derived NDVI is not always straight-forward, however, as satellite remote sensing datasets are inherently noisy due to cloud and atmospheric contamination, data processing failures, and instrument malfunction. Readily available NDVI products that account for these complexities are generally at coarse resolution; high resolution NDVI datasets are not conveniently accessible and developing them often presents numerous technical and methodological challenges. We address this deficiency by producing a Landsat derived, high resolution (30m), long-term (30+ years)

NDVI dataset for CONUS. We use Google Earth Engine, a planetary-scale cloud-based geospatial analysis platform, for processing the Landsat data and distributing the final dataset. We use a climatology driven approach to fill missing data and validate the dataset with established remote sensing products at multiple scales. We provide access to the composites through a simple web application, allowing users to customize key parameters appropriate for their application, question, and region of interest.

Chapter 2: Landsat 30 m and MODIS 250 m derived terrestrial primary production for the conterminous United States.

Terrestrial primary production is a fundamental ecological process and a crucial component in understanding the flow of energy through trophic levels. The global MODIS gross primary production (GPP) and net primary production (NPP) products (MOD17) are widely used for monitoring GPP and NPP at coarse resolutions across broad spatial extents. The coarse input datasets and global biome level parameters, however, are well-known limitations to the applicability of the MOD17 product at finer scales. We address these limitations and create two improved products for the CONUS that capture the spatiotemporal variability of terrestrial production. We use the MOD17 algorithm with medium resolution land cover classifications and improved meteorological data specific to CONUS to produce: a) Landsat derived 16-day GPP and annual NPP at 30 m resolution from 1986 to 2016 (GPP_{L30} and NPP_{L30}, respectively); and b) MODIS derived 8-day GPP and annual NPP at 250 m resolution from 2001 to 2016 (GPP_{M250} and NPP_{M250}, respectively). We optimized the biome specific input parameters based on eddy covariance flux tower-derived GPP data from the FLUXNET2015 database. We evaluated GPP_{L30} and GPP_{M250} products against the standard MODIS GPP

product utilizing a select subset of representative flux tower sites, and found improvement across all land cover classes except croplands. We further found consistent interannual variability and trends across NPP_{L30}, NPP_{M250}, and the standard MODIS NPP product. We highlight the application potential of the production products, demonstrating their improved capacity for monitoring terrestrial production at higher levels of spatial detail across broad spatiotemporal scales.

Chapter 3: Ownership dynamics of terrestrial production across the conterminous United States: implications for conservation

The foundational conservation paradigm in the United States centers around a network of public lands, accounting for almost 30% of the land area in the conterminous United States (CONUS). Although a third of the land area, public lands are unevenly distributed across the CONUS domain, resulting in a mosaic of public and private land in some areas, and completely private in others. We quantify the ownership patterns of terrestrial net primary production–a primary ecosystem function and supporting ecosystem service–within CONUS and the extent to which public land conserves net primary production. Our results show that total production on private land across CONUS more than doubles that of production on public and tribal lands combined. Likewise, average productivity across CONUS is greater on private lands than on public and tribal land, 13 and 32% greater on forests and 83 and 36% greater on rangelands. In western ecoregions, that are predominantly public lands, average productivity on private lands exceeds that of public land on almost all ecoregions. As terrestrial production is necessary for the production of all other ecosystem services, understanding the ownership–and ultimately management

and responsibility–of terrestrial production is a critical component of broader ecosystem sustainability.

References

Allred, B. W., Smith, W. K., Twidwell, D., Haggerty, J. H., Running, S. W., Naugle, D. W., & Fuhlendorf, S. D. (2015) Ecosystem services lost to oil and gas in North America. *Science*, **348**: 401–402.

Foley, J. A., Defries R., Asner, G.P., Barford, C., Bonan, G., Carpenter, S. R., Chapin, F. S., Coe, M. T., Daily, G. C., Gibbs, H. K., Helkowski, J. H., Holloway, T., Howard, E. A., Kucharik, C. J., Monfreda, C., Patz, J.A., Prentice, I. C., Ramankutty, N. & Snyder, P. K. (2005) Global consequences of land use. *Science*, **309**:570–574.

Gorelick, N., Hancher, M., Dixon, M., Ilyushchenko, S., Thau, D., & Moore, R. (2017) Google Earth Engine: Planetary-scale geospatial analysis for everyone. *Remote Sensing of Environment, **2016***.

Hansen, M. C., Potapov, P. V., Moore, R., Hancher, M., Turubanova, S. A.,Tyukavina, A., Thau, D., Stehman, S.V., Goetz, S.J., Loveland, T. R., Kommareddy, A., Egorov, A., Chini, L., Justice, C.O., & Townshend, J.R.G. (2013) High-resolution global maps of 21st-century forest cover change. *Science*, **342**:850–853.

Houghton, R.A. (1994) The Worldwide Extent of Land-Use Change. *Bioscience*, **44**:305–313.

Kennedy, R.E., Townsend, P. A., Gross, J. E., Cohen, W.B., Bolstad, P., Wang, Y. Q. & Adams, P. (2009) Remote sensing change detection tools for natural resource managers: Understanding concepts and tradeoffs in the design of landscape monitoring projects. *Remote Sensing of Environment,* **113**:1382–1396.

Kerr, J. T., & Ostrovsky, M. (2003). From space to species: ecological applications for remote sensing. *Trends in Ecology & Evolution,* **18**:299–305.

Lambin, E. F., Turner, B. L., Geist, H. J., Agbola, S. B., Angelsen, A., Bruce, J. W., Coomes, O. T., Dirzo, R., Fischer, G., Folke, C., George, P. S., Homewood, K., Imbernon, J., Leemans, R., Li, X., Moran, E. F., Mortimore, M., Ramakrishnan, P. S., Richards, J. F., Skånes, H., Steffen, W., Stone, G. D., Svedin, U., Veldkamp, T. A., Vogel, C., & Xu, J. (2001) The causes of land-use and land-cover change: moving beyond the myths. *Global Environmental Change: Human and Policy Dimensions*, **11**:261–269.

Lobell, D. B., Thau, D., Seifert, C., Engle, E., & Little, B. (2015) A scalable satellite-based crop yield mapper. *Remote Sensing of Environment,* **164**:324–333.

Loreau, M., Naeem, S., Inchausti, P., Bengtsson, J., Grime, J. P., Hector, A., Hooper, D. U., Huston, M. A., Raffaelli, D., Schmid, B., Tilman, D., & Wardle, D. A. (2001) Biodiversity and ecosystem functioning: current knowledge and future challenges. *Science*, **294**:804–808.

Map of Life. (2017) https://mol.org/

Maron, M., Gordon, A., & Mackey, B. G. (2015) Agree on biodiversity metrics to track from space. *Nature*, **523**:403–405.

Mustard, J. F., Defries, R. S., Fisher, T., & Moran, E. (2012) *Land Change Science*. Springer Netherlands.

Ojima, D. S., Galvin, K. A., & Turner B. L. (1994) The global impact of land-use change. *Bioscience,* **44**:300–304.

Pekel, J. F, Cottam, A., Gorelick, N., & Belward, A. S. (2016) High-resolution mapping of global surface water and its long-term changes. *Nature*, **540**:418–422.

Pettorelli, N., Safi, K., & Turner, W. (2014). Satellite remote sensing, biodiversity research and conservation of the future. P*hilosophical Tansactions of the Royal Society of London. Series B, Biological Sciences,* **369**:20130190.

Potter, C. S., Randerson, J. T., Field, C. B., Matson, P. A., Vitousek, P. M., Mooney, H. A., & Klooster, S. A. (1993) Terrestrial ecosystem production: a process model based on global satellite and surface data. *Global Biogeochemical Cycles,* **7**.

Running, S. W., Thornton, P. E., Nemani, R., & Glassy, J. M. (2000) *Methods in Ecosystem Science*. Springer, New York.

Running, S. W., & Zhao, M. (2015) MOD17 Users Guide 2015. *Numerical Terradynamic Simulation Group*.

Sturrock, H. J. W, Cohen, J.M., Keil, P., Tatem, A. J., Le Menach, A., Ntshalintshali, N. E., Hsiang, M. S., & Gosling, R. D. (2014) Fine-scale malaria risk mapping from routine aggregated case data. *Malaria Journal,* **13**:421.

Turner, W., Spector, S., Gardiner, N., Fladeland, M., Sterling, E., & Steininger, M. (2003) Remote sensing for biodiversity science and conservation. *Trends in Ecology & Evolution*, **18**:306–314.

Vitousek, P. M., Mooney, H. A., Lubchenco, J., & Melillo, J. M. (1997) Human domination of earth's ecosystems. *Science*, **277**:494–499.

CHAPTER 1: LANDSAT DERIVED NORMALIZED DIFFERENCE VEGETATION INDEX (NDVI) FOR THE CONTERMINOUS UNITED STATES

1.1 Introduction

The Normalized Difference Vegetation Index (NDVI) is arguably the most widely implemented remote sensing spectral index for monitoring Earth's land surface. Since the earliest report of use in 1973 (Rouse *et al.,* 1974, Tucker *et al.,* 1973), the term NDVI is found in nearly 121,000 scientific articles, conference papers, and books (Google Scholar). The index capitalizes on the optical properties of the cellular structure of leaves; the photosynthetic pigments (chlorophyll, associated light-harvesting pigments, and accessory pigments) efficiently absorb radiation in the visible range of the spectrum (to power photosynthesis) and reflect radiation in the near-infrared (NIR) range. The simple formula of NDVI and its direct relationship to vegetation photosynthetic capacity is a proxy for a wide range of essential vegetation characteristics and functions (e.g., fraction of photosynthetic radiation absorbed by the canopy, leaf area, canopy "greenness", gross primary productivity) with countless applications in agriculture, forestry, ecology, biodiversity, habitat modeling, species migrations, land surface phenology, earth system processes (nutrient cycling, net primary productivity, evapotranspiration), and even economic, social, and medical sciences.

Satellite remote sensing (SRS) allows for the calculation of NDVI globally at a range of temporal intervals and spatial resolutions dependent on sensor characteristics and the satellite orbit, with a common inverse relationship between temporal and spatial resolutions. The Landsat Mission, with its first sensor launched in 1972, is the only uninterrupted long-term (>30 years) high-resolution remote sensing dataset that can provide a continuous historic NDVI record globally. The Landsat record at 30-meter resolution is ideally suited for local or regional scale time-series applications, particularly

with the recent release of higher-level surface reflectance products from Landsat sensors 5 ETM, 7 ETM+, and 8 OLI from 1984 to present. Utilizing these products across scenes and through time, however, is not without complications (Wijedasa *et al.,* 2012), particularly for users without GIS and Remote Sensing training and resources. To create consistent mosaics or long-term time series, users must account for data record gaps, radiometric differences across sensors (She *et al.,* 2015), scene overlaps, malfunctions (e.g., the Landsat 7 scan line corrector malfunction), and inherent noise (due to clouds, atmospheric contamination, missing auxiliary data, etc.). As the region of interest and temporal extent increases, data volume and compute processing needs present significant barriers to many users without access to high performance computing facilities or the necessary skills to manipulate such data. These limitations often prevent the implementation of such a dataset in ecological studies, conservation monitoring efforts, or teaching exercises despite the clear value of its application.

The rise of high performance computing clusters, public access to supercomputing facilities and cloud computing and storage removes many of the computational barriers associated with Landsat data. The ability to create user friendly applications that interacts with these computing services eliminates additional barriers associated with data manipulation and enables users with minimal technical coding skills to access and process data. We capitalize on the abilities of high performance computing resources and web-based software to provide a Landsat derived conterminous U.S. (CONUS), 30-meter resolution, NDVI product (Figure 1.1). We use Landsat 5 ETM, 7 ETM+, and 8 OLI sensors, with a user specified climatology (historic NDVI value limited by a user-defined time-period) for temporal smoothing, and Google Earth Engine (a cloud-based geospatial

platform for planetary-scale data analysis) for rapid data processing and visualization (Gorelick *et al.,* 2016), to produce 16 day NDVI composites from 1984-2016. We validate the NDVI product by comparing against other established remote sensing products across multiple spatial scales. The resulting NDVI record enables greater use of Landsat data in answering crucial ecological questions across broad spatio-temporal scales at a higher level of spatial detail than possible with other currently available NDVI products. While Landsat composite products exist (e.g., the Web Enabled Landsat Data product (Roy *et al.,* 2010) and the ability to create simple mean/median/max composites) our product improves upon these with the novel gap-filling and smoothing approaches (Figure 1.2). Additionally, we make the composites available through a dynamic web application, allowing users to customize key parameters to produce NDVI composites more suited to specific regions or ecological questions.

1.2 Materials and Methods

1.2.1 DATA

We use the surface reflectance (SR) products from Landsat 5 ETM, 7 ETM+, and 8 OLI sensors to create NDVI composites. The Landsat satellites have near-polar orbits with a repeat overpass every 16 days; throughout the Landsat missions; however, two satellites have often operated simultaneously (Figure 1.3) in asynchrony, creating an eight-day return overpass for a given area. Furthermore, adjacent orbits of a single sensor spatially overlap from 7% at the equator to 68.7% at 70° latitude (Pekel *et al.,* 2016). During a single 16-day period there may be as many as four independent views for a given point.

Our compositing method (Figure 1.4) capitalizes on the operation of multiple sensors and views to maximize the potential of retrieving an NDVI observation every 16 days.

The Landsat SR products (Masek *et al.,* 2006, Vermote *et al.,* 2016) correct for atmospheric and illumination/viewing geometry effects, and are the highest level of image processing available for Landsat data. Although some images are not processed due to missing auxiliary data, the use of SR is generally more appropriate for measuring and monitoring vegetation at the land surface (Song *et al.,* 2001, Feng *et al.,* 2012) Landsat Surface reflectance products also contain useful pixel data quality flag information indicating clear, water, snow, cloud or shadow conditions, as determined by the CFMask algorithm (Foga *et al.,* 2017). We employ this information to select the best available data within each composite period.

1.2.2 COMPOSITING

To produce a pixel-wise 16-day composite (date of composite plus subsequent 15 days), all available Landsat surface reflectance images (from 5 ETM, 7 ETM+, and 8 OLI) are processed. Landsat scenes are resampled bilinearly to a Geographic Coordinate System WGS84 grid of approximately 30m (1/5000 degrees) resolution. NDVI is calculated as:

$$NDVI = (\rho NIR - \rho RED) \Big/ (\rho NIR + \rho RED) \quad (1)$$

where ρNIR is surface reflectance in the near infrared band (band 4 - Landsat 5, 7; band 5 -Landsat 8) and ρRED is surface reflectance in the red band (band 3 - Landsat 5, 7; band 4 - Landsat 8). To account for sensor differences, we adjusted landsat NDVI values from

Landsat 5 ETM and 7 ETM+ to match Landsat 8 OLI using a simple linear transformation: (Roy *et al.,* 2016).

$$NDVI_{L8} = 0.0235 + 0.9723 * NDVI_{L5,7} \quad (2)$$

Additionally, Landsat 5 scenes often contain abnormalities along scene edges, resulting in both missing data and erroneously high NDVI values. These pixels are removed by buffering 450 m inwards from the image mask (Figure 1.S1). The buffer size was determined from visual inspection of a subset of Landsat 5 scenes, ensuring removal of all the erroneous pixels without losing substantial amounts of valid data. To ensure the best available data for each composite, pixels are selected and used based on their quality flag. First, all pixels flagged as clear during a 16-day period are selected and the mean NDVI calculated. If no 'clear' pixels are available, the mean NDVI value of all 'water' and 'snow' pixels is used. If there are still no available pixels, (i.e., all pixels within the 16-day period are flagged as cloud or shadow, or no surface reflectance images are available) the pixel is filled with a climatology. The climatology is calculated as the median NDVI of 'clear', 'water' and 'snow' pixels over the same 16-day period from previous years, with the user specifying the number of years. The median climatology is used to minimize the effects abnormally wet or dry years within the climatology record. In rare instances when no climatology is available (i.e., all pixels within the set climatology length are flagged as cloud or shadow), the composite is filled with a no-data value.

1.2.3 SMOOTHING

As NDVI is a proxy for vegetation greenness, it is expected to follow a relatively smooth and continuous temporal profile. Outside of disturbance or land cover change events, a sudden drop in NDVI is likely due to atmospheric contamination or a quality issue not identified in the Landsat surface reflectance product (Reed *et al.,* 2994, Bradley *et al.,* 2007). To account for these anomalous declines, we employ a smoothing method, similar to iterative Interpolation for Data Reconstruction (IDR) (Julien & Sobrino 2010). If a composite NDVI value is less than the mean of the previous and following time step composites by a threshold of 0.1, it is replaced by that mean value. While Julien and Sobrino suggest iteratively smoothing until convergence is reached, we only smooth once as multiple runs significantly increases computational time at large scales. Invocation of the smoothing algorithm by the user is optional.

1.2.4 QUALITY

A quality band is provided to specify the attributes of the raw data used to calculate each pixel's composite value. The quality band indicates if a composite value was calculated from clear pixels; water or snow pixels; or if the climatology was used. The quality band also indicates if a composite value is the result of smoothing. Table 1.1 shows the range of quality band values and descriptions.

1.2.5 PRODUCT CREATION AND DISTRIBUTION

Landsat derived NDVI is available through a simplified web-interface (Figure 1.5, http://ndvi.ntsg.umt.edu/) that utilizes Google Earth Engine. Users define a region of interest, select a time period, the length of the climatology used for gap filling (2, 5, 10, 15, 20, 25 or 30 years), inclusion of Landsat 7 ETM+ SLC-off data, and whether to apply the smoothing algorithm. The customized NDVI composite is then produced (as a GeoTIFF) as requested based on the user defined parameters.

1.2.6 NDVI COMPARISONS ACROSS SPATIAL SCALES

We compare the Landsat derived NDVI record to independently derived finer and coarser resolution data, including: the green chromatic coordinate from in situ phenology camera (phenocam) observations and the Moderate Resolution Imaging Spectroradiometer 16-day 250m NDVI product (MOD13Q1). We use Landsat derived NDVI composites with a five-year climatology for gap filling and employ the IDR smoothing algorithm for the validation comparisons.

The PhenoCam Network provides automated, sub-daily, near-surface remote sensing of canopy phenology through digital repeat photography (Richardson *et al.,* 2009). The images are continuous in time and robust to variation in illumination condition, with minimal influence from clouds or atmospheric effects, particularly when calculating vegetation indices (Sonnentag *et al.,* 2012). Numerous studies (Richardson *et al.,* 2007, Ahrends *et al.,* 2009, Zhao *et al.,* 2012) have demonstrated that the green chromatic coordinate (GCC; Tomey *et al.,* 2015); can be used to identify phenology phases and

monitor canopy development, with strong correlations to NDVI time series. The GCC is calculated as:

$$GCC = {DN_g}/{(DN_r + DN_g + DN_b)} \quad (3)$$

Where DN is the digital number recorded by the camera and r, g, and b denote red, green, and blue channels respectively. PhenoCam Network sites within CONUS that had at least four years of continuous imagery were selected for analysis; resulting in 43 sites that include agriculture/crops, shrublands, grasslands, deciduous broadleaf forests, and evergreen needleleaf forests (Figure 1.S2). We use the daily GCC90 data provided by the PhenoCam Network, which represents the daily 90th percentile of the GCC during daylight hours. A 16-day mean is calculated from the daily GCC90, using the same 16-day period as the Landsat NDVI product. The corresponding Landsat NDVI time series is extracted over each PhenoCam site, followed by calculation of Pearson correlation coefficients.

Within each image field of view (FOV), a predefined region of interest (ROI) is used to calculate the GCC, isolating the plant functional type (PFT) of interest. Depending on the FOV, more than one ROI can be defined, providing two independent time series of different PFTs. Four of the 43 sites contained two ROIs and we compare both ROIs at these sites to the single broader scale (30m) Landsat NDVI time series.

The comparison of two independent vegetation indices derived from sensors with different bandwidths, fields of view, and viewing geometries is not without issue (Petach *et al.,* 2014) The GCC is more sensitive to leaf pigmentation than NDVI (Keenan *et al.,* 2014) and the Landsat pixel may not capture the camera FOV or may be smaller than the

FOV. However, the PhenoCam data provides the only multi-year, high spatial and temporal resolution standardized product comparable to the 30m land surface phenology signal. The correlations provide an assessment of the Landsat NDVI composites seasonal response to vegetation conditions either within or in close proximity to the camera FOV.

The MODIS VI products (MOD13) are designed to provide consistent spatiotemporal observations of vegetation conditions, have been continually produced since 2001 (Solano *et al.,* 2010), and employed in at least 1700 peer-reviewed research articles (Google Scholar). The MOD13Q1 product has a 16-day NDVI composite with an approximate spatial resolution of 250m. Like the Landsat NDVI product, the MOD13Q1 16-day composite period includes the composite date and 15 ensuing days. MOD13Q1 composites are created using a constrained-view angle, maximum value composite technique, and the MODIS surface reflectance product (Didan *et al.,* 2015).

We compare the Landsat derived NDVI to the MOD13Q1 NDVI from 2000-2016. Time series of both products are extracted for a set of points across the CONUS domain (Figure 1.S2) using a stratified random sample across land cover classes. Points are only selected within areas of homogenous land cover at the MODIS resolution, determined using the National Land Cover Dataset (NLCD) for 2001, 2006 and 2011 (Homer *et al.,* 2007, Fry *et al.,* 2009, Homer *et al.,* 2015). Within these homogenous regions, up to 50 random points are created, using Google Earth Engine's random point function, for 12 major land cover classes across the domain (evergreen forest, deciduous forest, mixed forest, shrubland, grassland, pasture/hay, herbaceous wetland, wooded wetland, barren, developed-open space and developed-low intensity). For certain land cover classes, less than 50 random points in homogeneous pixels are available, resulting in a total sample

size of 356 points across the domain. To match resolutions, the Landsat NDVI was degraded to the MODIS 250m resolution where the mean Landsat NDVI value was calculated within the extent of each MODIS pixel. The time series for both products were extracted, disregarding any null values, resulting in 131,973 paired observations. The Pearson correlation coefficients (r-value), mean bias, mean absolute bias (MAB), and root mean square error (RMSE) are calculated for the entire series and each location separately.

1.3. Results

1.3.1 PHENOLOGY CAMERAS RESULTS

The phenocam correlation analysis (Table 1.S1) resulted in 36 of the 47 ROIs exhibiting r-values greater than 0.70, and just three ROIs with r-values less than 0.30 (all ROIs: mean r-value = 0.72; range: -0.35 - 0.92; $p < 0.01$ for all cases). The high and significant correlations demonstrate that the 16-day Landsat composites do well in capturing the seasonal greenness patterns exhibited by the phenocam GCC90. The sites with the three lowest correlations provide good examples where the resulting NDVI values and their comparison to other data products requires careful interpretation. One site (drippingsprings; r = 0.22) presents a mismatch between the vegetation in the extent of the Landsat pixel and the ROI of the phenocam image. The phenocam ROI delineates a single deciduous broadleaf tree canopy in a narrow ravine, while the extent of the Landsat pixel includes other riparian zone species and shrubs above the ravine. Another low correlation site (oregonMP; r = -0.24) is from an evergreen needleleaf forest in Oregon. Examination of the quality band indicates this site is often obscured by clouds

and snow in the winter months, resulting in a spurious NDVI time series with poorly defined seasonality, while the GCC90 time series provides a well-defined seasonal signal. The site with the lowest correlation (sedgwick SH; r = -0.35) contained two ROIs and is discussed below.

Three of the four sites with two ROIs displayed strong correlations both between ROI's ($0.81 < r < 0.94$) and versus the Landsat NDVI ($0.72 < r < 0.88$). Therefore, even though the two ROIs within a site delineated separate PFTs, the PFTs displayed a common seasonality. The fourth site with one grass ROI and one shrub ROI, located on the Sedgwick Reserve in southern California, displayed contrasting results: Shrub vs. Grass ROI, r-value = -0.20; Shrub ROI vs. Landsat NDVI, r-value = -0.35; Grass ROI vs. Landsat NDVI, r-value = 0.75. Examination of the time series revealed that the Shrub ROI was out of phase with the Grass ROI, with a seasonal lag of approximately three months, resulting in negative correlations when compared to the grassland dominated NDVI signal.

The low correlation sites highlight two important considerations that must be accounted for when comparing satellite and ground-level observations. First, vegetation indices from satellite data represent integrated measures of the vegetation at the pixel scale often confounding comparisons to canopy scale indices, such as those derived from phenology cameras particularly over heterogeneous landscapes (Hufkens *et al.,* 2012, Klosterman et al, 2014). Second, phenology camera FOVs will vary from site to site, and in some cases an ROI may be beyond the extent of the satellite pixel that contains the camera, particularly when implementing high resolution (30m) data.

1.3.2 MOD13Q1 RESULTS

We found high correlations between the Landsat NDVI product and coarser MOD13Q1 observations (Table 1.2, Figure 1.6), with an overall r-value of 0.94. When disaggregated by the Landsat product quality flag these data show a higher correlation for clear pixels (r-value = 0.97), slightly lower correlation for climatology filled pixels (r-value = 0.88) and still lower correlation for snow/water pixels (r-value = 0.70).

When disaggregated to individual points, 258 of the 356 points (72%) exhibit r-values greater than 0.70, while 24 points had correlations lower than 0.30 (all points: mean r-value = 0.74; range: 0.01 - 0.97). The generally favorable results demonstrate that the 16-day Landsat NDVI composites track the greenness trends captured by the MOD13Q1 product. The relationship breaks down at some sites, especially within certain land cover classes (Figure 1.6).

The poorest performing land cover classes, with r-values less than 0.70, represent barren, evergreen needleleaf forest, and herbaceous wetland (mean r-values: 0.41, 0.57, and 0.64 respectively) land cover conditions. NDVI over barren land may be highly variable due to the high saturation of background soils affecting the sensors differently. The low mean correlations in evergreen forest is largely due to a few influential outliers. Many of these sites are located in the northwest. Similar to the oregonMP PhenoCam site, the time series are often contaminated with clouds and snow, and exhibit little NDVI seasonality. Temporal profiles of the Landsat NDVI and MOD13Q1 product (Figure 1.7), for a selection of points representing the major land cover classes across CONUS (Figure 1.S2), demonstrate the strong correlation between the two products.

The profiles are particularly analogous during the growing season. It is mainly during the winter months where the profiles tend to diverge, as the Landsat composites are more likely contaminated with cloud and/or snow cover, with lower signal-to-noise. Additionally, in heterogenous landscapes, the 30m Landsat NDVI product better reflects the spatial variability of the underlying land cover (Figures 1.1 and 1.8).

1.4 Discussion

The first-ever 16-day continuous and customizable Landsat derived NDVI composites produced here (30m resolution for CONUS; 1984-2016) overcome many of the previous barriers of working with Landsat imagery (e.g., obtaining current or historical images; managing overlapping scenes; image storage and processing; etc.), permitting ecologists to focus time and effort on specific questions rather than data/imagery manipulation. The composites are well correlated with other observational benchmarks, including in situ phenocam observations of local vegetation conditions and coarser satellite observations from MODIS (MOD13Q1), demonstrating product capabilities for tracking greenness trends from local to regional extents. Fine spatial resolution products such as these, with a longer historical record (Figure 1.3), open the door to numerous analytical possibilities and applications, ranging from change detection to conservation monitoring to ecosystem assessment (Jensen *et al.,* 2995, Nouvellon *et al.,* 2001, Hansen & Loveland 2012) The ability to customize the NDVI composite, per user specification, grants the use of a priori knowledge of the region to obtain the most suitable composite for the question at hand, producing an application ready product without the need for post-processing.

As with all remotely sensed products, the scope of Landsat derived NDVI has limitations, and is best suited for local or regional applications, where incomplete data are minimized due to a smaller spatial extent. Due to the infrequent return time of Landsat observations, data may be limited during the 16-day compositing period; cloudy pixels or the lack of surface reflectance images will reduce the overall data available for the composite. Additionally, due to the orbital paths of the Worldwide Reference System 2, a composite may be created from multiple scenes obtained from different dates within the 16-day period (e.g., different scenes that intersect an area of interest but are acquired at the beginning and end of the 16-day period). If data are incomplete (e.g., cloudy pixels, scan line corrector errors of Landsat 7 ETM+, etc.) within these scenes, it is possible that two adjacent pixels can represent two different acquisition dates; if no data for the period are available then a climatology is used for gap filling, further distancing the dates used in the composite. Frequency of gap filling that occurs varies both geographically and seasonally, and is more likely when only a single Landsat sensor is operational. Furthermore, gap filling with climatology may produce anomalies, particularly during unusually wet or dry years, yielding systematically low or high values, respectively. These caveats may result in visual artifacts in areas with incomplete data or along scene edges.

The real power of emerging big data, cloud and web-based applications, and technologies (e.g., Google Earth Engine, GeoTrellis, GeoMesa, Apache Spark, etc.) is our new-found ability to create customizable geospatial products. Publicly available applications may be built upon these technologies, ultimately allowing users greater flexibility to provide input data, set spatial or temporal restrictions, modify parameters of algorithms, or

perform on the fly testing and validation before final analysis. Such capabilities change the paradigm of static geospatial products to dynamic geospatial products, where the output is dependent upon the user's knowledge of both the system and the question. Although this requires products to be generated as needed, it provides the ability to create a much more appropriate product for any given system and question. The Landsat NDVI product and its associated web application (http://ndvi.ntsg.umt.edu/) provide a glimpse into this reality of dynamic geospatial products.

1.5 Conclusions

The present work introduces a unique approach to creating and disseminating high resolution spatially and temporally continuous Landsat derived NDVI. Our motivation is to remove the barriers of these datasets to further conservation and ecological research. Sixteen-day composites are created by selecting the best available pixels during each 16-day composite period from all available Landsat sensors. Missing values, due to unprocessed scenes, atmospheric contamination, or sensor malfunction are gap filled with a user-defined climatology. The resulting NDVI time series is then smoothed to approximate natural vegetative phenology. We validate the NDVI dataset using established remote sensing products at multiple scales, demonstrating the effectiveness of our approach. We provide open access to the dataset through a simple web application (http://ndvi.ntsg.umt.edu/) enabling ecologists, land managers, conservationists, and others–who may not have the compute processing capacity or technical skills–to process massive amounts of remote sensing data. This process is simplified with Google Earth Engine, an advanced planetary-scale cloud-based geospatial processing platform, which

processes and distributes the product. Each 16-day composite for CONUS requires processing at least 2700 individual Landsat scenes (more if the climatology is used for gap filling). The web application permits on-the-fly processing with customizable parameters, eliminating the need to store large amounts of data. Although we limit this study to CONUS, the framework can be expanded beyond CONUS where Landsat surface reflectance data are available and to include other useful vegetation indices (e.g. EVI, SAVI), and can be updated to accommodate updates or reorganization of the Landsat archive (e.g., Collection 1) or be modified to utilize other satellite remote sensing datasets.

1.6 Acknowledgments

We thank the Google Earth Engine developers for their support and technical advice. This work was funded through a Google Earth Engine research award and by the NRCS Wildlife Conservation Effects Assessment Project and Sage Grouse Initiative. The development of PhenoCam has been supported by the Northeastern States Research Cooperative, NSF's Macrosystems Biology program (award EF-1065029), DOE's Regional and Global Climate Modeling program (award DE-SC0016011), and the US National Park Service Inventory and Monitoring Program and the USA National Phenology Network (grant number G10AP00129 from the United States Geological Survey). We thank Koen Hufkens and Tom Milliman for their contributions to producing the PhenoCam data. We thank the PhenoCam site collaborators and funding sources (listed in the Supplementary Materials) for their support of the PhenoCam project.

1.7 References

Ahrends, H.E., Etzold, S., Kutsch, W. L., Stoeckli, R., Bruegger, R. Jeanneret, F., Wanner, H., Buchmann, N., & Eugster, W. (2009) Tree phenology and carbon dioxide fluxes: use of digital photography for process-based interpretation at the ecosystem scale. *Climate Research*, **39**, 261–274.

Bradley, B. A., Jacob, R. W., Hermance, J. F., & Mustard, J. F. (2007) A curve fitting procedure to derive inter-annual phenologies from time series of noisy satellite NDVI data. *Remote Sensing of Environment*, **106**, 137–145.

Didan, K., Munoz, A. B., Solano, R., & Huete, A. (2015) MODIS vegetation index user's guide (MOD13 Series), University of Arizona.

Feng, M., Huang, C., Channan, S., Vermote, E. F., Masek, J. G., & Townshend, J. R. (2012) Quality assessment of Landsat surface reflectance products using MODIS data. *Computers and Geoscienc*, **38**, 9–22.

Foga, S., Scaramuzza, P. L., Guo, S., Zhu, Z., Dilley, R. D., Jr, Beckmann, T., Schmidt, G. L., Dwyer, J. L., Joseph Hughes, M., & Laue, B. (2017) Cloud detection algorithm comparison and validation for operational Landsat data products. *Remote Sensing of Environment*, **194**, 379–390.

Fry, J. A., Xian, G., Jin, S., Dewitz, J. A., Homer, C. G., Limin, Y., Barnes, C. A., Herold, N. D., & Wickham, J. D. (2011) Completion of the 2006 National Land Cover Database for the conterminous United States. *Photogrammetric Engineering & Remote Sensing*, **77**, 858–864.

Gorelick, N., Hancher, M., Dixon, M., Ilyushchenko, S., Thau, D., & Moore, R. (2017) Google Earth Engine: Planetary-scale geospatial analysis for everyone. *Remote Sensing of Environment*, **2016**.

Hansen, M. C., & Loveland, T. R. (2012) A review of large area monitoring of land cover change using Landsat data. *Remote Sensing of Environment*, **122**, 66–74.

Homer, C. G., Dewitz, J. A., Yang, L., Jin, S., Danielson, P., Xian, G., Coulston, J., Herold, N. D., Wickham, J. D., Megown, K. (2015) Completion of the 2011 National Land Cover Database for the conterminous United States-Representing a decade of land cover change information. *Photogrammetric Engineering & Remote Sensing*, 81, 345–354.

Homer, C., Dewitz, J., Fry, J., Coan, M., Hossain, N., Larson, C., Herold, N., McKerrow, A., VanDriel, J. N., & Wickham, J., (2007) Others Completion of the 2001 national land cover database for the counterminous United States. *Photogrammetric Engineering & Remote Sensing,* **73**, 337.

Hufkens, K., Friedl, M., Sonnentag, O., Braswell, B. H., Milliman, T., & Richardson, A. D. (2012) Linking near-surface and satellite remote sensing measurements of deciduous broadleaf forest phenology. Remote Sensing of Environmet. **117**, 307–321.

Jensen, J. R., Rutchey, K., Koch, M. S., & Narumalani, S. (1995) Inland wetland change detection in the Everglades Water Conservation Area 2A using a time series of normalized remotely sensed data. *Photogrammetric Engineering & Remote Sensing*, **61**, 199–209.

Julien, Y., & Sobrino, J. A. (2010) Comparison of cloud-reconstruction methods for time series of composite NDVI data. *Remote Sensing of Environment*, **114**, 618–625.

Keenan, T. F., Darby, B., Felts, E, Sonnetag, O, Friedl, M. A., Hufkens, K., O'Keefe, J., Klosterman, S., Munger, J. W., Toomey, M., & Richardson, A. D. (2014) Tracking forest phenology and seasonal physiology using digital repeat photography: a critical assessment. *Ecological Applications*, **24**, 1478–1489.

Klosterman, S. T., Hufkens, K., Gray, J. M., Melaas, E., Sonnentag, O., Lavine, I., Mitchell, L., Norman, R., Friedl, M. A., & Richardson, A. D. (2014) Evaluating remote sensing of deciduous forest phenology at multiple spatial scales using PhenoCam imagery. *Biogeosciences*, **11**, 4305–4320.

Masek, J. G., Vermote, E. F., Saleous, N. E., Wolfe, R., Hall, F. G., Huemmrich, K. F., Gao, F., Kutler, J., & Lim, T. K. A (2006) Landsat surface reflectance dataset for North America, 1990-2000. *IEEE Geoscience and Remote Sensing Letters*, **3**, 68–72.

Nouvellon, Y., Moran, M. S., Seen, D. L., Bryant, R., Rambal, S., Ni, W., Bégué, A., Chehbouni, A., Emmerich, W. E., Heilman, P., & Qi, J. (2001) Coupling a grassland ecosystem model with Landsat imagery for a 10-year simulation of carbon and water budgets. *Remote Sensing of Environment*. **78**, 131–149.

Pekel, J. F., Cottam, A., Gorelick, N., & Belward, A. S. (2016) High-resolution mapping of global surface water and its long-term changes. *Nature*, **540**, 418–422.

Petach, A. R., Toomey, M., Aubrecht, D. M., & Richardson, A. D. (2014) Monitoring vegetation phenology using an infrared-enabled security camera. *Agriculture and Forest Meteorology*, **195**, 143–151.

Reed, B. C., Brown, J. F., VanderZee, D., Loveland, T. R., Merchant, J. W., & Ohlen, D. O. (1994) Measuring phenological variability from satellite imagery. *Journal of Vegetation Science,* **5**, 703–714.

Richardson, A. D., Braswell, B. H., Hollinger, D. Y., Jenkins, J. P., & Ollinger, S. V. (2009) Near-surface remote sensing of spatial and temporal variation in canopy phenology. *Ecological Applications*, **19**, 1417–1428.

Richardson, A. D., Jenkins, J. P., Braswell, B. H., Hollinger, D. Y., Ollinger, S. V., & Smith, M. L. (2007) Use of digital webcam images to track spring green-up in a deciduous broadleaf forest. *Oecologia*, **152**, 323–334.

Rouse, J. W., Jr, Haas, R. H., Schell, J. A., & Deering, D. W. (1974) Monitoring vegetation systems in the Great Plains with ERTS.

Roy, D. P., Ju, J., Kline, K., Scaramuzza, P. L., Kovalskyy, V., Hansen, M. C., Loveland, T. R., Vermote, E. F., & Zhang, C. (2010) Web-enabled Landsat Data (WELD): Landsat ETM+ Composited Mosaics of the Conterminous United States, *Remote Sensing of Environment,* **114**, 35-49.

Roy, D. P., Kovalskyy, V., Zhang, H. K., Vermote, E. F., Yan, L., Kumar, S. S., & Egorov, A. (2016) Characterization of Landsat-7 to Landsat-8 reflective wavelength and normalized difference vegetation index continuity. *Remote Sensing of Environment,* **185**, 57–70.

She, X., Zhang, L., Cen, Y., Wu, T., Huang, C., & Baig, M. H. A. (2015) Comparison of the continuity of vegetation indices derived from Landsat 8 OLI and Landsat 7 ETM+ data among different vegetation types. *Remote Sensing*, **7**, 13485–13506.

Solano, R., Didan, K., Jacobson, A., & Huete, A. (2010) MODIS vegetation index user's guide (MOD13 series). Vegetation Index and Phenology Lab, The University of Arizona, 1–38.

Song, C., Woodcock, C. E., Seto, K. C., Lenney, M. P., & Macomber, S. A. (2001) Classification and change detection using Landsat TM data: When and how to correct atmospheric effects? Remote Sensing of Environment, **75**, 230–244.

Sonnentag, O., Hufkens, K., Teshera-Sterne, C., Young, A. M., Friedl, M., Braswell, B. H., Milliman, T., O'Keefe, J., & Richardson, A. D. (2012) Digital repeat photography for phenological research in forest ecosystems. *Agriculture and Forest Meteorology,* **152**, 159–177.

Toomey, M., Friedl, M. A., Frolking, S., Hufkens, K., Klosterman, S., Sonnentag, O., Baldocchi, D. D., Bernacchi, C. J., Biraud, S. C., Bohrer, G., Brzostek, E., Burns, S. P., Coursolle, C., Hollinger, D. Y., Margolis, H. A., Mccaughey, H., Monson, R. K., Munger, J. W., Pallardy, S., Phillips, R. P., Torn, M. S., Wharton, S., Zeri, M., & Richardson, A. D. (2015) Greenness indices from digital cameras predict the timing and seasonal dynamics of canopy-scale photosynthesis. *Ecological Applications,* **25**, 99–115.

Tucker, C. J., Miller, L. D., & Pearson, R. L. (1973) Measurement of the combined effect of green biomass, chlorophyll, and leaf water on canopy spectroreflectance of the shortgrass prairie. *Remote Sensing of Earth Resources,* **2**.

Vermote, E., Justice, C., Claverie, M., & Franch, B. (2016) Preliminary analysis of the performance of the Landsat 8/OLI land surface reflectance product. *Remote Sensing of Environment*, **185**, 46–56.

Wijedasa, L. S., Sloan, S., Michelakis, D. G., & Clements, G. R. (2012) Overcoming limitations with Landsat imagery for mapping of peat swamp forests in Sundaland. *Remote Sensing*, **4**, 2595–2618.

Zhao, J., Zhang, Y., Tan, Z., Song, Q., Liang, N., Yu, L., & Zhao, J. (2012) Using digital cameras for comparative phenological monitoring in an evergreen broad-leaved forest and a seasonal rain forest. *Ecological Informatics*, **10**, 65–72.

1.8 Tables

Table 1.1 NDVI quality band values and descriptions.

Pixel Value	Description
10	Clear not smoothed
11	Clear and smoothed
20	Snow or water not smoothed
21	Snow or water smoothed
30	Climatology not smoothed
31	Climatology smoothed

Table 1.2 Mean bias, mean absolute bias, root mean square error, and r-values for all the MOD13Q1 and Landsat NDVI sample points combined. Each statistic is calculated for all pixels and each quality flag separately.

Statistic	All Pixels	Clear Pixels	Snow/Water Pixels	Climatology Pixels
Mean Bias	-0.03	-0.03	-0.01	-0.02
MAB	0.06	0.05	0.10	0.09
RMSE	0.10	0.08	0.15	0.14
Pearson's r	0.94	0.97	0.71	0.88

1.9 Figures

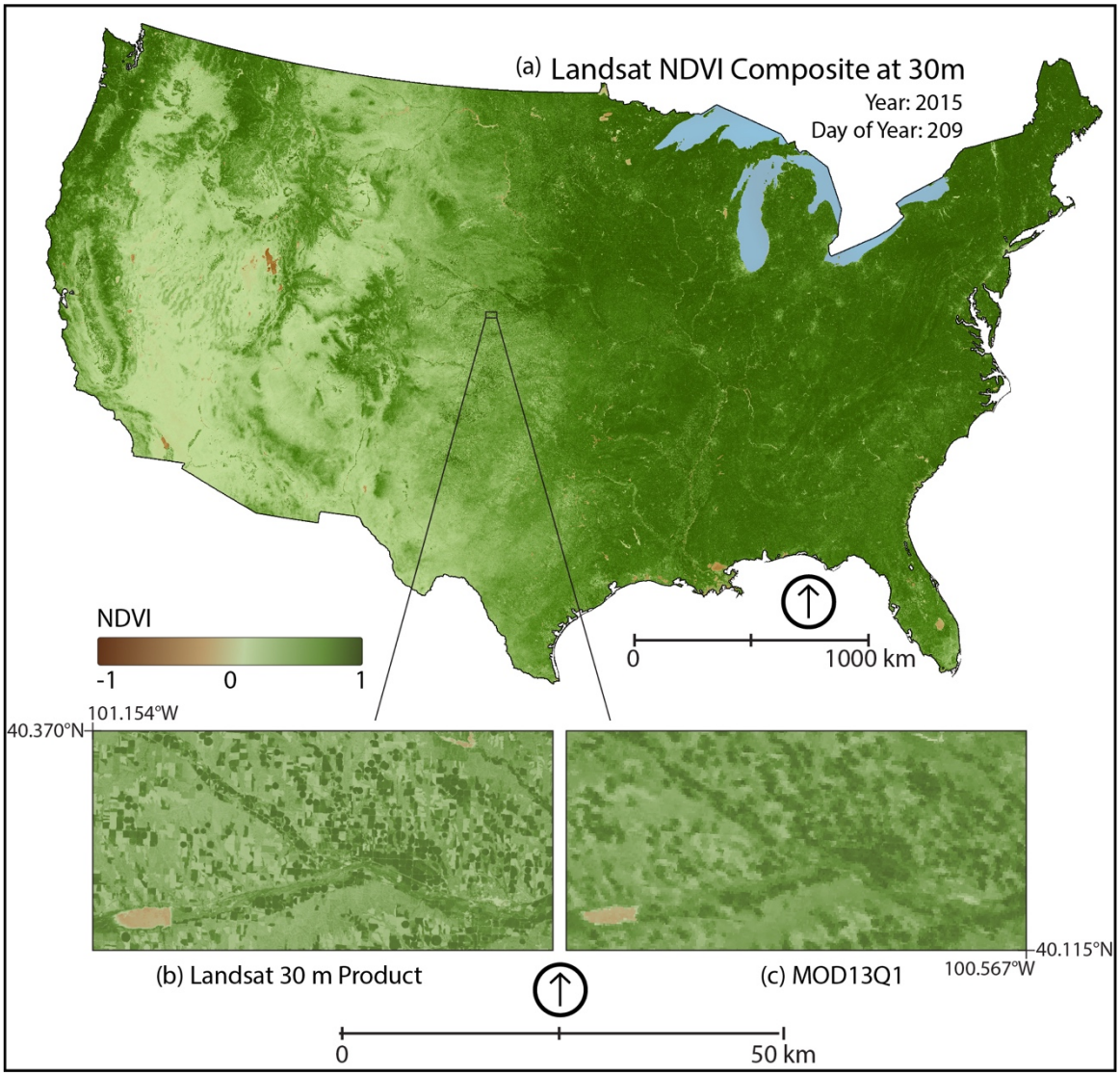

Figure 1.1 (a) A 30m continuous CONUS Landsat NDVI composite for July 28, 2015. Our methods produce broad scale composites with minimal gaps in data and reduce the effect of scene edges. Local scale comparison of (b) Landsat NDVI at 30 m and (c) MODIS MOD13Q1 at 250 m from the same composite period. The Landsat product provides added spatial detail important in measuring certain ecological processes.

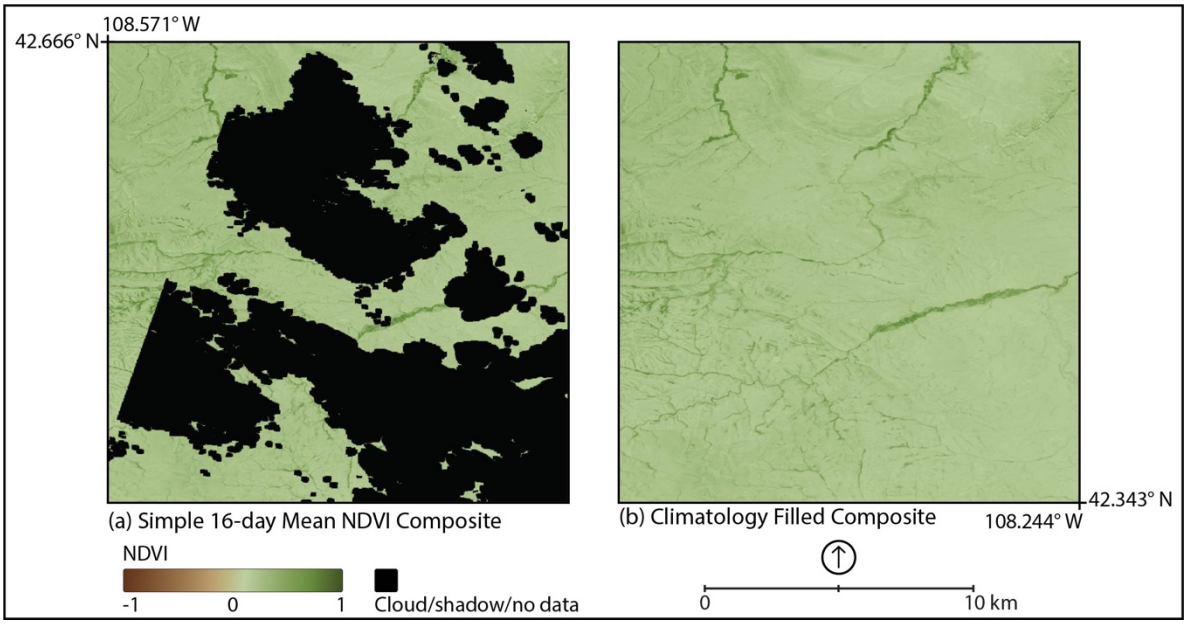

Figure 1.2 (a) A simple 16-day mean NDVI composite from July 28 to August 12, 2015 created from Landsat 7 and 8 sensors. The composite contains missing data due to cloud cover and scene edges are apparent due to differing acquisition dates. (b) A 16-day climatology (5-year) gap filled composite for the same time and location. The climatology is user defined in order to produce an appropriate composite for the question being asked.

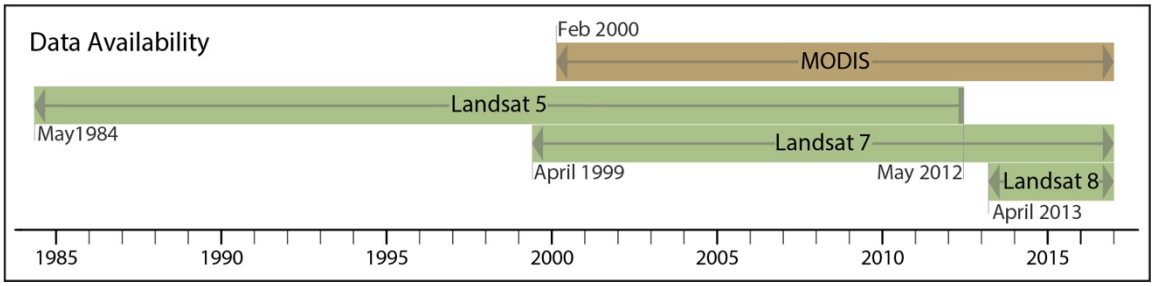

Figure 1.3 A timeline showing the data availability for Landsat NDVI, based upon Landsat surface reflectance products and MOD13Q1. The extended Landsat record provides a longer continuous record of high resolution NDVI.

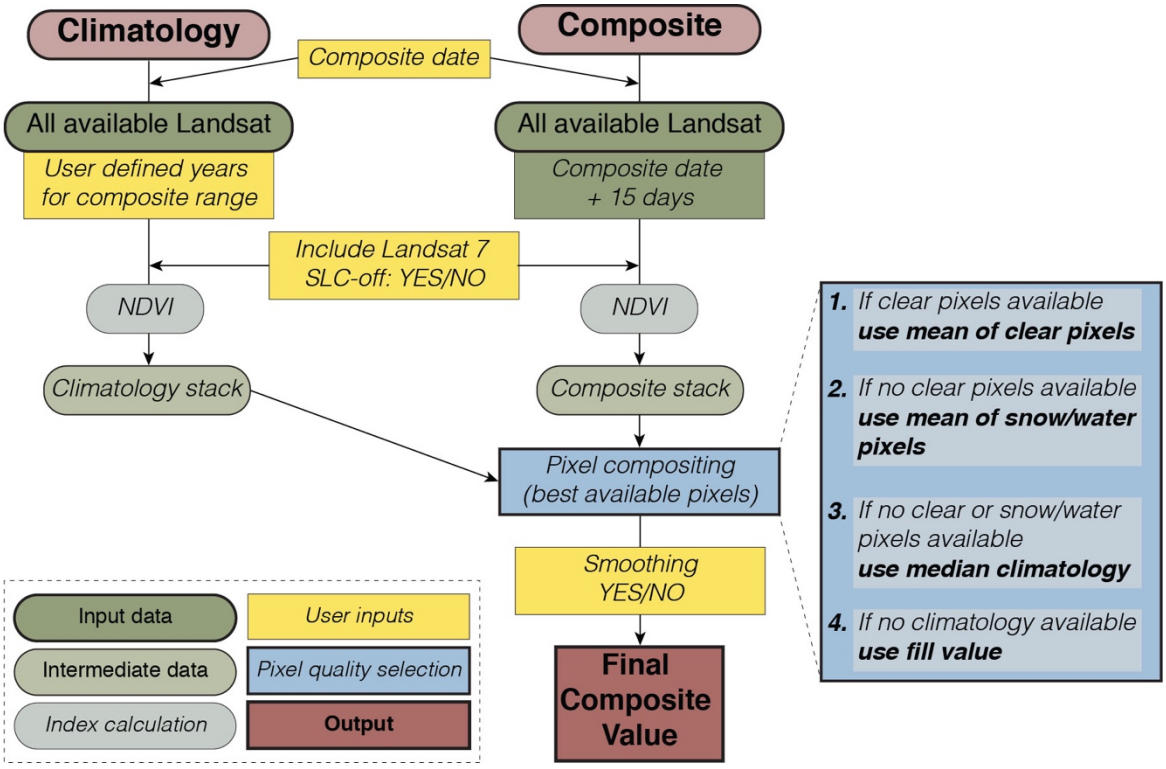

Figure 1.4 A flow chart demonstrating the NDVI compositing process, in which the best available pixels from all available Landsat sensors are selected and combined to produce the final NDVI composite value.

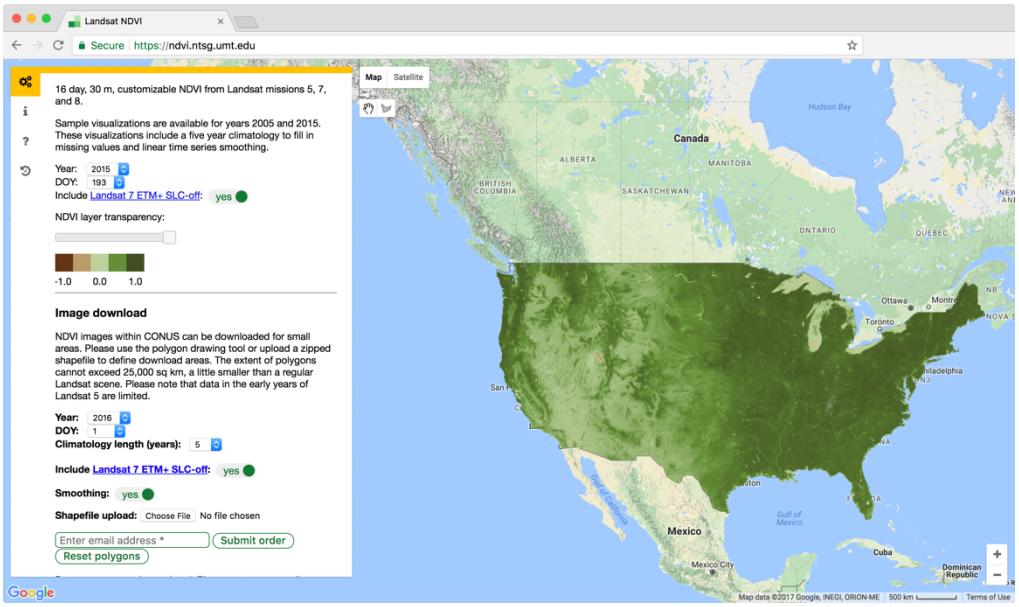

Figure 1.5 A screen shot of the NDVI web application (https://ndvi.ntsg.umt.edu). To download a composite, users set their desired parameters in the left panel. The region of interest can either be an uploaded shapefile or a polygon drawn directly on the map. The composite is processed on the fly and users are notified via email when it is ready to download.

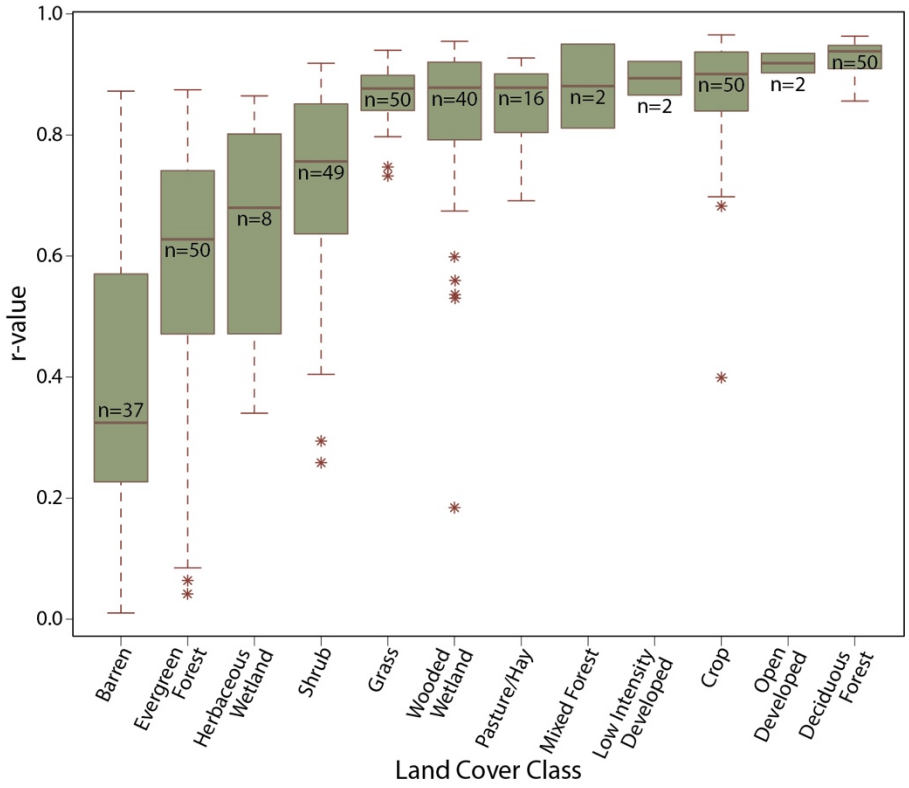

Figure 1.6 The distribution of Pearson correlation coefficients between MOD13Q1 NDVI and Landsat NDVI for each land cover class.

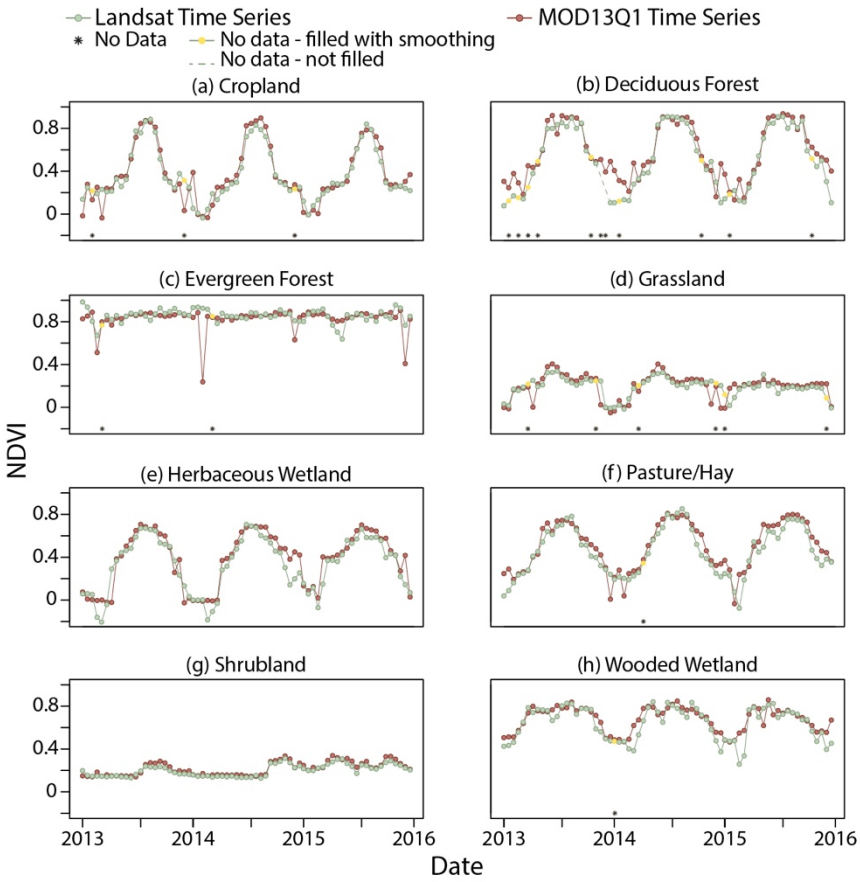

Figure 1.7 Time series of 30m Landsat NDVI and 250m MOD13Q1 NDVI time series from 2013 to 2015, separated by land cover class. After April 2013, the Landsat NDVI time series include data from both Landsat 7 and 8, while before April 2013 they included just Landsat 7 data. Each time series is from a single point, within a homogenous area (i.e., pixels where both Landsat and MOD13Q1 represent the same land cover), sampled at a location indicative of the major land cover classes.

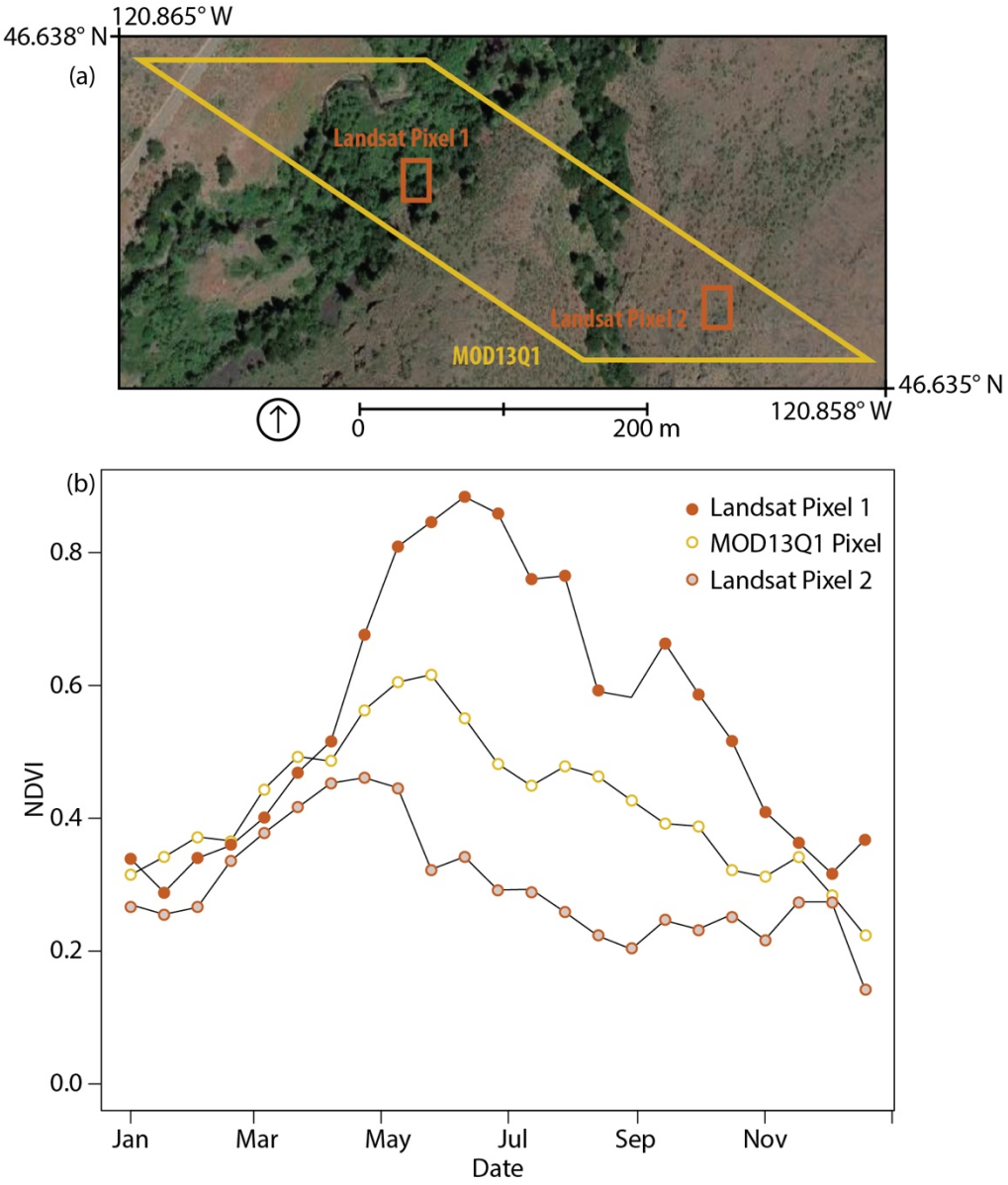

Figure 1.8 (a) Pixel locations in central Washington, USA. Landsat derived NDVI can provide increased detail in heterogeneous landscapes. The difference in pixel shape is due to native projections being transformed to a common projection. (b) Chart for 2015 of a Landsat derived NDVI and MOD13Q1 NDVI time series.

1.10 Supplemental Materials

Table 1.S1. List of PhenoCam sites and resulting Pearson correlation coefficients (r) comparing phenocam GCC90 to Landsat NDVI (16-day means). Plant Functional Type (PFT): DB - Deciduous Broadleaf; EN - Evergreen Needleleaf; GR - Grass; SH - Shrub; AG - Agriculture/Crop. Start date and End date indicate temporal extent used in correlations. Map ID corresponds to map labels in Figure 1.S1.

Site_Name	Pearson's r*	PFT	Start date	End date	Latitude	Longitude	Map ID
acadia	0.71	DB	3/15/07	12/31/15	44.37694	-68.26083	1
bartlett	0.87	DB	3/1/07	12/31/15	44.06460	-71.28810	2
bitterootvalley	0.86	DB	9/15/11	12/31/15	46.50700	-114.09100	3
bostoncommon	0.90	DB	5/6/10	12/31/15	42.35591	-71.06415	4
boundarywaters	0.83	DB	3/26/07	3/13/12	47.94670	-91.49551	5
butte	0.77	GR	1/6/09	12/31/15	45.95304	-112.47964	6
caryinstitute	0.79	DB	4/14/08	12/31/15	41.78390	-73.73410	7
coaloilpoint	0.85	GR	5/11/08	12/5/12	34.41370	-119.88023	8
coweeta	0.92	DB	4/14/11	12/31/15	35.05959	-83.42798	9
dollysods	0.84	DB	11/21/03	4/17/14	39.09953	-79.42704	10
drippingsprings	0.24	DB	4/6/01	5/26/09	33.30000	-116.80000	11
gatesofthemountains	0.44	GR	8/11/11	12/31/15	46.82620	-111.71070	12
harvard	0.88	DB	4/4/08	12/31/15	42.53780	-72.17150	13
howland1	0.60	EN	3/27/10	12/31/15	45.20410	-68.74030	14
hubbardbrook	0.83	DB	4/3/11	12/31/15	43.94380	-71.70100	15
joycekilmer	0.88	DB	6/6/06	3/27/15	35.25700	-83.79500	16
kaweah	0.46	SH	7/14/11	12/31/15	36.44350	-118.90925	17
mammothcave	0.80	DB	6/11/10	12/31/15	37.18583	-86.10194	18
monture	0.88	DB	11/4/10	12/31/15	47.02019	-113.12832	19
monture	0.86	GR	11/4/10	12/31/15	47.02019	-113.12832	20
morganmonroe	0.89	DB	8/27/08	12/31/15	39.32310	-86.41310	21
nationalcapital	0.44	DB	9/17/09	12/31/15	38.88818	-77.06950	22
niwot2	0.32	EN	10/2/09	7/16/15	40.03286	-105.54697	23
oakridge2	0.81	DB	1/17/08	12/31/15	35.93110	-84.33230	24
oregonMP	-0.16	EN	6/15/11	12/31/15	44.45230	-121.55740	25
pointreyes	0.38	SH	1/24/04	12/31/15	37.99639	-123.02111	26
proctor	0.89	DB	9/11/08	12/31/15	44.52500	-72.86600	27
sedgwick	0.75	GR	9/18/08	4/25/13	34.69685	-120.04840	28
sedgwick	-0.35	SH	9/18/08	4/25/13	34.69685	-120.04840	29
shenandoah	0.87	DB	9/14/09	12/31/15	38.61670	-78.35000	30
shiningrock	0.91	DB	9/15/09	12/31/15	35.39016	-82.77497	31
smokylook	0.87	DB	7/3/02	12/31/15	35.63253	-83.94311	32
smokypurchase	0.91	DB	7/3/08	12/31/15	35.59000	-83.07750	33
snakerivermn	0.74	DB	1/1/11	12/31/15	46.12056	-93.24467	34
teddy	0.82	GR	10/6/10	12/31/15	46.89472	-103.37750	35
thompsonfarm2N	0.87	DB	5/17/10	12/31/15	43.10860	-70.95050	36
thompsonfarm2N	0.88	EN	5/17/10	12/31/15	43.10860	-70.95050	37
tonzi	0.72	DB	10/26/11	12/31/15	38.43092	-120.96589	38
tonzi	0.86	GR	10/26/11	12/31/15	38.43092	-120.96589	39
uiefmaize	0.81	AG	11/5/08	12/31/15	40.06282	-88.19613	40

uiefmiscanthus	0.88	AG	11/11/08	12/31/15	40.06281	-88.19843	41
uiefprairie	0.68	GR	10/22/08	12/31/15	40.06369	-88.19729	42
uiefswitchgrass	0.76	AG	10/20/08	12/31/15	40.06369	-88.19729	43
umichbiological	0.90	DB	12/3/08	3/28/14	45.55984	-84.71382	44
vaira	0.89	GR	10/18/11	12/31/15	38.41328	-120.95064	45
windriver	0.41	EN	4/30/10	8/24/14	45.82128	-121.95208	46
woodshole	0.87	DB	4/14/11	12/31/15	41.54950	-70.64320	47

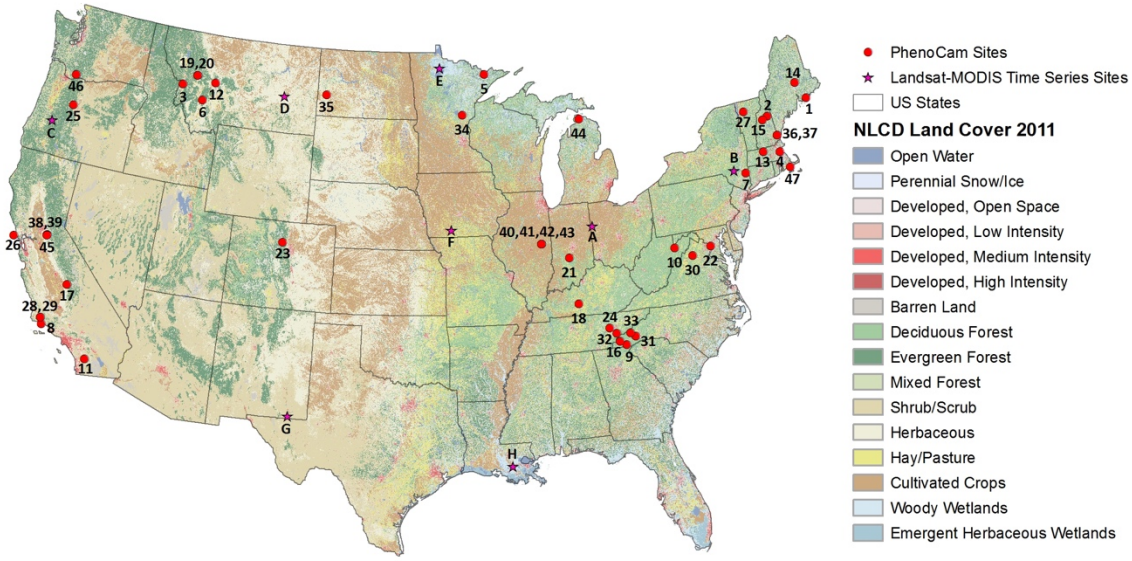

Figure 1.S1 (a) Map of phenocam locations.

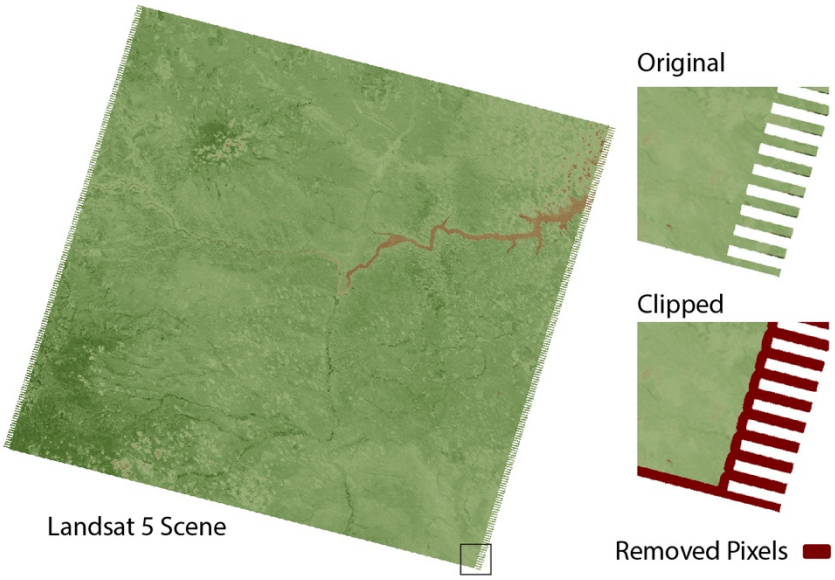

Figure 1.S2 (a) Landsat 5 edge removal illustration.

PhenoCam Site Acknowledgments

Camera images from Acadia National Park, National Capital Region, Point Reyes National Seashore, Great Smoky National Park, and Teddy Roosevelt National Park are provided courtesy of the National Park Service Air Resources Program. Camera images from the Bitterroot Valley, Superior National Forest, Dolly Sods Wilderness, Cleveland National Forest, Helena National Forest, Joyce Kilmer Slickrock Wilderness, Lolo National Forest, and Shining Rock Wilderness are provided courtesy of the USDA Forest Service Air Resources Management Program. Camera images from Kaweah are provided courtesy of the Sierra Wildland Fire Reporting System, National Park Service, and USDA Forest Service. Research at the Bartlett Experimental Forest tower is supported by the National Science Foundation (grant DEB-1114804) and the USDA Forest Service's Northern Research Station. Research at the Boston Common is supported by an Emerson College Faculty Advancement Funds Grant. Research at the Continental Divide PhenoCam Site in Butte, Montana is supported by the National Science Foundation-EPSCoR (grant NSF-0701906), OpenDap, Inc., and Montana Tech of the University of Montana. Research at the Coweeta flux tower is funded through the USDA Forest Service, Southern Research Station; USDA Agriculture and Food Research Initiative Foundational Program, award number 2012-67019-19484; EPA agreement number 13-IA-11330140-044; and the National Science Foundation, Long-Term Ecological Research (LTER) program, award #DEB-0823293. Research at Harvard Forest is partially supported through the National Science Foundation's LTER program (DEB-1237491), and Dept. of Energy Offfice of Science (BER). Research at Howland Forest is supported by the Office of Science (BER), US Department of Energy, and the USDA

Forest Service's Northern Research Station. Research at the Hubbard Brook Experimental Forest is partially supported by the National Science Foundation's LTER program (grant DEB-1114804) and the USDA Forest Service's Northern Research Station.

Research at the Morgan-Monroe Ameriflux site is supported by the US Department of Energy, Office of Science, Office of Biological and Environmental Research through the Ameriflux Management Project administered by Lawrence Berkeley National Lab. The US-NR1 AmeriFlux site is currently supported by the U.S. DOE, Office of Science through the AmeriFlux Management Project (AMP) at Lawrence Berkeley National Laboratory under Award Number 7094866. Research at Chestnut Ridge is funded by US Dept of Commerce, National Oceanic and Atmospheric Administration, Office of Atmospheric Research, Air Resources Lab, Atmospheric Turbulence and Diffusion Division as part of the Surface Energy Budget Network (SEBN). Support for US-Me2 is provided from the Metolius Core Site Cluster by the DOE Office of Science Ameriflux Network Management Project. Proctor Maple Research Station is supported by the Agricultural Experiment Station of the University of Vermont. Funding for the Shenandoah PhenoCam and related research has been provided by the U.S. Geological Survey Land Change Science Program (Shenandoah National Park Phenology Project) with logistical support from the National Park Service in collaboration with the University of Virginia Department of Environmental Science. Research at the Thompson Farm Observatory is supported by NH EPSCoR with support from the National Science Foundation's Research Infrastructure Improvement Award (#EPS 1101245) and by the NH Agricultural Experiment Station/USDA NIFA (Hatch project #1006997). Funding for AmeriFlux core site data at Tonzi Ranch was provided by the U.S. Department of

Energy's Office of Science. Research at the UIUC Energy Farm is supported by the Global Change and Photosynthesis Research Unit of the USDA Agricultural Research Service. Primary support for the University of Michigan AmeriFlux Core Site (US-UMB) provided by the Department of Energy Office of Science. Infrastructure support provided by the University of Michigan Biological Station. Data and logistical support at the Wind River site were provided by the US Forest Service Pacific Northwest Research Station and the University of Washington. Logistical support for the Woods Hole PhenoCam is provided by the Woods Hole Research Center.

CHAPTER 2: LANDSAT 30 M AND MODIS 250 M DERIVED TERRESTRIAL PRIMARY PRODUCTION FOR THE CONTERMINOUS UNITED STATES.

2.1 Introduction

A primary process in all terrestrial ecosystems is the flux of carbon through trophic levels. Considered a supporting ecosystem service, primary production provides the foundation for numerous other services, including food, fuel and fiber (Running *et al.*, 2000; Haberl *et al.*, 2007; Smith *et al.*, 2012a). Terrestrial gross primary production (GPP) is the total amount of carbon captured by plants while net primary production (NPP) is the carbon allocated to plant tissue after accounting for the costs of autotrophic respiration (Ruimy *et al.*, 1994). GPP and NPP thus represent the carbon removed from the atmosphere and the carbon available to other trophic levels, respectively (Field *et al.*, 1995). The spatiotemporal variability of GPP and NPP across the terrestrial surface is substantial, and is primarily affected by climate, land cover, disturbance, and land use practices (Piao *et al.*, 2009). Given the importance of GPP and NPP to ecosystem function and the capacity for humans to alter production via land use/land cover change and climate change, developing appropriate products for monitoring these processes has emerged as a key component of ecological research, conservation, and management.

GPP and NPP cannot be directly observed at broad scales and requires models based on biophysical factors and atmospheric dynamics (Cramer *et al.*, 1999; Scurlock *et al.*, 1999). Models that integrate remotely sensed-derived estimates of vegetation provide mechanisms for estimating, monitoring, and evaluating the spatiotemporal variability of terrestrial ecosystem production (Field *et al.*, 1995; Running *et al.*, 2000; Turner *et al.*, 2004). One of the primary remote sensing-based models of terrestrial GPP and NPP is the Moderate Resolution Imaging Spectroradiometer (MODIS) MOD17 algorithm (Running *et al.*, 2004; Sims *et al.*, 2008; Smith *et al.*, 2016). The MOD17 algorithm was originally

designed for global monitoring and is widely applied across ecology (Haberl *et al.*, 2007; Running, 2012; Smith *et al.*, 2012a, 2012b; DeLucia *et al.*, 2014). MOD17 products are currently the only regularly produced production products publicly available, with 8-day GPP and annual NPP estimates for the global vegetated surface at 1 km (version 5.5) and 500 m (version 6) spatial resolutions.

While the MOD17 product is widely utilized, tradeoffs between temporal resolution, spatial resolution, and spatial extent restrict its use and applicability in ecology and natural resource conservation and management (Turner *et al.*, 2003; Heinsch *et al.*, 2006; Sims *et al.*, 2008). Process based models like MOD17 are often computationally demanding and limited by computational processing and data storage capacity. To maintain global coverage, MOD17 inputs are spatially coarse, utilizing 0.5° (≈ 50 km) meteorological data, 500 m land cover classifications, and 500 m FPAR (fraction of photosynthetically active radiation), and LAI (leaf area index) estimates. The algorithm also relies on biome-specific parameters applied through a biome parameter look-up table (BPLUT). The BPLUT parameters are both parameterized and applied to biomes at the global scale, and thus do not capture variation within biomes (e.g., grasslands in North America use the same parameters as those in East Africa). While this simplification permits global estimations of terrestrial production, the coarse inputs and BPLUT approach attenuate ecologically important variation at finer scales (Running *et al.*, 2000; Zhao *et al.*, 2005; Neumann *et al.*, 2016).

The patterns and spatiotemporal variability of GPP and NPP across landscapes are the result of numerous processes occurring at multiple spatiotemporal scales. Many of these processes occur simultaneously at fine resolutions but across broad spatial extents.

Furthermore, human alteration and impact occurs at multiple scales. Discrete individual disturbances, small and potentially undetectable in isolation, can have substantial impacts when viewed cumulatively (Allred *et al.*, 2015). Land management activities (e.g., crop agriculture, grazing, or forestry) can occur at fine or broad spatial scales, as well as across long time periods. Due to its coarse resolution, the MOD17 product is generally ill-suited for evaluating production responses to finer-scale processes and impacts. To more effectively assess and monitor production, higher resolution products that balance the scales of observed patterns and underlying processes are needed.

Addressing some of the limitations of the MOD17 product, we develop two separate medium resolution (30 m and 250 m) GPP and NPP products for the CONUS region. As the MOD17 algorithm is not bound to the coarse input datasets, we replace input datasets with finer resolution and locally validated datasets, and optimize model parameters to reflect conditions specifically found within CONUS. We capitalize on advancements in cloud computing and parallel processing technologies to process historical Landsat and MODIS images alongside finer resolution meteorological data and land cover classifications to produce 30 m Landsat-derived GPP and NPP products from 1986 to 2016 (GPP_{L30} and NPP_{L30}) and 250 m MODIS-derived GPP and NPP products from 2001 to 2016 (GPP_{M250} and NPP_{M250}). We describe, evaluate, and emphasize the applicability of these two products, highlighting the capability to monitor terrestrial production at increased levels of spatial detail.

2.2 Methods

2.2.1 MOD17 OVERVIEW

To create both the MODIS and Landsat derived production products we utilize the established framework of the MOD17 algorithm (Figure 1). The theoretical basis for the MOD17 algorithm stems from original work by Monteith (1972), directly relating GPP and NPP to the amount of solar radiation absorbed by the plant canopy. Remotely sensed vegetation information is combined with light use efficiency logic and incident shortwave radiation to calculate daily GPP and after accounting for losses due to respiration, annual NPP.

The global input datasets of the MOD17 product are replaced with finer resolution datasets (Table 1). For the GPP/NPP_{M250} and GPP/NPP_{L30} products, we obtain meteorological inputs from the University of Idaho's 4-km gridded surface meteorological dataset, METDATA (Abatzoglou, 2013). The meteorological inputs used to calculate light use efficiency and scale rates of respiration are short wave radiation, daily minimum and maximum temperature, and vapor pressure deficit. Land cover classifications from 1992, 2001, 2006, and 2011 are used to apply biome specific constraints throughout the algorithm, and are obtained from the 30 m National Land Cover Database (NLCD) (Homer *et al.*, 2007, 2015; Fry *et al.*, 2011). For GPP/NPP_{M250}, FPAR and LAI are calculated from the MODIS surface reflectance product, MOD09Q1 (Vermote, 2015); for GPP/NPP_{L30}, FPAR and LAI are calculated from the Landsat surface reflectance products (Masek *et al.*, 2006; Feng *et al.*, 2012; Vermote *et al.*, 2016). We use established relationships of FPAR and LAI with the normalized difference

vegetation index (NDVI) (Choudhury, 1987; Sellers *et al.*, 1994; Peng *et al.*, 2012; Wang *et al.*, 2014).

As remotely sensed satellite data are inherently noisy due to atmospheric effects, cloud cover, data retrieval, and processing errors, a significant challenge is creating spatio-temporally continuous NDVI composites from which to calculate FPAR and LAI. The MOD09Q1 product is an 8-day global composite product that accounts for some of these underlying complexities. To account for temporal noise in the data, we smooth data gaps and unusually low NDVI values based on the iterative Interpolation for Data Reconstruction (IDR) method (Julien & Sobrino, 2010). Landsat data are more complex, due to an infrequent overpass interval, collection date differences between adjacent scenes, radiometric differences between missions, and various sensor malfunctions (e.g., Landsat 7 ETM+ scan line corrector error). Thus, we utilize a smoothing and climatology driven gap filling approach to create spatially continuous and temporal regular Landsat NDVI composites across CONUS (Robinson *et al.*, 2017). Detailed descriptions of these methods are provided in the supporting materials.

2.2.2 GPP

We use daily FPAR estimates, meteorological data, and the optimized parameter set to calculate daily GPP (Equation 1).

$$GPP = LUE_{max} \times f_{Tmin} \times f_{vpd} \times 0.45 \times SW_{rad} \times FPAR \quad (1)$$

LUE_{max} (g C MJ^{-1}) is a biome specific maximum potential light use efficiency and is attenuated by minimum temperature (f_{Tmin}) and vapor pressure deficit (f_{vpd}) scalars

(Figure 2.S1) to account for temperature and water stress, respectively. These scalars utilize other biome specific properties ($Tmin_{min}$, $Tmin_{max}$, VPD_{min} and VPD_{max}) to linearly scale the daily minimum temperature and daily vapor pressure deficit between 0 and 1. SW_{rad} (w m^{-2}) is incoming shortwave radiation, of which 45% is in wavelengths available for photosynthesis.

The original MOD17 BPLUT parameters represent global biomes and do not vary spatiotemporally. As the GPP products we develop are limited to CONUS, we optimize these parameters ($Tmin_{min}$, $Tmin_{max}$, VPD_{min} and VPD_{max}) with reference GPP estimates from eddy covariance flux towers within CONUS. We use tier one level data from the FLUXNET2015 dataset, containing data from 43 tower sites across CONUS. To avoid the inclusion of poor quality data, we only use flux towers with at least two years of data and select daily GPP observations flagged as high quality (quality flag >= 0.75) (Richardson *et al.*, 2010; Verma *et al.*, 2015). At some flux tower locations, there is a discrepancy in land cover as designated by the flux tower dataset and the dominant land cover as classified by the NLCD. To avoid flux towers in areas with heterogeneous land cover, towers are only included if more than 50% of the pixels within a one km buffer are classified as the dominant land cover based on the NLCD and match the given land cover classification of the flux tower. This results in 30 flux towers representing the range of land cover classes (Figure 2.S2; Table S1). Our optimization approach finds the parameter set (Table 2) that minimizes the residual sum of squares between model outputs and the corresponding flux tower GPP estimates for each land cover class (Turner *et al.*, 2006, 2009). We utilize a limited memory, quasi-Newton algorithm (L-BFGS-B)

for optimization (Byrd *et al.*, 1995; Santaren *et al.*, 2007), using original MOD17 BPLUT parameters as initialization values.

To quantify the improvements made through the parameter optimization process, we compare Pearson's correlation coefficients (r-values), root mean square error (RMSE), mean bias (MB), and mean absolute bias (MAB) calculated for daily GPP estimates using the original MOD17 parameters versus daily flux tower GPP estimates (GPP_{Flux}) and daily GPP estimates using the optimized parameter set versus GPP_{Flux}. To assess differences between the datasets, we compare the r-values, RMSE, MB and MAB for GPP_{M250}, GPP_{L30}, MOD17 GPP versus GPP_{Flux}. As the MOD17 product is an 8-day product, we match GPP_{M250}, GPP_{L30} and GPP_{Flux} to the temporal granularity of MOD17. Eight day periods with less than four valid flux tower observations are discarded.

2.2.3 NPP

Daily estimates of LAI, meteorological data, and the relevant MOD17 algorithm BPLUT parameters are used to calculate daily maintenance respiration (MR). The logic and parameters are based on allometric relationships between estimated leaf area, leaf mass, fine root mass, and live wood mass. Annual NPP (Equation 2) is calculated as the sum of the daily differences between GPP and MR minus annual growth respiration (GR).

$$NPP = \sum_{i=day\ 1}^{365}(GPP_i - MR_i) - GR \quad (2)$$

To assess the quality of NPP_{M250} and NPP_{L30} estimates, we compare cumulative NPP, separated by land cover, across CONUS to the MOD17 product. Detailed methods for GPP and NPP are provided in the supporting materials.

2.2.4 PRODUCTS

GPP_{M250} is an 8-day cumulative estimate (kg C m^{-2} 8-$days^{-1}$) of GPP that matches the temporal resolution of the MOD17A2 GPP product; GPP_{L30} is a 16-day cumulative GPP estimate (kg C m^{-2} 16-$days^{-1}$). Both GPP products begin on day one of a given year and end on day 361 (MODIS derived 8-day) or 353 (Landsat derived 16-day). Each GPP composite includes the composite date and 7 or 15 ensuing days. The final period of each year is restricted to 5 days (6 days in a leap year) for GPP_{M250} and to 13 days (14 days in a leap year) for GPP_{L30}. The NPP_{M250} and NPP_{L30} are estimates of annual NPP (kg C m^{-2} $year^{-1}$). Data are scaled by 10,000 and stored as a 16-bit integer. Each of the products contain a QC band providing information regarding the underlying NDVI estimate for each pixel (Table 3). We utilize Google Earth Engine (Gorelick *et al.*, 2016) for data processing, product creation and product distribution.

2.3 Results

2.3.1 GPP ASSESSMENT

Incorporating optimized parameters into Landsat and MODIS derived GPP improves estimates compared to the original MOD17 algorithm parameter set (Figure 2). Across all flux tower sites combined, r-values increased from 0.60 to 0.79 (GPP_{M250}) and from 0.63 to 0.80 (GPP_{L30}), while RMSE values decreased from 4.33 to 2.84 (GPP_{M250}) and from 4.25 to 2.91 (GPP_{L30}). Analysis of flux towers aggregated by land cover also produced

improved results for most land cover classes (Figure 3; Table 4). Deciduous broadleaf (DBF) sites improved the most with r-values increasing from 0.55 to 0.85 (GPP_{M250}) and from 0.57 to 0.88 (GPP_{L30}) and RMSE decreasing from 5.11 to 2.56 (GPP_{M250}) from 4.91 to 2.33 (GPP_{L30}). Shrubland (SH) sites revealed little change with optimized parameter sets, with decreases in RMSE values from 1.05 to 0.97 (GPP_{M250}) and from 1.13 to 1.01 (GPP_{L30}) and decreases in r-values from 0.74 to 0.72 (GPP_{M250}) and from 0.71 to 0.68 (GPP_{L30}). Of the six shrubland sites, five (44 of 46 site-years) are in semi-arid regions of Arizona and Utah. The shrubland class constitutes a diverse functional group, and this diversity is poorly represented in this clustering. Eddy covariance flux measurements in semi-arid areas often include significant components of abiotic CO_2 fluxes, which may result in the overestimation of GPP_{Flux} using traditional flux partitioning procedures (Serrano‐Ortiz *et al.*, 2014).

When comparing to GPP_{Flux}, both GPP_{M250} and GPP_{L30} showed improvements over MOD17 GPP across all land cover classes except cropland (Table 5). Excluding croplands, the r-values improved from 0.91 (MOD17) to 0.94 (GPP_{M250}) and 0.93 (GPP_{L30}), while the RMSE decreased from 1.49 (MOD17) to 1.29 (GPP_{M250}) and 1.31 (GPP_{L30}). Seasonally, the temporal profiles of modelled GPP track the profiles of flux tower GPP (Figure 4). Across most flux towers, GPP_{M250} and GPP_{L30} correspond more closely to GPP_{Flux} than the MOD17 product GPP. The most notable discrepancies are in cropland sites, where all models tend to underestimate peak flux tower GPP (Figure 4D). The poor performance of MOD17 within croplands is well documented and improved methods are needed to capture the wide variation of parameters across crop types (Chen

et al., 2011) and nonlinearities between LUE and GPP within croplands (Guanter *et al.*, 2014; Wood *et al.*, 2017).

2.3.2 NPP ASSESSMENT

Comparing total annual NPP across CONUS (Table 6), we find high correlations between both NPP_{M250} and NPP_{L30} relative to the MOD17 product (NPP_{M250} r-value: 0.82; NPP_{L30} r-value: 0.81). From 2001 to 2014, average annual NPP from the MOD17 product is estimated at 3.09 petagrams (Pg; 10^{15} g) of carbon while for the NPP_{M250} NPP_{L30} it is 4.49 Pg and 3.03 Pg, respectively. When compared to the MOD17 product, NPP_{M250} is 41-50% higher, while NPP_{L30} is 1.7 to 2.0% lower. The relatively high NPP_{M250} estimates are largely caused by differences in the parameterization of LUE_{max} for croplands (Table 2). While comparing the total absolute values of NPP across a region is useful for general validation purposes, discrepancies between models are expected due to the utilization of different input datasets and parameterization. More informative is the degree to which each product tracks interannual variability of total NPP. We find consistent interannual variability and seasonal magnitudes across all three NPP products for all land cover classes (Figure 5). The only notable exception occurs in the shrubland class (SH), where NPP_{L30} shows higher deviations from the mean in 2004 and 2012. NPP_{M250} and NPP_{L30} consistently underestimate NPP across shrublands compared to the MOD17 product, likely originating from an underestimation of GPP (see *GPP Assessment*) or an overestimation of respiration (see *Strengths, Challenges, and the Future*).

2.4 Discussion

We produce 30 meter and 250 meter GPP and NPP products for CONUS that better capture the spatiotemporal variability of terrestrial production than currently available coarser resolution products (Figure 2.6). Accounting for this variability reveals changes in production dynamics, particularly important for smaller scale monitoring, conservation, and land management (see case studies below and Figures 2.7-2.9). By optimizing the parameters with GPP data from FLUXNET2015 towers located within CONUS and using improved land cover and climate data specific to CONUS, we further refine the algorithm to more accurately reflect regionally unique conditions.

2.4.1 VALUE FOR CONSERVATION AND MANAGEMENT

Remotely sensed GPP and NPP extend satellite imagery beyond commonly used vegetation indices or land cover change. Production, measured in units of carbon, allows for assessing ecosystem dynamics in ecological, economical, and socially relevant terms (Vitousek *et al.*, 1986; Haberl *et al.*, 2004; Crabtree *et al.*, 2009). Better understanding–specifically with improved spatial resolution–of how land use activities affect carbon dynamics is critical in an era where climate change poses a massive challenge. Production also provides a foundation for process based models used to estimate ecosystem services, such as cropland agriculture (McGuire *et al.*, 2001; Monfreda *et al.*, 2008), forest stand biomass biomass (Keeling & Phillips, 2007; Hasenauer *et al.*, 2012), or rangeland forage (Hunt & Miyake, 2006; Reeves *et al.*, 2006). As many of the conservation or management activities associated with these and other ecosystem services occur at finer scales across landscapes, medium resolution products are necessary for

assessment and monitoring. Built into decision frameworks, production information can help managers better understand the dynamics, impacts, and tradeoffs of their management. Quantifying conservation outcomes, e.g., management practices, restoration activities, etc., at fine resolutions, across broad spatial extents, and in relevant ecological terms (biomass, carbon), is essential in evaluation and adaptive management. We provide three examples highlighting the benefits of production estimates at increased spatial resolution and their utility for conservation and management.

2.4.2 FIRE

Fire affects a large proportion of grasslands, shrublands, and forests across the United States, fulfilling a critical ecological role in shaping these ecosystems (White, 1979; Oliver, 1980; Axelrod, 1985). Fire activity has increased due to plant invasions, changes in climate, and increased human activity (Westerling *et al.*, 2006; Bowman *et al.*, 2009; Balch *et al.*, 2013). Fire is also a fundamental component of the global carbon cycle, releasing carbon through combustion or in the absence of fire, sequestering it as biomass (Seiler & Crutzen, 1980; Andreae & Merlet, 2001; Bond *et al.*, 2005). Burned areas exhibit patterns of burn severity, related to topographic, meteorological, and pre-fire biomass dynamics (White *et al.*, 1996). Burning directly influences production at fine scales, often with short-term immediate increases in grasslands (Knapp & Seastedt, 1986; Blair, 1997) and longer recovery times in forests (Amiro *et al.*, 2000; Hicke *et al.*, 2003; Goetz *et al.*, 2006), varying with burn severity (White *et al.*, 1996).

We demonstrate fire-production dynamics at multiple scales utilizing burn severity data (Eidenshink *et al.*, 2007) from a grassland (Lund fire, North Dakota, 2006) and a forested

(Horse Creek fire, Wyoming, 2007) system (Figure 7). In both systems, patterns between burn severity and NPP are detectable at finer resolutions, but these patterns diminish as spatial resolution becomes coarser. Using both NPP_{M250} and NPP_{L30}, the grassland fire shows a positive relationship between burn severity and production (pre- and post-fire), indicating that more production resulted in greater burn severity, and that greater burn severity resulted in greater production post fire, a common occurrence in grasslands (Knapp & Seastedt, 1986; Blair, 1997). The coarser resolution MOD17 product shows little variation in production pre- or post-fire across burn severity levels. The forested system shows no detectable pattern between burn severity and pre-fire production across all NPP products, hinting at stability and spatial homogeneity. Post-fire dynamics, however, reveal a negative relationship between burn severity and production with NPP_{M250} and NPP_{L30}, demonstrating that areas which burned less severely retained or recovered production while areas with greater burn severity had yet to recover. These dynamics and relationships were not present with the coarser resolution MOD17 product. To better understand the nuanced relationships between fire and productivity across broad scales, medium to high spatial resolution products are needed, as well as datasets that extend further back in time.

2.4.3 DEVELOPMENT

Anthropogenic land transformation occurs in many forms and substantially affects the Earth's biological systems and processes (Imhoff *et al.*, 2004; Metzger *et al.*, 2006). Approximately one half of the terrestrial surface has been altered by human activity (Vitousek *et al.*, 1997), with 55% of the annual primary production being appropriated by

humans (Vitousek *et al.*, 1986; Haberl *et al.*, 2004, 2007; Mustard *et al.*, 2012). Many forms of human induced land transformation, such as urbanization and development, are especially disruptive as they greatly reduce or eliminate the photosynthetic capacity of land area where they occur (Wackernagel & Yount, 1998; Wackernagel *et al.*, 2002; Imhoff *et al.*, 2004). Development such as transportation networks, communication and energy infrastructure, or residential housing often occurs at fine spatial resolutions across broad spatiotemporal extents. Medium and high spatial resolution products allow for the assessment of these finer scale, localized disturbances which are often missed with coarser products.

Rapid energy development across the United States is a major driver of land use change (McDonald *et al.* 2009, Trainor *et al.* 2016). The cumulative impacts of these developments, specifically on terrestrial production, is substantial but difficult to assess due to their broad geographic extent and the scale mismatch between the disturbances and products (Allred *et al.*, 2015). Examining a well site in New York, drilled in 2006, both the MOD17 (500 m) and NPP_{M250} products fail to detect discrete losses in NPP caused by disturbance at this scale, while the NPP_{L30} product detects a 68% loss in mean NPP (Figure 8). The NPP_{L30} product improves the tracking and accounting of these discrete losses while also extending the historical record.

2.4.4 RESTORATION

Restoration activities, aimed to repair degraded systems, are often central to conservation practices (Hobbs & Norton, 1996). While the aims and scope of restoration activities vary in objective, complexity, size, cost, etc., they often target restoring natural processes–

commonly at localized sites–with the goal of returning ecosystem structure and function to its pre-degraded state (Jackson *et al.*, 1995). Across the semi-arid western United States, riparian restoration activities are common, re-establishing the linkages between hydrologic processes to broader ecosystem function (Kauffman *et al.*, 1997) and include activities such as stream channel engineering, grazing management, and vegetation rehabilitation. Restoring ecosystem structure and function in riparian zones often improves production and is considered an indicator of success (Ehrenfeld & Toth, 1997).

In the early 1990s, Maggie Creek (a tributary to the Humboldt River in north-central Nevada) underwent comprehensive restoration efforts aimed at restoring riparian area habitat and production. Activities included changes in grazing management, fencing, and culvert replacement (Elliott *et al.*, 2004; Huntington *et al.*, 2016). Maggie Creek is relatively small, with a narrow riparian area often less than 150 m wide and is surrounded by semi-arid shrubland. Due to the timing (early 1990s) and scale of restoration activities, coarser MODIS based NPP products are inadequate for evaluating this restoration. Using the NPP_{L30} product, we detect measurable differences in NPP within the narrow riparian zone after restoration (Figure 9). As the higher resolution GPP and NPP products more closely match the scales at which many conservation and management actions take place, they provide expanded capacity for conservationists and managers to monitor and evaluate activities.

2.4.5 STRENGTHS, CHALLENGES, AND THE FUTURE

The Landsat (30 m) and MODIS (250 m) derived products have specific applications they are best suited for. The finer resolution of Landsat sensors allows for more detailed examination of production dynamics and responses to human activities that are largely absent in coarser products. The historical Landsat archive adds another 15+ years to that available with MODIS, permitting longer trend analysis. Landsat derived production (GPP_{L30} and NPP_{L30}) is best suited for detailed, smaller scale assessments where responses or trends of localized areas are desired. The 16-day return interval of satellites and temporal offset between adjacent orbital paths, however, can create discontinuous data across broad scales. Although the compositing and gap filling mitigates much of the resulting effects and artefacts, they do not eliminate them. The daily overpass of MODIS sensors make MODIS derived estimates of production well suited for analysis across broad geographic regions or continental analysis. MODIS derived production (GPP_{M250} and NPP_{M250}) minimizes atmospheric and cloud contamination; increases resolution from 500 to 250 m relative to the MOD17 product, permitting examination of some of the finer scale processes and responses (Figure 6); and follows the same 8-day schedule of the MOD17 product. Users should examine both products before application to determine which is appropriate for their needs.

Despite the noted improvements and added utility of the high-resolution products, some of the simplifying assumptions and limitations of the MOD17 algorithm itself are maintained in our methods. First, there is an unmeasured propagation of errors, stemming from the underlying accuracy and mismatched resolution of input datasets. Second, the biome specific parameters do not vary spatiotemporally and are applied through

temporally discrete land cover datasets, which may not reflect rapid land cover change. Third, the optimization process is based on a limited and clustered network of flux tower data. Due to the sparse data across representative land cover classes, independent samples were unavailable for validation. While users should be aware of these limitations, these are key areas for future research and product development. For example, strategies to incorporate the spatiotemporal variability of key parameters or to more accurately represent land cover through time at sub-pixel levels are promising approaches for improvement (Madani *et al.*, 2014; Yang *et al.*, 2015). Additionally, respiration is a key source of uncertainty in the NPP algorithm (Figure 1B), as it is calculated independently from GPP and utilizes biome level allometric relationships (Turner *et al.*, 2005; Zhang *et al.*, 2009). Simplifying respiration to a fixed proportion of GPP can avoid associated uncertainties (DeLucia *et al.*, 2007; Zhang *et al.*, 2009; Van Oijen *et al.*, 2010). A fixed ratio reduces the interannual variability of NPP across land cover classes and removes the NPP anomalies in shrublands and deciduous forest (Figure 2.S4, Table 2.S3).

Emerging big data technologies and geospatial applications (e.g., Apache Spark, Google Earth Engine, etc.) enable new and dynamic approaches to geospatial product creation and distribution. A barrier to using Landsat or other fine resolution data is the access, retrieval, storage, and manipulation of images. As the spatiotemporal extents increase, so do data volume and compute processing needs, making it difficult or impractical to those without access to high performance computing facilities and the skills to work with such systems. We overcame these barriers and limitations by implementing the MOD17 algorithm in Google Earth Engine. The structure of Google Earth Engine creates the ability to incorporate data from multiple sensors and datasets to build even more robust

products. What we accomplish with multiple Landsat sensors can be extended to include even higher resolution sensors, such as Sentinel-2. However, the real power of these new platforms and technologies is the ability to create customizable and dynamic geospatial products (Robinson *et al.*, 2017). When algorithms are programmed into a web application, model parameters and input datasets can be customizable so that users not satisfied with the standard parameters or other inputs can modify them based on *a priori* knowledge. For example, a user working with a web application that utilizes the MOD17 algorithm to estimate productivity can correct misclassified pixels in land cover datasets, or select between standard approaches or fixed ratios to calculate respiration used in NPP. Models can be tuned for specific regions or environmental conditions, providing locally optimized products that are more appropriate for a given system or question.

The new Landsat (30 m; 1986 to 2016) and MODIS (250 m; 2001 to 2016) derived primary production products provide new opportunities in the study of production dynamics and variability. Of significance is the ability to utilize these datasets for conservation and management, as the scales of both the product and the conservation/management activities are now better aligned. These enhancements will advance the study of terrestrial primary production, enable future refinements, and generate new applications of vegetation productivity measures.

2.5 Acknowledgements

We thank the Google Earth Engine developers for their support and technical advice. This work was funded through a Google Earth Engine Research Award and by the NRCS Wildlife Conservation Effects Assessment Project and Sage Grouse Initiative. This work

used eddy covariance data acquired and shared by the FLUXNET community, including these networks: AmeriFlux, AfriFlux, AsiaFlux, CarboAfrica, CarboEuropeIP, CarboItaly, CarboMont, ChinaFlux, Fluxnet-Canada, GreenGrass, ICOS, KoFlux, LBA, NECC, OzFlux-TERN, TCOS-Siberia, and USCCC. The ERA-Interim reanalysis data are provided by ECMWF and processed by LSCE. The FLUXNET eddy covariance data processing and harmonization was carried out by the European Fluxes Database Cluster, AmeriFlux Management Project, and Fluxdata project of FLUXNET, with the support of CDIAC and ICOS Ecosystem Thematic Center, and the OzFlux, ChinaFlux and AsiaFlux offices.

2.6 References

Abatzoglou JT (2013) Development of gridded surface meteorological data for ecological applications and modelling. *International Journal of Climatology*, **33**, 121–131.

Allred BW, Smith WK, Twidwell D, Haggerty JH, Running SW, Naugle DE, Fuhlendorf SD (2015) Ecosystem services lost to oil and gas in North America. *Science*, **348**, 401–402.

Amiro BD, Chen JM, Liu J (2000) Net primary productivity following forest fire for Canadian ecoregions. *Canadian Journal of Forest Research*, **30**, 939–947.

Andreae MO, Merlet P (2001) Emission of trace gases and aerosols from biomass burning. *Global Biogeochemical Cycles*, **15**, 955–966.

Axelrod DI (1985) Rise of the grassland biome, central North America. *The Botanical Review; Interpreting Botanical Progress*, **51**, 163–201.

Balch JK, Bradley BA, D'Antonio CM, Gómez-Dans J (2013) Introduced annual grass increases regional fire activity across the arid western USA (1980–2009). *Global Change Biology*, **19**, 173–183.

Blair JM (1997) Fire, N availability, and plant response in grasslands: A test of the transient maxima hypothesis. *Ecology*, **78**, 2359–2368.

Bond WJ, Woodward FI, Midgley GF (2005) The global distribution of ecosystems in a world without fire. *The New Phytologist*, **165**, 525–537.

Bowman DMJS, Balch JK, Artaxo P *et al.* (2009) Fire in the earth system. *Science*, **324**, 481–484.

Byrd RH, Lu P, Nocedal J, Zhu C (1995) A limited memory algorithm for bound constrained optimization. *SIAM Journal on Scientific Computing*, **16**, 1190–1208.

Chen T, van der Werf GR, Dolman AJ, Groenendijk M (2011) Evaluation of cropland maximum light use efficiency using eddy flux measurements in North America and Europe. *Geophysical Research Letters*, **38**, L14707.

Choudhury BJ (1987) Relationships between vegetation indices, radiation absorption, and net photosynthesis evaluated by a sensitivity analysis. *Remote Sensing of Environment*, **22**, 209–233.

Crabtree R, Potter C, Mullen R *et al.* (2009) A modeling and spatio-temporal analysis framework for monitoring environmental change using NPP as an ecosystem indicator. *Remote Sensing of Environment*, **113**, 1486–1496.

Cramer W, Kicklighter DW, Bondeau A *et al.* (1999) Comparing global models of terrestrial net primary productivity (NPP): overview and key results. *Global Change Biology*, **5**, 1–15.

DeLucia EH, Drake JE, Thomas RB, Gonzalez-Meler M (2007) Forest carbon use efficiency: is respiration a constant fraction of gross primary production? *Global Change Biology*, **13**, 1157–1167.

DeLucia EH, Gomez-Casanovas N, Greenberg JA *et al.* (2014) The theoretical limit to plant productivity. *Environmental Science & Technology*, **48**, 9471–9477.

Ehrenfeld JG, Toth LA (1997) Restoration ecology and the ecosystem perspective. *Restoration Ecology*, **5**, 307–317.

Eidenshink J, Schwind B, Brewer K, Zhu ZL, Quayle B, Howard S (2007) A project for monitoring trends in burn severity. *Fire Ecology*, **58**, 28–34.

Elliott J, Haskins RL, Weller G (2004) *Lahontan cutthroat trout species management plan for the upper Humboldt River drainage basin*. State of Nevada, Department of Wildlife.

Feng M, Huang C, Channan S, Vermote EF, Masek JG, Townshend JR (2012) Quality assessment of Landsat surface reflectance products using MODIS data. *Computers & Geosciences*, **38**, 9–22.

Field CB, Randerson JT, Malmström CM (1995) Global net primary production: Combining ecology and remote sensing. *Remote Sensing of Environment*, **51**, 74–88.

Fry JA, Xian G, Jin S *et al.* (2011) Completion of the 2006 national land cover database for the conterminous United States. *Photogrammetric Engineering and Remote Sensing*, **77**, 858–864.

Goetz SJ, Fiske GJ, Bunn AG (2006) Using satellite time-series data sets to analyze fire disturbance and forest recovery across Canada. *Remote Sensing of Environment*, **101**, 352–365.

Gorelick N, Hancher M, Dixon M, Ilyushchenko S, Thau D, Moore R (2016) Google Earth Engine: Planetary-scale geospatial analysis for everyone. *Remote Sensing of Environment*.

Guanter L, Zhang Y, Jung M *et al.* (2014) Global and time-resolved monitoring of crop photosynthesis with chlorophyll fluorescence. *Proceedings of the National Academy of Sciences*, **111**, E1327–E1333.

Haberl H, Schulz NB, Plutzar C *et al.* (2004) Human appropriation of net primary production and species diversity in agricultural landscapes. *Agriculture, Ecosystems & Environment*, **102**, 213–218.

Haberl H, Erb KH, Krausmann F *et al.* (2007) Quantifying and mapping the human appropriation of net primary production in earth's terrestrial ecosystems. *Proceedings of the National Academy of Sciences of the United States of America*, **104**, 12942–12947.

Hasenauer H, Petritsch R, Zhao M, Boisvenue C, Running SW (2012) Reconciling satellite with ground data to estimate forest productivity at national scales. *Forest Ecology and Management*, **276**, 196–208.

Heinsch FA, Zhao M, Running SW *et al.* (2006) Evaluation of remote sensing based terrestrial productivity from MODIS using regional tower eddy flux network observations. *IEEE Transactions on Geoscience and Remote Sensing **44**, 1908–* 1925.

Hicke JA, Asner GP, Kasischke ES *et al.* (2003) Post fire response of North American boreal forest net primary productivity analyzed with satellite observations. *Global Change Biology*, **9**, 1145–1157.

Hobbs RJ, Norton DA (1996) Towards a conceptual framework for restoration ecology. *Restoration Ecology*, **4**, 93–110.

Homer C, Dewitz J, Fry J *et al.* (2007) Completion of the 2001 national land cover database for the conterminous United States. *Photogrammetric Engineering and Remote Sensing*, **73**, 337.

Homer CG, Dewitz JA, Yang L *et al.* (2015) Completion of the 2011 National Land Cover Database for the conterminous United States-Representing a decade of land cover change information. *Photogrammetric Engineering and Remote Sensing*, **81**, 345–354.

Hunt ER, Miyake BA (2006) Comparison of stocking rates from remote sensing and geospatial data. *Rangeland Ecology & Management*, **59**, 11–18.

Huntington J, McGwire K, Morton C *et al.* (2016) Assessing the role of climate and resource management on groundwater dependent ecosystem changes in arid environments with the Landsat archive. *Remote Sensing of Environment*, **185**, 186–197.

Imhoff ML, Bounoua L, DeFries R, Lawrence WT, Stutzer D, Tucker CJ, Ricketts T (2004) The consequences of urban land transformation on net primary productivity in the United States. *Remote Sensing of Environment*, **89**, 434–443.

Jackson LL, Lopoukhine N, Hillyard D (1995) Ecological restoration: A definition and comments. *Restoration Ecology*, **3**, 71–75.

Julien Y, Sobrino JA (2010) Comparison of cloud-reconstruction methods for time series of composite NDVI data. *Remote Sensing of Environment*, **114**, 618–625.

Kauffman JB, Beschta RL, Otting N, Lytjen D (1997) An ecological perspective of riparian and stream restoration in the western United States. *Fisheries*, **22**, 12–24.

Keeling HC, Phillips OL (2007) The global relationship between forest productivity and biomass. *Global Ecology and Biogeography*, **16**, 618–631.

Knapp AK, Seastedt TR (1986) Detritus accumulation limits productivity of tallgrass prairie. *Bioscience*, **36**, 662–668.

Madani N, Kimball JS, Affleck DLR *et al.* (2014) Improving ecosystem productivity modeling through spatially explicit estimation of optimal light use efficiency. *Journal of Geophysical Research: Biogeosciences*, **119**, 2014JG002709.

Masek JG, Vermote EF, Saleous NE *et al.* (2006) A Landsat surface reflectance dataset for North America, 1990-2000. *IEEE Geoscience and Remote Sensing Letters*, **3**, 68–72.

McGuire AD, Sitch S, Clein JS *et al.* (2001) Carbon balance of the terrestrial biosphere in the Twentieth Century: Analyses of CO2, climate and land use effects with four process-based ecosystem models. *Global Biogeochemical Cycles*, **15**, 183–206.

Metzger MJ, Rounsevell MDA, Acosta-Michlik L, Leemans R, Schröter D (2006) The vulnerability of ecosystem services to land use change. *Agriculture, Ecosystems & Environment*, **114**, 69–85.

Monfreda C, Ramankutty N, Foley JA (2008) Farming the planet: 2. Geographic distribution of crop areas, yields, physiological types, and net primary production in the year 2000. *Global Biogeochemical Cycles*, **22**, GB1022.

Monteith JL (1972) Solar radiation and productivity in tropical ecosystems. *The Journal of Applied Ecology*, **9**, 747–766.

Mustard JF, Defries RS, Fisher T, Moran E (2012) Land-use and land-cover change pathways and impacts. In: *Land Change Science* (eds Gutman G *et al.*), pp. 411–429. Springer Netherlands.

Neumann M, Moreno A, Thurnher C *et al.* (2016) Creating a regional MODIS satellite-driven net primary production dataset for European forests. *Remote Sensing*, **8**, 554.

Oliver CD (1980) Forest development in North America following major disturbances. *Forest Ecology and Management*, **3**, 153–168.

Peng D, Zhang B, Liu L (2012) Comparing spatiotemporal patterns in Eurasian FPAR derived from two NDVI-based methods. *International Journal of Digital Earth*, **5**, 283–298.

Piao S, Ciais P, Friedlingstein P, de Noblet-Ducoudré N, Cadule P, Viovy N, Wang T (2009) Spatiotemporal patterns of terrestrial carbon cycle during the 20th century. *Global Biogeochemical Cycles*, **23**, GB4026.

Reeves MC, Zhao M, Running SW (2006) Applying improved estimates of MODIS productivity to characterize grassland vegetation dynamics. *Rangeland Ecology & Management*, **59**, 1–10.

Robinson NP, Allred BW, Jones MO *et al.* (2017) A dynamic Landsat derived normalized difference vegetation index (NDVI) product for the conterminous United States. *Remote Sensing*, **9**, 863.

Ruimy A, Saugier B, Dedieu G (1994) Methodology for the estimation of terrestrial net primary production from remotely sensed data. *Journal of Geophysical Research*, **99**, 5263–5283.

Running SW (2012) Ecology. A measurable planetary boundary for the biosphere. *Science*, **337**, 1458–1459.

Running SW, Zhao M (2015) *MOD17 Users Guide 2015*. Numerical Terra Dynamic Simulation Group.

Running SW, Thornton PE, Nemani R, Glassy JM (2000) Global terrestrial gross and net primary productivity from the earth observing system. In: *Methods in Ecosystem Science (*eds Sala OE *et al.)*, pp. 44–57. Springer New York.

Running SW, Nemani RR, Heinsch FA, Zhao M, Reeves M, Hashimoto H (2004) A continuous satellite-derived measure of global terrestrial primary production. *Bioscience*, **54**, 547–560.

Santaren D, Peylin P, Viovy N, Ciais P (2007) Optimizing a process-based ecosystem model with eddy-covariance flux measurements: A pine forest in southern France. *Global Biogeochemical Cycles*, **21**, GB2013.

Scurlock JMO, Cramer W, Olson RJ, Parton WJ, Prince SD (1999) Terrestrial NPP: Toward a consistent data set for global model evaluation. *Ecological Applications*, **9**, 913–919.

Seiler W, Crutzen PJ (1980) Estimates of gross and net fluxes of carbon between the biosphere and the atmosphere from biomass burning. *Climatic Change*, **2**, 207–247.

Sellers PJ, Tucker CJ, Collatz GJ, Los SO, Justice CO, Dazlich DA, Randall DA (1994) A global 1° by 1° NDVI data set for climate studies. Part 2: The generation of global fields of terrestrial biophysical parameters from the NDVI. *International Journal of Remote Sensing*, **15**, 3519–3545.

Serrano‐Ortiz P, Oyonarte C, Pérez‐Priego O *et al.* (2014) Ecological functioning in grass–shrub Mediterranean ecosystems measured by eddy covariance. *Oecologia*, **175**, 1005–10017.

Sims DA, Rahman AF, Cordova VD *et al.* (2008) A new model of gross primary productivity for North American ecosystems based solely on the enhanced

vegetation index and land surface temperature from MODIS. *Remote Sensing of Environment*, **112**, 1633–1646.

Smith WK, Zhao M, Running SW (2012a) Global bioenergy capacity as constrained by observed biospheric productivity rates. *Bioscience*, **62**, 911–922.

Smith WK, Cleveland CC, Reed SC, Miller NL, Running SW (2012b) Bioenergy potential of the United States constrained by satellite observations of existing productivity. *Environmental Science & Technology*, **46**, 3536–3544.

Smith WK, Reed SC, Cleveland CC *et al.* (2016) Large divergence of satellite and Earth system model estimates of global terrestrial CO2 fertilization. *Nature Climate Change*, **6**, 306–312.

Turner DP, Ritts WD, Cohen WB *et al.* (2003) Scaling Gross Primary Production (GPP) over boreal and deciduous forest landscapes in support of MODIS GPP product validation. *Remote Sensing of Environment*, **88**, 256–270.

Turner DP, Ollinger SV, Kimball JS (2004) Integrating remote sensing and ecosystem process models for landscape- to regional-scale analysis of the carbon cycle. *Bioscience*, **54**, 573–584.

Turner DP, Ritts WD, Cohen WB *et al.* (2005) Site-level evaluation of satellite-based global terrestrial gross primary production and net primary production monitoring. *Global Change Biology*, **11**, 666–684.

Turner DP, Ritts WD, Styles JM, Yang Z, Cohen WB, Law BE, Thornton PE (2006) A diagnostic carbon flux model to monitor the effects of disturbance and interannual variation in climate on regional NEP. *Tellus. Series B, Chemical and Physical Meteorology*, **58**, 476–490.

Turner DP, Ritts WD, Wharton S, Thomas C, Monson R, Black TA, Falk M (2009) Assessing FPAR source and parameter optimization scheme in application of a diagnostic carbon flux model. *Remote Sensing of Environment*, **113**, 1529–1539.

Van Oijen M, Schapendonk A, Höglind M (2010) On the relative magnitudes of photosynthesis, respiration, growth and carbon storage in vegetation. *Annals of Botany*, **105**, 793–797.

Vermote E (2015) MOD09 (006) [Data set]. doi:10.5067/MODIS/MOD09Q1.006

Vermote E, Justice C, Claverie M, Franch B (2016) Preliminary analysis of the performance of the Landsat 8/OLI land surface reflectance product. *Remote Sensing of Environment*, **185**, 46–56.

Vitousek PM, Ehrlich PR, Ehrlich AH, Matson PA (1986) Human appropriation of the products of photosynthesis. *Bioscience*, **36**, 368–373.

Vitousek PM, Mooney HA, Lubchenco J, Melillo JM (1997) Human domination of earth's ecosystems. *Science*, **277**, 494–499.

Wackernagel M, David Yount J (1998) The ecological footprint: an indicator of progress toward regional sustainability. *Environmental Monitoring and Assessment*, **51**, 511–529.

Wackernagel M, Schulz NB, Deumling D *et al.* (2002) Tracking the ecological overshoot of the human economy. *Proceedings of the National Academy of Sciences of the United States of America*, **99**, 9266–9271.

Wang J, Dong J, Liu J *et al.* (2014) Comparison of gross primary productivity derived from GIMMS NDVI3g, GIMMS, and MODIS in Southeast Asia. *Remote Sensing*, **6**, 2108–2133.

Westerling AL, Hidalgo HG, Cayan DR, Swetnam TW (2006) Warming and earlier spring increase western U.S. forest wildfire activity. *Science*, **313**, 940–943.

White PS (1979) Pattern, process, and natural disturbance in vegetation. *The Botanical Review*, **45,** 229–299.

White JD, Ryan KC, Key CC, Running SW (1996) Remote sensing of forest fire severity and vegetation recovery. *International Journal of Wildland Fire*, **6**, 125–136.

Wood JD, Griffis TJ, Baker JM, Frankenberg C, Verma M, Yuen K (2017) Multiscale analyses of solar-induced florescence and gross primary production. *Geophysical Research Letters*, **44**, 533–541.

Yang Y, Zhu Q, Peng C, Wang H, Chen H (2015) From plant functional types to plant functional traits: A new paradigm in modelling global vegetation dynamics. *Progress in Physical Geography*, **39**, 514–535.

Zhang Y, Xu M, Chen H, Adams J (2009) Global pattern of NPP to GPP ratio derived from MODIS data: effects of ecosystem type, geographical location and climate. *Global Ecology and Biogeography*, **18**, 280–290.

Zhao M, Heinsch FA, Nemani RR, Running SW (2005) Improvements of the MODIS terrestrial gross and net primary production global data set. *Remote Sensing of Environment*, **95**, 164–176.

2.7 Tables

Table 2.1: Underlying data sources for the MOD17 (500 m), MODIS derived GPP/NPP_{M250} (CONUS only; 250 m), and Landsat derived GPP/NPP_{L30} (CONUS only; 30 m) products.

		MOD17		MODIS250		LS30	
Input Variable	**Units**	**Source**	**Resolution**	**Source**	**Resolution**	**Source**	**Resolution**
VPD[1]	Pa	GMAO/NASA	0.5°	Idaho Metdata	4 km	Idaho Metdata	4 km
SWrad[2]	w m^{-2}	GMAO/NASA	0.5°	Idaho Metdata	4 km	Idaho Metdata	4 km
Tavg[3]	°C	GMAO/NASA	0.5°	Idaho Metdata	4 km	Idaho Metdata	4 km
Tmin[4]	°C	GMAO/NASA	0.5°	Idaho Metdata	4 km	Idaho Metdata	4 km
Land Cover	na	MOD12Q1	500 m	NLCD	30 m	NLCD	30 m
FPAR[5]	na	MOD15A2	500 m	MOD09Q1	250 m	Landsat SR	30 m
LAI[6]	m^2leaf m^{-2}grd	MOD15A2	500 m	MOD09Q1	250 m	Landsat SR	30 m

[1] vapor pressure deficit, [2] incident shortwave radiation, [3] average daytime temperature, [4] daily minimum temperature, [5] fraction of photosynthetically active radiation, [6] leaf area index

Table 2.2: The biome parameter lookup table (BPLUT) for MOD17, the GPP/NPP_{M250} and the GPP/NPP_{L30}. * Indicates parameters that were modified from the original MOD17 algorithm. ** Indicates parameter added to the BPLUT for LAI calculations.

Dataset	Parameter	ENF[1]	DBF[2]	MF[3]	SH[4]	GR[5]	CR[6]
MOD17	LUE_{max}	0.00096	0.00117	0.00105	0.00128	0.00086	0.00104
	$Tmin_{min}$	-8.00	-6.00	-7.00	-8.00	-8.00	-8.00
	$Tmin_{max}$	8.31	9.94	9.50	8.61	12.02	12.02
	VPD_{min}	650.0	650.0	650.0	650.0	650.0	650.0
	VPD_{max}	4600.0	1650.0	2400.0	4700.0	5300.0	4300.0
GPP /NPP_{M250}	LUE_{max}*	0.00132	0.00156	0.00144	0.00104	0.00142	0.00227
	$Tmin_{min}$*	-9.43	-8.44	-8.94	-7.54	-10.56	-9.48
	$Tmin_{max}$*	7.63	8.59	8.11	10.26	9.45	10.53
	VPD_{min}*	721.51	745.26	733.39	627.08	778.52	723.69
	VPD_{max}*	5703.33	3922.55	4812.94	4206.98	7040.36	5982.23
GPP/ NPP_{LS30}	LUE_{max}*	0.00133	0.00142	0.00138	0.00101	0.00091	0.00176
	$Tmin_{min}$*	-9.44	-8.15	-8.78	-7.94	-11.57	-10.31
	$Tmin_{max}$*	7.63	8.76	8.20	9.97	8.44	9.71
	VPD_{min}*	722.23	733.84	728.04	647.37	828.54	765.33
	VPD_{max}*	5714.47	3650.12	4682.30	4287.20	7697.52	6178.25
All	LAI_{max}**	6.501	6.091	6.296	6.328	6.606	6.543
	SLA	14.1	21.8	21.5	11.5	37.5	30
	Fine Root to Leaf Ratio	1.2	1.1	1.1	1.3	2.6	2
	Base Leaf MR	0.00604	0.00778	0.00778	0.00519	0.0098	0.0098
	Base Fine Root MR	0.00519	0.00519	0.00519	0.00519	0.00819	0.00819
	Q_{10}MR	2	2	2	2	2	2
	Live Wood to Leaf Ratio	0.182	0.203	0.203	0.04	0	0
	Base Livewood MR	0.00397	0.00371	0.00371	0.00218	0	0

[1]Evergreen Needleaf Forest, [2]Deciduous Broadleaf Forest, [3]Mixed Forest, [4]Shrubland, [5]Grassland, [6]Cropland

Table 2.3: QC band pixel value descriptions for GPP/NPP_{M250} and GPP/NPP_{L30}. Differences in the QC values between the two products are due to different input datasets and processing methods. The pixel values indicate the quality of the NDVI values used in calculating FPAR and LAI.

Dataset	Pixel Value	Description
GPP_{M250}	0	Original NDVI value used
	1	Smoothed NDVI value used
NPP_{M250}	0 - 100	Percent of NDVI values gap filled
GPP_{L30}	10	Clear not smoothed
	11	Clear smoothed
	20	Snow or water not smoothed
	21	Snow or water smoothed
	30	Climatology not smoothed
	31	Climatology smoothed
	40	Gap filled not smoothed
	41	Gap filled smoothed
NPP_{L30}	0 - 100	Percentage of gap filled 16-day composites
	255	Incomplete data (gap filling failed)

Table 2.4: Pearson's r-value, RMSE, bias, and mean absolute bias (MAB) between GPP_{M250} and GPP_{L30} and CONUS flux tower GPP aggregated by land cover. Results include GPP calculated with both the original MOD17 algorithm parameters and optimized parameters produced in this paper. The optimized parameters for both datasets yielded better statistics across all land cover classes except shrublands Pearson's r value.

	Tower vs. GPP_{M250}	**Pearson's r**	**RMSE**	**Bias**	**MAB**
All Sites	Optimized Parameters	0.79	2.84	0.02	1.72
	MOD17 Parameters	0.60	4.33	1.90	2.42
ENF	Optimized Parameters	0.85	1.55	0.11	1.15
	MOD17 Parameters	0.84	2.16	1.43	1.59
DBF	Optimized Parameters	0.85	2.56	-0.01	1.75
	MOD17 Parameters	0.55	5.11	3.05	3.35
SH	Optimized Parameters	0.72	0.97	< 0.01	0.62
	MOD17 Parameters	0.74	1.05	-0.46	0.79
GR	Optimized Parameters	0.76	1.72	< 0.01	1.24
	MOD17 Parameters	0.74	2.44	1.38	1.66
CR	Optimized Parameters	0.71	5.13	-0.01	3.61
	MOD17 Parameters	0.64	7.12	3.49	4.23
	Tower vs. GPP_{L30}				
All Sites	Optimized Parameters	0.80	2.91	0.06	1.76
	MOD17 Parameters	0.63	4.25	1.72	2.41
ENF	Optimized Parameters	0.86	1.53	0.10	1.12
	MOD17 Parameters	0.85	2.18	1.44	1.12
DBF	Optimized Parameters	0.88	2.33	0.05	1.62
	MOD17 Parameters	0.57	4.91	2.81	3.19
SH	Optimized Parameters	0.68	1.01	< 0.01	0.64
	MOD17 Parameters	0.71	1.13	-0.45	0.81
GR	Optimized Parameters	0.74	2.09	0.26	1.51
	MOD17 Parameters	0.72	2.41	0.94	1.62
CR	Optimized Parameters	0.70	5.18	< 0.01	3.70
	MOD17 Parameters	0.63	6.74	2.96	4.11

Table 2.5: Pearson's r-value, RMSE, bias and mean absolute bias (MAB) between flux tower GPP and the MOD17 product, GPP_{M250} and GPP_{L30}. These comparisons use 8-day mean GPP, matching the temporal granularity of the MOD17 product. **Bold** indicates the best statistic.

Tower	Dataset	Correlation	RMSE	Bias	MAB
All	MOD17	0.89	1.53	**0.09**	**0.96**
	GPP_{M250}	**0.91**	1.55	-0.48	1.02
	GPP_{L30}	0.90	**1.50**	-0.26	0.99
ENF	MOD17	0.90	1.07	-0.33	0.72
	GPP_{M250}	0.93	1.09	-0.32	0.76
	GPP_{L30}	**0.94**	**0.90**	**-0.19**	**0.62**
DBF	MOD17	0.91	1.98	-0.12	1.28
	GPP_{M250}	**0.95**	**1.62**	-0.55	**1.12**
	GPP_{L30}	0.94	1.70	**-0.09**	1.13
SH	MOD17	0.69	1.04	**0.03**	0.68
	GPP_{M250}	**0.76**	**0.94**	0.04	**0.62**
	GPP_{L30}	0.74	0.97	0.04	0.64
GR	MOD17	0.63	1.30	**0.13**	**0.78**
	GPP_{M250}	**0.69**	**1.23**	-0.27	0.84
	GPP_{L30}	0.66	1.28	-0.25	0.86
CR	MOD17	**0.68**	**1.82**	**0.2**4	**1.25**
	GPP_{M250}	0.66	2.86	-1.84	2.15
	GPP_{L30}	0.65	2.57	-1.53	1.96

Table 2.6: Total annual NPP for CONUS in Pg (10^{15} g) carbon for MOD17, NPP_{M250} and NPP_{L30}. Results are shown aggregated across all land cover as well for each class individually.

LC	Product	2001	2002	2003	2004	2005	2006	2007	2008	2009	2010	2011	2012	2013	2014	Mean
Total	MOD17	2.996	2.946	3.275	3.389	3.217	2.880	3.196	3.162	3.137	3.297	2.880	2.786	3.070	3.120	**3.097**
	NPP_{M250}	4.606	4.192	4.762	5.017	4.712	4.504	4.699	4.631	4.692	4.617	3.864	3.892	4.069	4.566	**4.487**
	NPP_{L30}	3.114	2.834	3.221	3.431	3.194	3.054	3.139	3.208	3.267	3.137	2.519	2.491	2.712	3.148	**3.034**
ENF	MOD17	0.606	0.543	0.609	0.629	0.644	0.573	0.565	0.585	0.595	0.605	0.519	0.508	0.570	0.607	**0.583**
	NPP_{M250}	0.657	0.588	0.635	0.681	0.661	0.639	0.635	0.615	0.645	0.612	0.535	0.561	0.575	0.636	**0.620**
	NPP_{L30}	0.616	0.556	0.598	0.638	0.625	0.602	0.593	0.594	0.613	0.588	0.503	0.525	0.534	0.604	**0.585**
DBF	MOD17	0.602	0.634	0.752	0.710	0.630	0.565	0.578	0.654	0.661	0.651	0.613	0.614	0.683	0.631	**0.641**
	NPP_{M250}	0.923	0.837	0.987	1.000	0.889	0.907	0.886	0.929	0.926	0.861	0.752	0.779	0.799	0.886	**0.883**
	NPP_{L30}	0.701	0.630	0.758	0.772	0.672	0.675	0.637	0.715	0.720	0.649	0.509	0.501	0.573	0.675	**0.656**
MF	MOD17	0.093	0.089	0.096	0.101	0.091	0.087	0.087	0.092	0.091	0.091	0.087	0.087	0.091	0.089	**0.091**
	NPP_{M250}	0.125	0.113	0.123	0.127	0.120	0.120	0.115	0.117	0.118	0.114	0.103	0.111	0.106	0.115	**0.116**
	NPP_{L30}	0.153	0.138	0.152	0.156	0.147	0.146	0.139	0.145	0.146	0.138	0.119	0.129	0.127	0.143	**0.141**
SH	MOD17	0.378	0.366	0.404	0.441	0.456	0.396	0.459	0.407	0.394	0.457	0.380	0.384	0.393	0.414	**0.409**
	NPP_{M250}	0.257	0.235	0.270	0.317	0.317	0.261	0.295	0.263	0.281	0.297	0.234	0.222	0.242	0.279	**0.269**
	NPP_{L30}	0.179	0.162	0.187	0.237	0.224	0.179	0.211	0.186	0.204	0.204	0.149	0.127	0.158	0.191	**0.186**
GR - Natural	MOD17	0.334	0.315	0.358	0.382	0.384	0.325	0.435	0.360	0.361	0.402	0.325	0.292	0.337	0.369	**0.356**
	NPP_{M250}	0.604	0.527	0.621	0.660	0.650	0.561	0.676	0.612	0.635	0.663	0.523	0.502	0.549	0.623	**0.600**
	NPP_{L30}	0.309	0.274	0.317	0.343	0.336	0.295	0.346	0.329	0.344	0.351	0.351	0.266	0.273	0.332	**0.319**
GR - Pasture/ Hay	MOD17	0.379	0.387	0.410	0.414	0.377	0.345	0.393	0.394	0.377	0.401	0.351	0.363	0.373	0.368	**0.381**
	NPP_{M250}	0.552	0.508	0.576	0.591	0.544	0.535	0.542	0.556	0.545	0.535	0.457	0.484	0.482	0.535	**0.532**
	NPP_{L30}	0.232	0.211	0.244	0.251	0.229	0.227	0.227	0.241	0.235	0.224	0.184	0.191	0.196	0.292	**0.227**
CR	MOD17	0.597	0.606	0.638	0.705	0.628	0.583	0.672	0.663	0.650	0.683	0.599	0.532	0.616	0.635	**0.629**
	NPP_{M250}	1.488	1.384	1.550	1.642	1.532	1.480	1.577	1.540	1.543	1.537	1.260	1.235	1.317	1.493	**1.470**
	NPP_{L30}	0.925	0.863	0.965	1.032	0.961	0.930	0.985	0.998	1.103	0.983	0.783	0.751	0.836	0.975	**0.935**

2.8 Figures

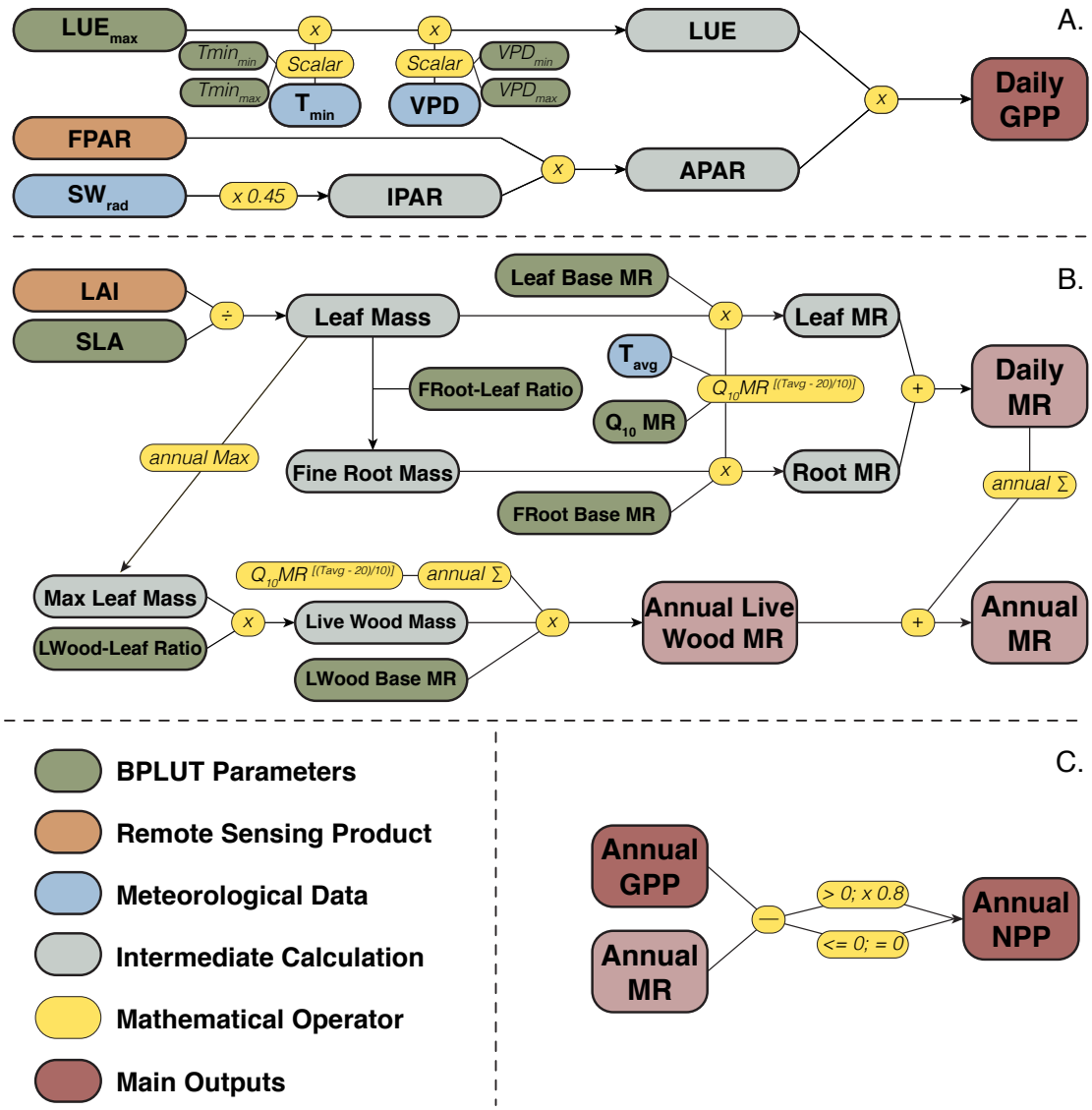

Acronyms: LUE_{max}: maximum light use effecienct; LUE: light use effeciency; T_{min}: minimum daily temperature; VPD: daily vapor pressure deficit; $Tmin_{min}$: minimum daily minimum temperature; $Tmin_{max}$: maximum daily minimum temperature; VPD_{min}: minimum daily vapor pressure deficit; VPD_{max}: maximum daily vapor pressure deficit; SW_{rad}: short wave radiation; FPAR: fraction abosrbed photosynthetically active radiation; IPAR: incident photosynthetically active radiation; APAR: absrobed photosynthetically active radiation; LAI: leaf area index; SLA: specific leaf area; MR: maintenance respiration; FRoot: fine root; LWood: live wood; T_{avg}: average daytime temperature

Figure 2.1: Flowchart of the MOD17 GPP and NPP algorithms. The main components are A) GPP; B) maintenance respiration; and C) annual NPP. Adapted from the MOD17 user's guide (Running & Zhao, 2015).

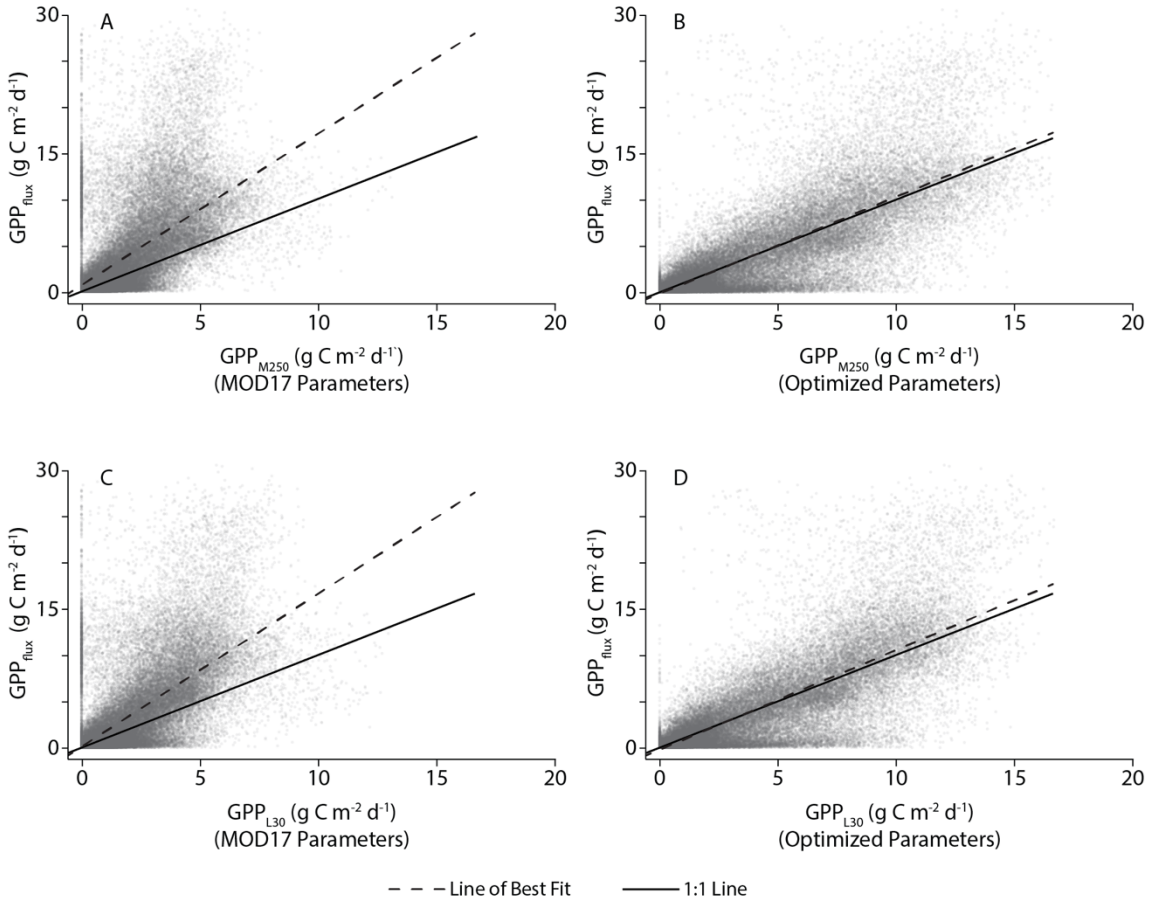

Figure 2.2: GPP_{M250} (A & B) and GPP_{L30} (C & D) relative to GPP_{Flux} (FLUXNET2015, CONUS only). GPP_{250} GPP_{L30} in plots A and C are calculated with the original MOD17 BPLUT parameters, while GPP in B and D use parameters optimized for CONUS and demonstrate improvement.

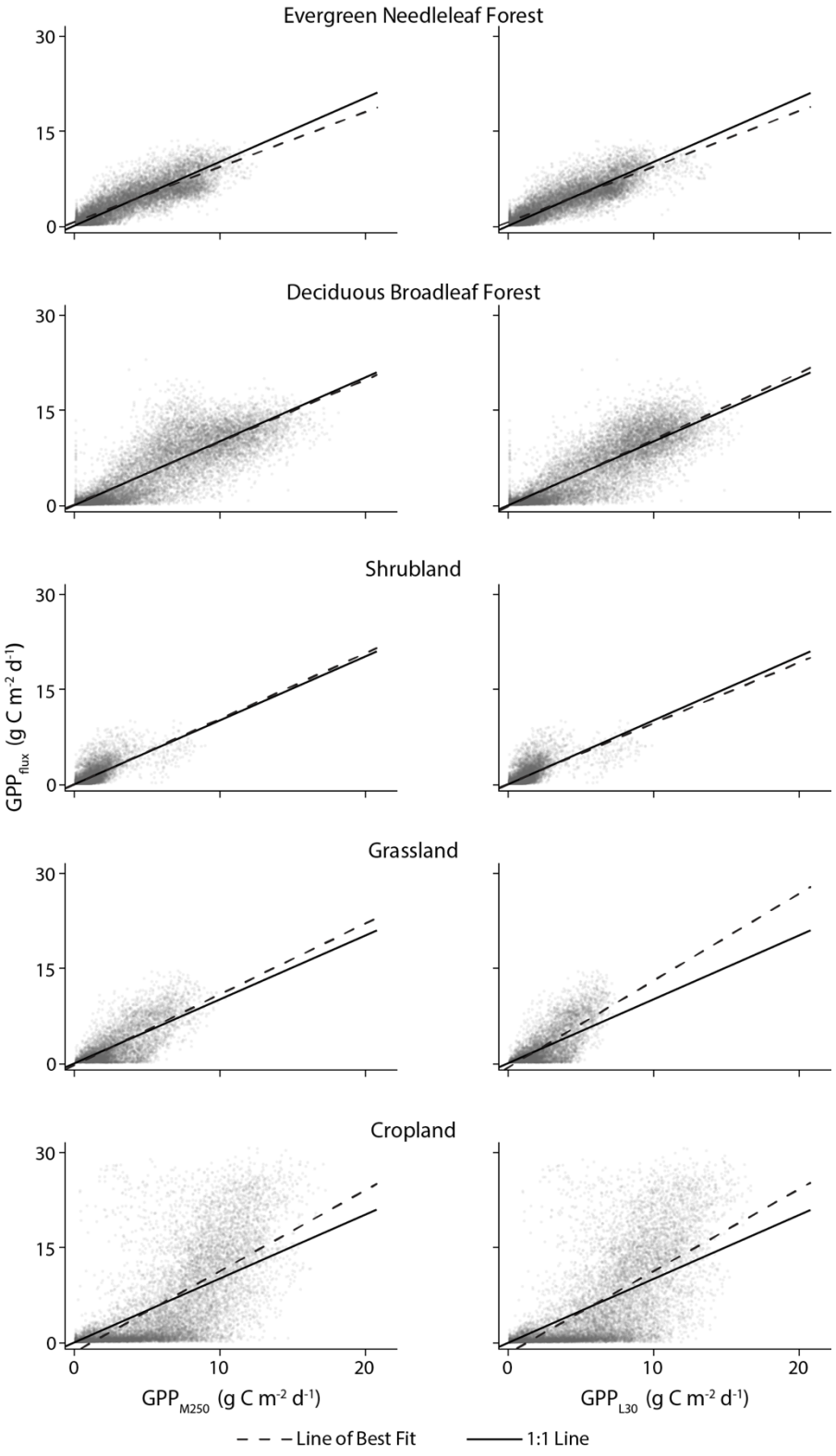

Figure 2.3: GPP_{M250} (left column) and GPP_{L30} (right column) relative to GPP_{Flux} (FLUXNET2015, CONUS only), aggregated by land cover.

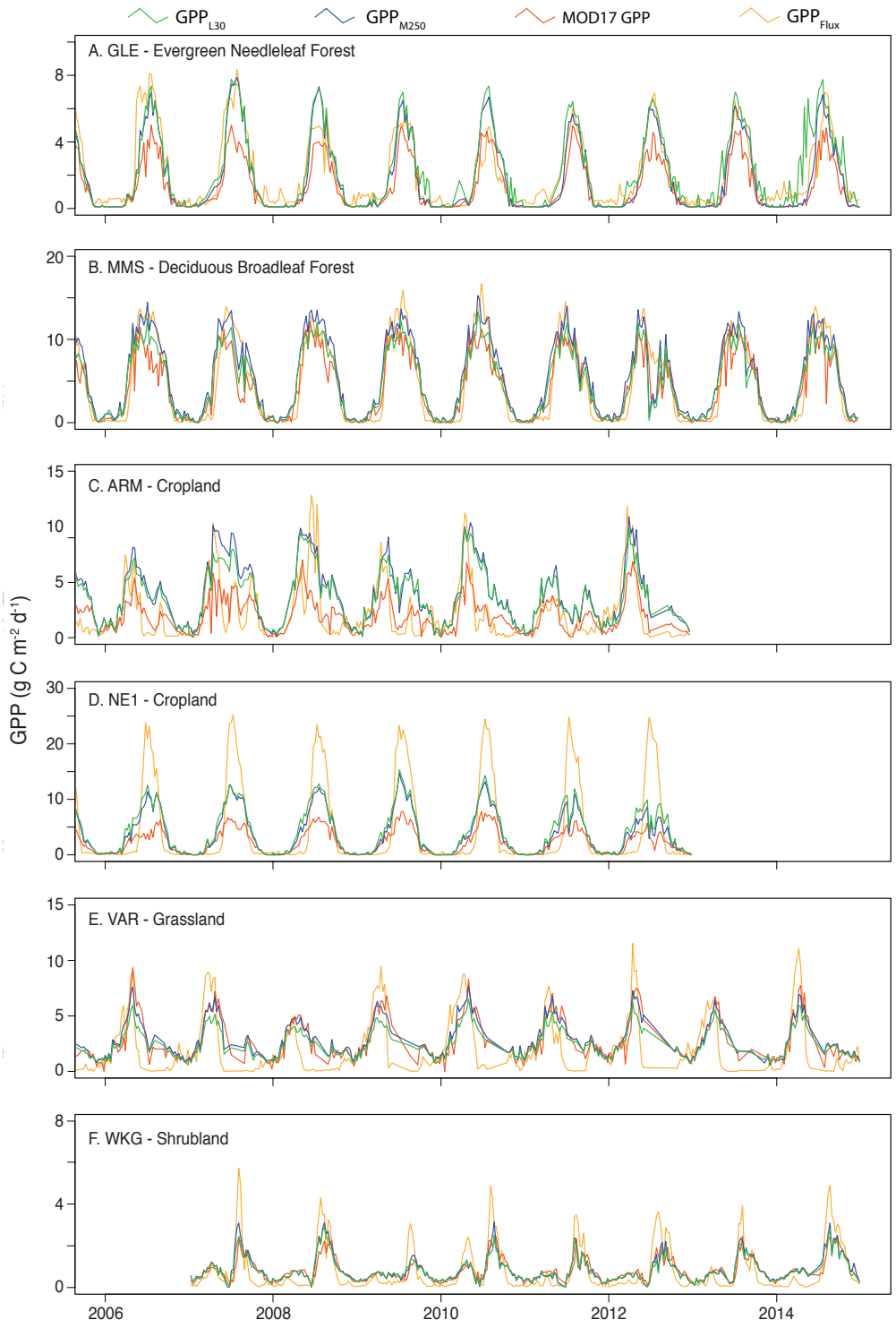

Figure 2.4: Time series of 8-day GPP_{Flux}, MOD17 GPP (500 m), GPP_{M250} (250 m) and GPP_{L30} (30 m) from towers representing the range of land cover classes. Data from two cropland towers (C and D) are plotted demonstrating the range of GPP variability across cropland sites. The GPP_{M250} and GPP_{L30} datasets correspond well with GPP_{Flux} at the ARM flux tower (C; Oklahoma, wheat and soybean) while underestimate GPP compared to GPP_{Flux} at the NE1 flux tower(D; Nebraska, irrigated corn).

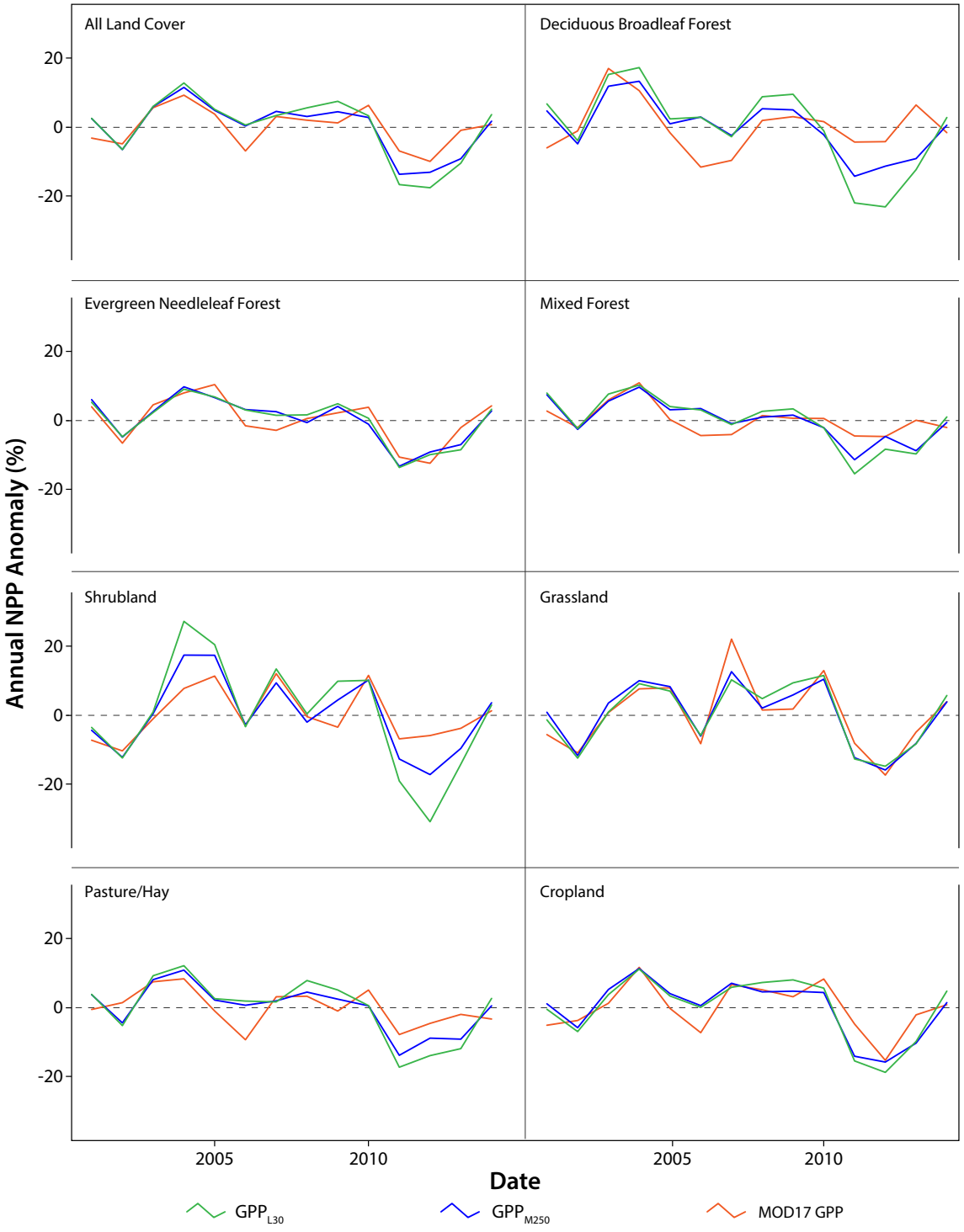

Figure 2.5: Time series of NPP anomalies for the MOD17 (500 m), NPP_{M250} (250 m), and NPP_{L30} (30 m) datasets. All three datasets track the interannual variability of NPP with similar magnitudes. Anomalies are calculated as the percent difference from the long-term mean for each dataset and land cover class.

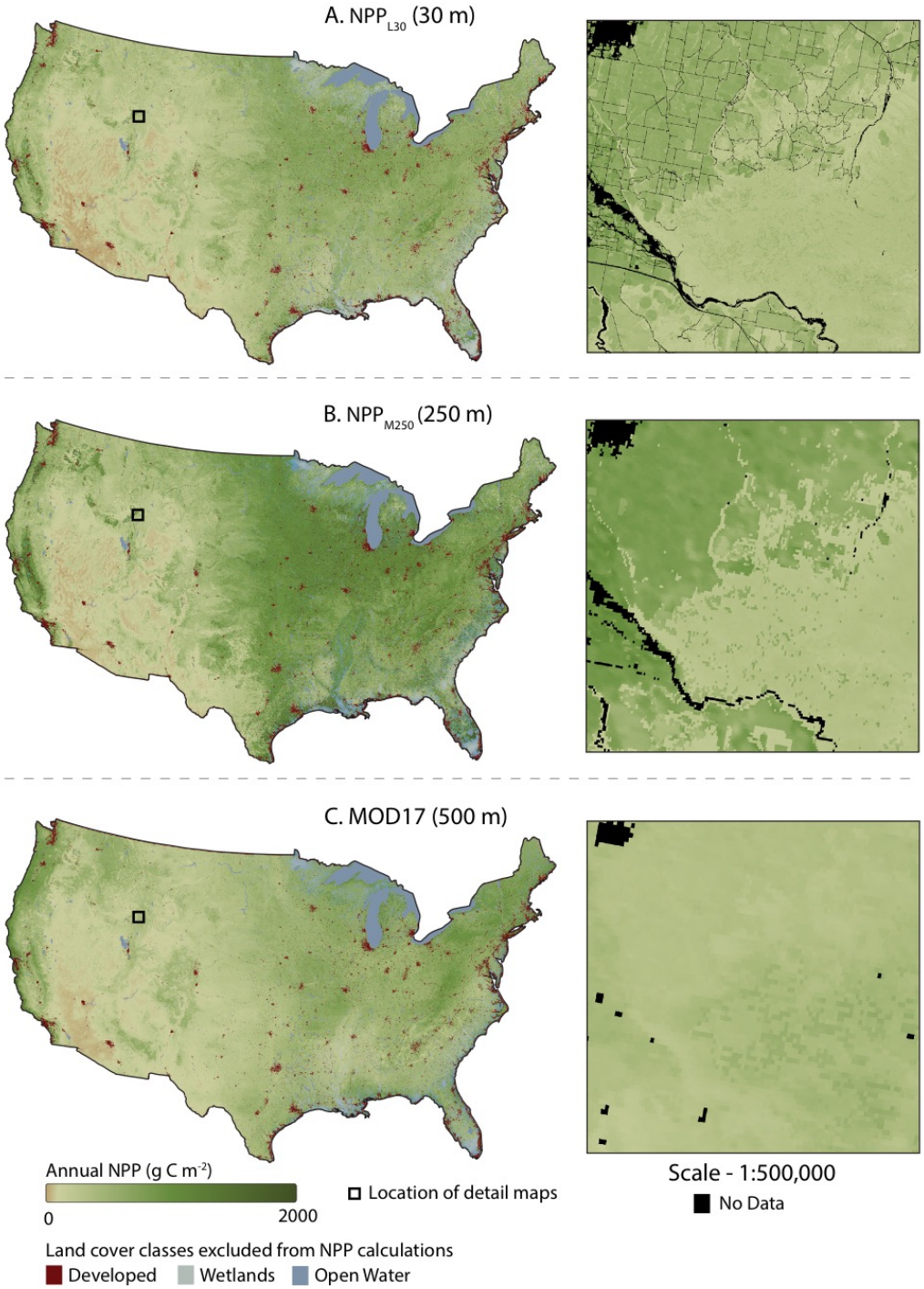

Figure 2.6: Maps of 2010 annual NPP across CONUS at levels of decreasing resolution: (A) NPP_{L30} at 30 m; (B) NPP_{M250} at 250 m; and (C) the MOD17 product at 500 m. Higher resolution reveals greater spatial variability of NPP.

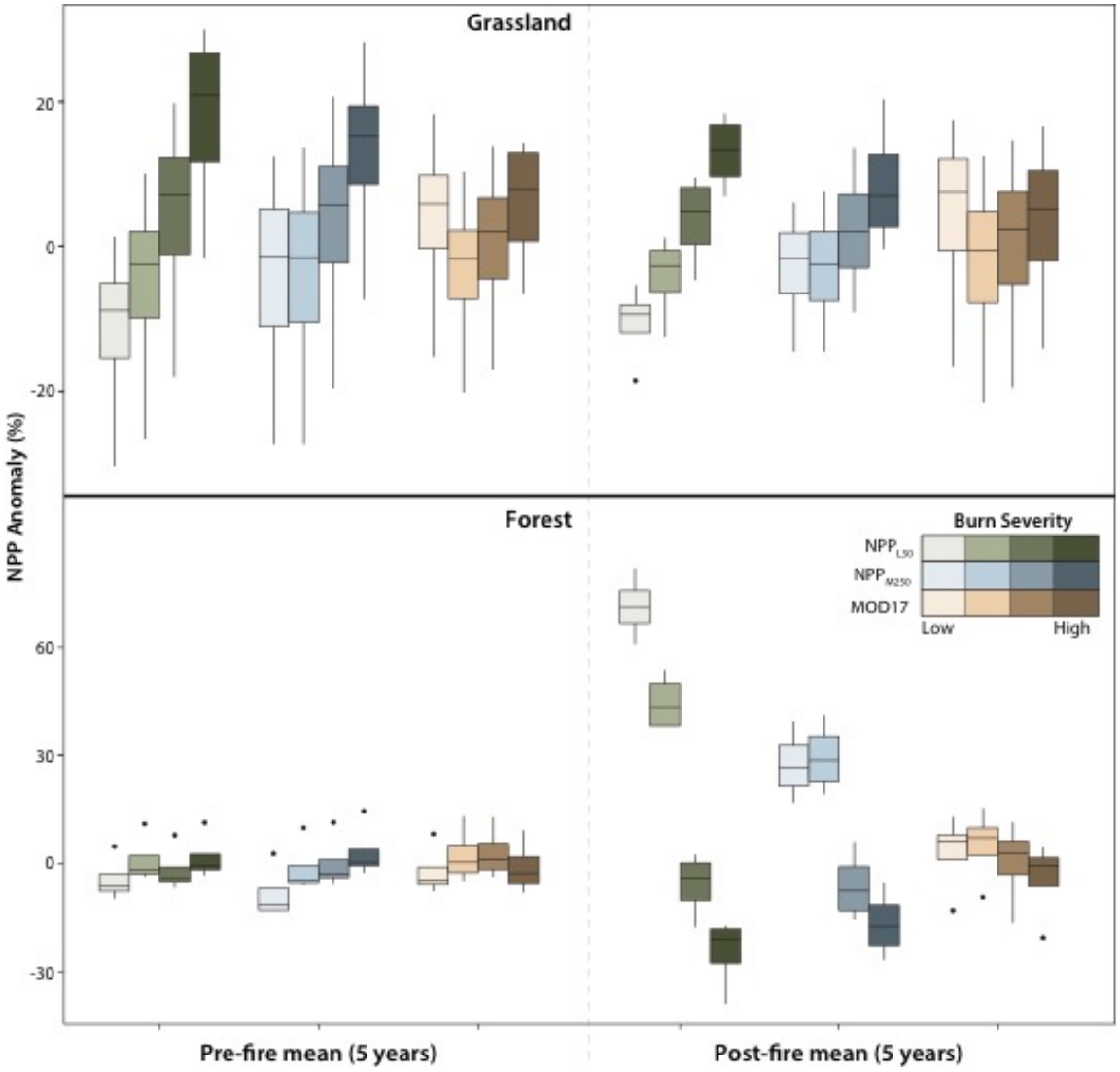

Figure 2.7: Boxplots showing pre- and post-fire NPP dynamics (anomalies) relative to burn severity for a grassland fire (top panels; Lund fire, North Dakota) and an evergreen needleleaf forest fire (bottom panels; Horse Creek fire, Wyoming) using the MOD17 (500 m), NPP_{M250} (250 m), and NPP_{L30} (30 m) products. The nuances of fire-productivity relationships–increased variability between NPP and burn severity, and the resulting responses of NPP to burn severity,– are detected using the medium resolution NPP_{M250} and NPP_{L30} products but are lost with the coarser resolution MOD17 product.

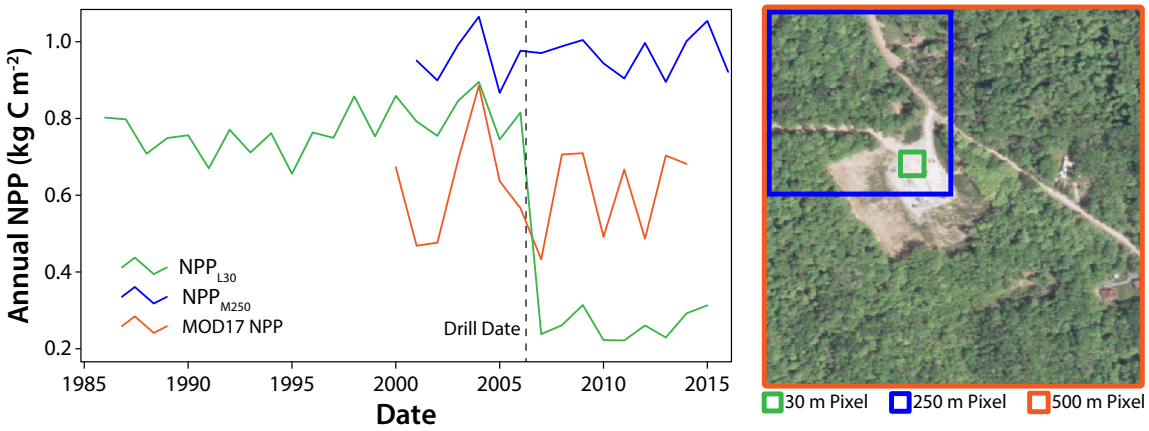

Figure 2.8: Annual NPP for an energy site using the MOD17 product (500 m), NPP_{M250} (250 m), and NPP_{L30} (30 m) datasets. Losses in NPP due the discrete disturbance are reflected in the finer resolution NPP_{L30} dataset , but are absent in the coarser resolution datasets. The time series also demonstrates the historical data available using the full Landsat archive. The relative differences in pixel sizes are shown in the right panel.

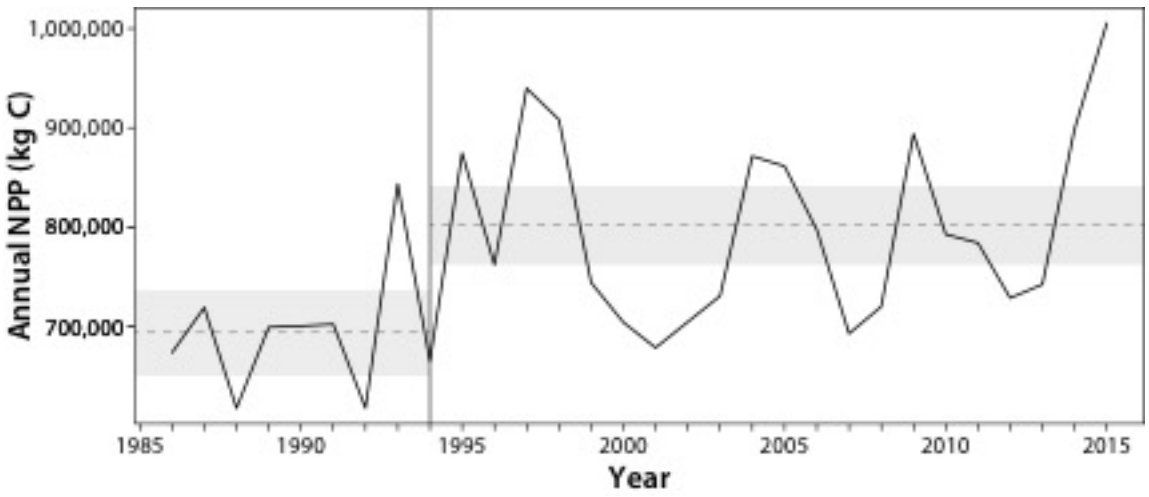

Figure 2.9: The GPP/NPP_{L30} datasets permit the tracking of primary production change across broad spatiotemporal scales. Here, annual NPP for a 60 m buffer around Maggie Creek, Nevada is plotted. Restoration activities occurred in 1994 (vertical black line). The pre- and post-restoration mean NPP (dashed lines) along with 95% confidence intervals are shown.

2.9 Supplemental Materials

Methods

The MOD17 algorithm is built upon four main variables: the absorbed fraction of photosynthetically active radiation (FPAR), leaf area index (LAI), a suite of meteorological measurements, and land cover classification. GPP (Equation 1) combines light use efficiency logic with incident shortwave radiation and FPAR.

$$GPP = LUE_{max} \times f_{Tmin} \times f_{vpd} \times 0.45 \times SW_{rad} \times FPAR \quad (1)$$

LUE_{max} (g C MJ^{-1}) is a biome specific maximum potential light use efficiency and is attenuated by temperature (f_{Tmin}) and vapor pressure deficit (f_{vpd}) scalars to account for temperature and water stress, respectively. SW_{rad} (w m^{-2}) is incoming shortwave radiation, of which 45% is in wavelengths available for photosynthesis. FPAR (unitless) is the estimated fraction of photosynthetically active radiation captured by the plant canopy. NPP is determined by accounting for costs due to maintenance and growth respiration (Equation 2).

$$NPP = \sum_{i=day\ 1}^{365} \left(GPP_i - R_{M_i}\right) - R_G \quad (2)$$

Maintenance respiration (R_M; g C m^{-2} d^{-1}) is calculated using remotely sensed estimates of LAI (m^2 leaf m^{-2} ground), biome specific properties, and meteorological data. The logic is based on allometric relationships between estimated leaf mass, fine root mass, and live wood mass. Plant mass is multiplied by the rate of respiration (Equation 3).

$$Q_{10}MR = Q_{10}^{[\frac{Tavg-20.0}{10.0}]} \quad (3)$$

For live wood and fine roots, Q_{10} is a constant of 2.0, while for leaves it is a temperature acclimated equation (Tjoelker *et al.*, 2001).

$$Q_{10} = 3.22 - 0.046^{Tavg} \quad (4)$$

Growth respiration (R_G) is roughly estimated to be 25% of NPP (Field *et al.*, 1995; Crabtree *et al.*, 2009; Cleveland *et al.*, 2015). A detailed description of the MOD17 algorithm and individual equations is documented in the MOD17 user's guide (Running & Zhao, 2015).

Meteorological Variables

The daily meteorological variables required for the MOD17 algorithm are minimum temperature (T_{min}), average daytime temperature (T_{day}) and vapor pressure deficit (VPD). T_{min} is obtained directly from METDATA while the T_{day} (Running *et al.*, 1987) is calculated from average and maximum temperature estimates (Equation 5). VPD (Equation 6) is simply the difference between the saturation vapor pressure (VP_{sat}) and the actual vapor pressure (VP_{act}). VP_{sat} (Equation 7), is a function of T_{day} (Buck, 1981), while VP_{act} (Equation 8) is a function of specific humidity (SPH) and atmospheric pressure (Equation 9). Atmospheric pressure (P_{atm}) is calculated using the standard

barometric formula and elevation is obtained using the 10 m United States Geological Survey National Elevation Dataset (NED).

$$T_{day} = (0.45 \times (T_{max} - T_{avg})) + T_{avg} \quad (5)$$

$$VPD = VP_{sat} - VP_{act} \quad (6)$$

$$VP_{sat} = 611 \times exp(17.502 \times (\frac{T_{day}}{(T_{day} + 240.97)})) \quad (7)$$

$$VP_{act} = \frac{(SPH \times 1000 \times Pressure)}{621.97} \quad (8)$$

$$P_{atm} = 101325 \times ((1 - (\frac{(0.0065 \times elev)}{288.15}))^{5.25588} \quad (9)$$

The 4 km gridded meteorological data are resampled using bilinear interpolation to a Geographic Coordinate System (GCS) WGS84 grid at the output resolution of the respective datasets.

Land Cover

We utilize the NLCD to apply biome specific parameters (Table 2.S3). The NLCD contains a 21-class land cover for 1992 and a consistent 16-class land cover for 2001, 2006 and 2011. We exclude classes from the classification scheme that are not pertinent to terrestrial productivity (i.e.,. water, developed, barren) and that are not present within CONUS (i.e., dwarf scrub, sedge). The wetland classes, while important to terrestrial production are also excluded, as the presence of water can negatively influence the normalized difference vegetation index (NDVI) which is the source of our FPAR and LAI estimates. Additionally, we combine pasture/hay with the grassland class. The result

is a 6 class land cover classification for CONUS (Table 2.S4) for time periods spanning 1992, 2001, 2006 and 2011. For a given year of GPP and NPP, the closest subsequent NLCD year is used. For example, the 2006 NLCD is used in calculations for 2002 - 2006. From 2007 to 2016, the 2011 dataset is used as the 2016 NLCD is not currently available. For both datasets, the NLCD is resampled, using the mode value, to GCS WGS84 grids at the output resolution of respective datasets.

FPAR and LAI

The MOD17 GPP and NPP products use estimates from another MODIS product, MOD15, as FPAR and LAI inputs. As these estimates are unavailable at finer resolutions, we use established relationships of FPAR and LAI with the normalized difference vegetation index (NDVI) (Choudhury, 1987; Goward & Huemmrich, 1992; Sellers *et al.*, 1994; Paruelo *et al.*, 1997; Gower *et al.*, 1999; Peng *et al.*, 2012; Wang *et al.*, 2014). The NDVI (Equation 10) is one of the most widely implemented spectral indices and is calculated as:

$$NDVI = \frac{(\rho NIR - \rho Red)}{(\rho NIR + \rho Red)} \quad (10)$$

where ρNIR is surface reflectance (SR) in the near infrared band and ρRED is SR in the red band. We first create daily NDVI time series across CONUS for both MODIS and Landsat derived production using the MOD09Q1 and Landsat SR products (Masek *et al.*, 2006; Vermote *et al.*, 2016), respectively. Satellite remotely sensed data are inherently noisy due to atmospheric effects, cloud cover, data retrieval, and processing errors. While

MOD09Q1, an 8-day composite product, accounts for some of these issues, Landsat data are more complex, due to an infrequent overpass interval, collection date differences between adjacent scenes, radiometric differences between missions, and various sensor malfunctions (e.g., Landsat 7 ETM+ scan line corrector error). Thus, for each dataset we employ a separate method for creating the NDVI time series.

MOD09Q1 Processing

MOD09Q1 is an 8-day composite of the Terra/Aqua MODIS red and near-infrared bands (E. Vermote, 2015). Each pixel within each composite constitutes the best available observation during the 8-day window, based on low view angle, high observation coverage, levels of cloud and cloud shadow, and low aerosol loading. Despite this level of processing, MOD09Q1 may still contain cloud or aerosol contamination. Using provided quality control (QC) information, we calculate NDVI for pixels that are flagged as 'clear', resulting in a temporally discontinuous profile in regions of CONUS with a high probability of cloud cover. While QC labels reliably flag pixels with cloud contamination, they do not always specify anomalously low NDVI values. As we generally expect continuous and smooth NDVI temporal profiles, outside of sudden disturbance or land use change (Reed *et al.*, 1994; Bradley *et al.*, 2007; Julien & Sobrino, 2010), we smooth data gaps and unusually low NDVI values based on the iterative Interpolation for Data Reconstruction (IDR) method (Julien & Sobrino, 2010). The NDVI value for each pixel is compared with the mean NDVI value of the first previous and subsequent observations; if the mean is higher than the original value by a threshold of 0.1, the original value is replaced by the mean value. This process is repeated again with

the new temporal profile, resulting in a smooth and continuous 8-day NDVI profile. Estimated daily NDVI values are calculated by linearly interpolating between the 8-day values. The composites are resampled to a GCS WGS84 grid of approximately 250 m (1/450 degrees) resolution.

Landsat SR Processing

The Landsat 5 ETM, 7 ETM+, and 8 OLI SR products are the highest level of processing available for Landsat imagery and are corrected for atmospheric effects and illumination/viewing geometry (Masek *et al.*, 2006; Vermote *et al.*, 2016). We first create 16-day NDVI composites by selecting the best available, cloud free pixels from all available landsat sensors during each composite period (Robinson *et al.*, 2017). If no cloud free pixels are available during a composite window, the gap is filled with the median climatology of the five previous years for that particular 16-day window. If the climatology is unavailable, the gap is filled with a linearly interpolated value between the previous 16-day composite and the subsequent 16-day composite. This interpolation fails when there are two or more composite windows in a row with no data; the pixel is given a no data value and flagged in a QC band. The resulting 16-day NDVI time series is smoothed using iterative IDR, but with only one smoothing iteration due to the large volume of Landsat data. Estimated daily NDVI values are calculated by linearly interpolating between the 16-day composites. The composites are resampled to a GCS WGS84 grid of approximately 30 m (1/5000 degrees) resolution.

FPAR and LAI Calculations

The daily NDVI estimates for both products are used to calculate FPAR (Equation 11) and LAI (Equation 12). FPAR is calculated as:

$$FPAR = \frac{(NDVI - NDVI_{min})(FPAR_{max} - FPAR_{min})}{NDVI_{max} - NDVI_{min}} + FPAR_{min} \quad (11)$$

where $NDVI_{min}$ = 0.03, $NDVI_{max}$ = 0.96, calculated as the 2% and 98% of the NDVI frequency distribution and $FPAR_{min}$ = 0.001, $FPAR_{max}$ = 0.95, corresponding to the theoretical minimum and maximum FPAR for any vegetated surface (Wang *et al.*, 2014). The relationship between NDVI and LAI is more complex, as NDVI can effectively saturate while LAI continues to increase, leading to potential underestimation of LAI. LAI is calculated as:

$$LAI = \frac{log(1 - FPAR)}{log(1 - FPAR_{max})} \times LAI_{max_i} \quad (12)$$

where $FPAR_{max}$ is 0.95 and $LAI_{max,i}$ is the potential maximum LAI for each land cover class from the BPLUT (Sellers *et al.*, 1994).

Parameter Optimization

We use tier one level data from the FLUXNET2015 dataset, containing data from 43 tower sites across CONUS and representing the range of land cover classes (Figure 2.S2; Table 2.S1). To avoid the inclusion of poor quality data, we only use flux towers with at least two years of data and select daily GPP observations flagged as high quality (quality flag >= 0.75) (Richardson *et al.*, 2010; Verma *et al.*, 2015). At some flux tower sites

there is a discrepancy in land cover as designated by the flux tower dataset and the dominant land cover as classified by the NLCD. To avoid flux towers in areas with heterogeneous land cover, towers are only included if more than 50% of the pixels within a one km buffer are classified as the dominant land cover based on the NLCD and match the given land cover classification of the flux tower. At each flux tower location we extract the spatial mean of daily meteorological input variables (T_{min}, VPD and SW_{rad}) within a one km buffer of each tower location. The daily FPAR estimates for each product are extracted in the same way, however only pixels representing the dominant land cover (based on the categorization of the NLCD) within the buffer are included (Figure 2.S3). Our optimization approach finds the parameter set (Table 2.2) that minimizes the residual sum of squares between model outputs and the corresponding flux tower GPP estimates for each land cover class (Turner *et al.*, 2006, 2009). We utilize a limited memory, quasi-Newton algorithm (L-BFGS-B) for optimization (Byrd *et al.*, 1995; Santaren *et al.*, 2007), using original MOD17 algorithm parameters as starting values for initialization.

Supplemental References

Bradley BA, Jacob RW, Hermance JF, Mustard JF (2007) A curve fitting procedure to derive inter-annual phenologies from time series of noisy satellite NDVI data. *Remote Sensing of Environment*, **106**, 137–145.

Buck AL (1981) New equations for computing vapor pressure and enhancement factor. *Journal of Applied Meteorology*, **20**, 1527–1532.

Byrd RH, Lu P, Nocedal J, Zhu C (1995) A limited memory algorithm for bound constrained optimization. *SIAM Journal on Scientific Computing*, **16**, 1190–1208.

Choudhury BJ (1987) Relationships between vegetation indices, radiation absorption, and net photosynthesis evaluated by a sensitivity analysis. *Remote Sensing of Environment*, **22**, 209–233.

Cleveland CC, Taylor P, Chadwick KD *et al.* (2015) A comparison of plot-based satellite and Earth system model estimates of tropical forest net primary production. *Global Biogeochemical Cycles*, **29**, 626–644.

Crabtree R, Potter C, Mullen R *et al.* (2009) A modeling and spatio-temporal analysis framework for monitoring environmental change using NPP as an ecosystem indicator. *Remote Sensing of Environment*, **113**, 1486–1496.

Field CB, Randerson JT, Malmström CM (1995) Global net primary production: Combining ecology and remote sensing. *Remote Sensing of Environment*, **51**, 74–88.

Goward SN, Huemmrich KF (1992) Vegetation canopy PAR absorbance and the normalized difference vegetation index: An assessment using the SAIL model. *Remote Sensing of Environment*, **39**, 119–140.

Gower ST, Kucharik CJ, Norman JM (1999) Direct and indirect estimation of leaf area

index, f APAR, and net primary production of terrestrial ecosystems. *Remote Sensing of Environment*, **70**, 29–51.

Julien Y, Sobrino JA (2010) Comparison of cloud-reconstruction methods for time series of composite NDVI data. *Remote Sensing of Environment*, **114**, 618–625.

Masek JG, Vermote EF, Saleous NE *et al.* (2006) A Landsat surface reflectance dataset for North America, 1990-2000. *IEEE Geoscience and Remote Sensing Letters*, **3**, 68–72.

Paruelo JM, Epstein HE, Lauenroth WK, Burke IC (1997) ANPP estimates from NDVI for the central grassland region of the United States. *Ecology*, **78**, 953–958.

Peng D, Zhang B, Liu L (2012) Comparing spatiotemporal patterns in Eurasian FPAR derived from two NDVI-based methods. *International Journal of Digital Earth*, **5**, 283–298.

Reed BC, Brown JF, VanderZee D, Loveland TR, Merchant JW, Ohlen DO (1994) Measuring phenological variability from satellite imagery. *Journal of Vegetation Science*, **5**, 703–714.

Richardson AD, Black TA, Ciais P *et al.* (2010) Influence of spring and autumn phenological transitions on forest ecosystem productivity. *Philosophical Transactions of the Royal Society of London.*, **365**, 3227–3246.

Robinson NP, Allred BW, Jones MO *et al.* (2017) A Dynamic Landsat Derived Normalized Difference Vegetation Index (NDVI) Product for the Conterminous United States. *Remote Sensing*, **9**, 863.

Running SW, Zhao M (2015) *MOD17 Users Guide 2015*. Numerical Terradynamic Simulation Group.

Running SW, Nemani RR, Hungerford RD (1987) Extrapolation of synoptic meteorological data in mountainous terrain and its use for simulating forest evapotranspiration and photosynthesis. *Canadian journal of forest research*, **17**, 472–483.

Santaren D, Peylin P, Viovy N, Ciais P (2007) Optimizing a process-based ecosystem model with eddy-covariance flux measurements: A pine forest in southern France. *Global Biogeochemical Cycles*, **21**, GB2013.

Sellers PJ, Tucker CJ, Collatz GJ, Los SO, Justice CO, Dazlich DA, Randall DA (1994) A global 1° by 1° NDVI data set for climate studies. Part 2: The generation of global fields of terrestrial biophysical parameters from the NDVI. *International Journal of Remote Sensing*, **15**, 3519–3545.

Tjoelker MG, Oleksyn J, Reich PB (2001) Modelling respiration of vegetation: evidence for a general temperature-dependent Q10. *Global Change Biology*, **7**, 223–230.

Turner DP, Ritts WD, Styles JM, Yang Z, Cohen WB, Law BE, Thornton PE (2006) A diagnostic carbon flux model to monitor the effects of disturbance and interannual variation in climate on regional NEP. *Tellus. Series B, Chemical and Physical Meteorology*, **58**, 476–490.

Turner DP, Ritts WD, Wharton S, Thomas C, Monson R, Black TA, Falk M (2009) Assessing FPAR source and parameter optimization scheme in application of a diagnostic carbon flux model. *Remote Sensing of Environment*, **113**, 1529–1539.

Verma M, Friedl MA, Law BE *et al.* (2015) Improving the performance of remote sensing models for capturing intra- and inter-annual variations in daily GPP: An analysis using global FLUXNET tower data. *Agricultural and Forest Meteorology*,

214–215, 416–429.

Vermote E (2015) MOD09 (006) [Data set]. doi:10.5067/MODIS/MOD09Q1.006

Vermote E, Justice C, Claverie M, Franch B (2016) Preliminary analysis of the performance of the Landsat 8/OLI land surface reflectance product. *Remote Sensing of Environment*, **185**, 46–56.

Wang J, Dong J, Liu J *et al.* (2014) Comparison of gross primary productivity derived from GIMMS NDVI3g, GIMMS, and MODIS in Southeast Asia. *Remote Sensing*, **6**, 2108–2133.

Table 2.S1: Flux Tower Info

	Site ID	Dates	State	Lat (°N)	Long (°E)	NLCD LC	DOI
1	US-AR1	2009-2012	Oklahoma	36.4267	-99.42	GR	http://dx.doi.org/10.17190/AMF/1246137
2	US_AR2	2009-2012	Oklahoma	36.6358	-99.5975	GR	http://dx.doi.org/10.17190/AMF/1246138
3	US-ARb	2005-2006	Oklahoma	35.5497	-98.0402	GR	http://dx.doi.org/10.17190/AMF/1246025
4	US-ARc	2005-2006	Oklahoma	35.5465	-98.04	GR	http://dx.doi.org/10.17190/AMF/1246026
5	US-ARM	2003-2012	Oklahoma	36.6058	-97.4888	CR	http://dx.doi.org/10.17190/AMF/1246027
6	US-Blo	1997-2007	California	38.8953	-120.6328	ENF	http://dx.doi.org/10.17190/AMF/1246032
7	US-Cop	2001-2007	Utah	38.09	-109.39	SH	http://dx.doi.org/10.17190/AMF/1246129
8	US-GLE	2004-2014	Wyoming	41.3665	-106.2399	ENF	http://dx.doi.org/10.17190/AMF/1246056
9	US-Ha1	1991-2012	Massachusetts	42.5378	-72.1715	DBF	http://dx.doi.org/10.17190/AMF/1246059
10	US-Me2	2002-2014	Oregon	44.4523	-121.5574	ENF	http://dx.doi.org/10.17190/AMF/1246076
11	US-Me6	2010-2014	Oregon	44.3233	-121.6078	ENF	http://dx.doi.org/10.17190/AMF/1246128
12	US-MMS	1999-2014	Indiana	39.3232	-86.4131	DBF	http://dx.doi.org/10.17190/AMF/1246080
13	US-Ne1	2001-2013	Nebraska	41.1651	-96.4766	CR	http://dx.doi.org/10.17190/AMF/1246084
14	US-Ne2	2001-2013	Nebraska	41.1649	-96.4701	CR	http://dx.doi.org/10.17190/AMF/1246085
15	US-Ne3	2001-2013	Nebraska	41.1797	-96.4397	CR	http://dx.doi.org/10.17190/AMF/1246086
16	US-NR1	1998-2014	Colorado	40.0329	-105.5464	ENF	http://dx.doi.org/10.17190/AMF/1246088
17	US-SRG	2008-2014	Arizona	31.7894	-110.8277	SH	http://dx.doi.org/10.17190/AMF/1246154
18	US-SRM	2004-2014	Arizona	31.8214	-110.8661	SH	http://dx.doi.org/10.17190/AMF/1246104
19	US-Ton	2001-2014	California	38.4316	-120.966	GR	http://dx.doi.org/10.17190/AMF/1245971
20	US-Tw3	2013-2014	California	38.1159	-121.6467	CR	http://dx.doi.org/10.17190/AMF/1246149
21	US-Twt	2009-2014	California	38.1087	-121.653	CR	http://dx.doi.org/10.17190/AMF/1246140
22	US-UMB	2000-2014	Michigan	45.5598	-84.7138	DBF	http://dx.doi.org/10.17190/AMF/1246107
23	US-UMd	2007-2014	Michigan	45.5625	-84.6975	DBF	http://dx.doi.org/10.17190/AMF/1246134
24	US-Var	2000-2014	California	38.4133	-120.9507	GR	http://dx.doi.org/10.17190/AMF/1245984
25	US-WCr	1999-2014	Wisconsin	45.8059	-90.0799	DBF	http://dx.doi.org/10.17190/AMF/1246111
26	US-Whs	2007-2014	Arizona	31.7438	-110.0522	SH	http://dx.doi.org/10.17190/AMF/1246113
27	US-Wi3	2002-2004	Wisconsin	46.6347	-91.0987	DBF	http://dx.doi.org/10.17190/AMF/1246018
28	US-Wi4	2002-2005	Wisconsin	46.7393	-91.1663	ENF	http://dx.doi.org/10.17190/AMF/1246019
29	US-Wi9	2004-2005	Wisconsin	46.6188	-91.0814	SH	http://dx.doi.org/10.17190/AMF/1246024
30	US-Wkg	2004-2014	Arizona	31.7365	-109.9419	SH	http://dx.doi.org/10.17190/AMF/1246112

Table 2.S2: Total annual NPP for CONUS in Pg (10^{15} g) carbon for MOD17, NPP_{M250} and NPP_{L30} calculated with respiration as a fixed ratio of GPP and with the MOD17 procedure. Results are shown aggregated across all land cover as well for each class individually.

LC	Product	2001	2002	2003	2004	2005	2006	2007	2008	2009	2010	2011	2012	2013	2014	Mean
Total	MOD17	2.996	2.946	3.275	3.389	3.217	2.880	3.196	3.162	3.137	3.297	2.880	2.786	3.070	3.120	**3.097**
	NPP_{M250}	4.606	4.192	4.762	5.017	4.712	4.504	4.699	4.631	4.692	4.617	3.864	3.892	4.069	4.566	**4.487**
	NPP_{M250} (fixed ratio)	4.084	3.813	4.161	4.334	4.192	3.979	4.194	4.017	4.022	4.115	3.590	3.649	3.731	3.983	**3.990**
	NPP_{L30}	3.114	2.834	3.221	3.431	3.194	3.054	3.139	3.208	3.267	3.137	2.519	2.491	2.712	3.148	**3.034**
	NPP_{L30} (fixed ratio)	3.281	3.091	3.319	3.472	3.393	3.254	3.356	3.307	3.350	3.380	2.976	3.070	3.158	3.378	**3.270**
ENF	MOD17	0.606	0.543	0.609	0.629	0.644	0.573	0.565	0.585	0.595	0.605	0.519	0.508	0.570	0.607	**0.583**
	NPP_{M250}	0.657	0.588	0.635	0.681	0.661	0.639	0.635	0.615	0.645	0.612	0.535	0.561	0.575	0.636	**0.620**
	NPP_{M250} (fixed ratio)	0.666	0.615	0.650	0.675	0.659	0.640	0.639	0.611	0.625	0.614	0.559	0.593	0.590	0.624	**0.626**
	NPP_{L30}	0.616	0.556	0.598	0.638	0.625	0.602	0.593	0.594	0.613	0.588	0.503	0.525	0.534	0.604	**0.585**
	NPP_{L30} (fixed ratio)	0.677	0.633	0.659	0.683	0.680	0.666	0.653	0.640	0.655	0.648	0.599	0.636	0.636	0.674	**0.653**
DBF	MOD17	0.602	0.634	0.752	0.710	0.630	0.565	0.578	0.654	0.661	0.651	0.613	0.614	0.683	0.631	**0.641**
	NPP_{M250}	0.923	0.837	0.987	1.000	0.889	0.907	0.886	0.929	0.926	0.861	0.752	0.779	0.799	0.886	**0.883**
	NPP_{M250} (fixed ratio)	0.791	0.750	0.817	0.831	0.781	0.776	0.762	0.775	0.762	0.762	0.690	0.708	0.707	0.743	**0.761**
	NPP_{L30}	0.701	0.630	0.758	0.772	0.672	0.675	0.637	0.715	0.720	0.649	0.509	0.501	0.573	0.675	**0.656**
	NPP_{L30} (fixed ratio)	0.691	0.653	0.713	0.730	0.685	0.677	0.660	0.688	0.689	0.673	0.591	0.606	0.639	0.682	**0.670**
MF	MOD17	0.093	0.089	0.096	0.101	0.091	0.087	0.087	0.092	0.091	0.091	0.087	0.087	0.091	0.089	**0.091**
	NPP_{M250}	0.125	0.113	0.123	0.127	0.120	0.120	0.115	0.117	0.118	0.114	0.103	0.111	0.106	0.115	**0.116**
	NPP_{M250} (fixed ratio)	0.146	0.136	0.144	0.147	0.142	0.140	0.135	0.135	0.134	0.134	0.124	0.132	0.127	0.132	**0.136**
	NPP_{L30}	0.153	0.138	0.152	0.156	0.147	0.146	0.139	0.145	0.146	0.138	0.119	0.129	0.127	0.143	**0.141**
	NPP_{L30} (fixed ratio)	0.147	0.137	0.144	0.147	0.144	0.142	0.136	0.137	0.138	0.137	0.126	0.136	0.133	0.140	**0.139**
SH	MOD17	0.378	0.366	0.404	0.441	0.456	0.396	0.459	0.407	0.394	0.457	0.380	0.384	0.393	0.414	**0.409**
	NPP_{M250}	0.257	0.235	0.270	0.317	0.317	0.261	0.295	0.263	0.281	0.297	0.234	0.222	0.242	0.279	**0.269**
	NPP_{M250} (fixed ratio)	0.376	0.357	0.397	0.435	0.440	0.381	0.436	0.390	0.395	0.425	0.344	0.358	0.368	0.402	**0.393**
	NPP_{L30}	0.179	0.162	0.187	0.237	0.224	0.179	0.211	0.186	0.204	0.204	0.149	0.127	0.158	0.191	**0.186**
	NPP_{L30} (fixed ratio)	0.294	0.282	0.309	0.344	0.352	0.308	0.345	0.320	0.329	0.350	0.282	0.293	0.304	0.334	**0.318**
GR - Natural	MOD17	0.334	0.315	0.358	0.382	0.384	0.325	0.435	0.360	0.361	0.402	0.325	0.292	0.337	0.369	**0.356**
	NPP_{M250}	0.604	0.527	0.621	0.660	0.650	0.561	0.676	0.612	0.635	0.663	0.523	0.502	0.549	0.623	**0.600**
	NPP_{M250} (fixed ratio)	0.522	0.465	0.535	0.561	0.561	0.489	0.586	0.525	0.538	0.572	0.471	0.455	0.493	0.538	**0.522**
	NPP_{L30}	0.309	0.274	0.317	0.343	0.336	0.295	0.346	0.329	0.344	0.351	0.351	0.266	0.273	0.332	**0.319**
	NPP_{L30} (fixed ratio)	0.325	0.298	0.330	0.349	0.353	0.314	0.366	0.342	0.352	0.371	0.314	0.317	0.331	0.356	**0.337**
GR - Pasture/ Hay	MOD17	0.379	0.387	0.410	0.414	0.377	0.345	0.393	0.394	0.377	0.401	0.351	0.363	0.373	0.368	**0.381**
	NPP_{M250}	0.552	0.508	0.576	0.591	0.544	0.535	0.542	0.556	0.545	0.535	0.457	0.484	0.482	0.535	**0.532**
	NPP_{M250} (fixed ratio)	0.461	0.433	0.472	0.485	0.455	0.443	0.456	0.451	0.443	0.452	0.402	0.421	0.417	0.437	**0.445**
	NPP_{L30}	0.232	0.211	0.244	0.251	0.229	0.227	0.227	0.241	0.235	0.224	0.184	0.191	0.196	0.292	**0.227**
	NPP_{L30} (fixed ratio)	0.288	0.273	0.291	0.300	0.287	0.281	0.288	0.288	0.284	0.290	0.264	0.281	0.277	0.290	**0.284**
CR	MOD17	0.597	0.606	0.638	0.705	0.628	0.583	0.672	0.663	0.650	0.683	0.599	0.532	0.616	0.635	**0.629**
	NPP_{M250}	1.488	1.384	1.550	1.642	1.532	1.480	1.577	1.540	1.543	1.537	1.260	1.235	1.317	1.493	**1.470**
	NPP_{M250} (fixed ratio)	1.123	1.056	1.146	1.200	1.153	1.111	1.180	1.130	1.126	1.156	1.001	0.983	1.029	1.107	**1.107**
	NPP_{L30}	0.925	0.863	0.965	1.032	0.961	0.930	0.985	0.998	1.103	0.983	0.783	0.751	0.836	0.975	**0.935**
	NPP_{L30} (fixed ratio)	0.859	0.815	0.874	0.919	0.892	0.866	0.908	0.893	0.903	0.911	0.800	0.802	0.839	0.903	**0.870**

Table 2.S3: Biome specific properties used in the MOD17 algorithm (Running & Zhao, 2015).

Component	Pameter	Units	Description
GPP	LUE_{max}	kg C MJ^{-1}	Maximum light use efficiency
	$Tmin_{max}$	°C	Daily minimum temperature at which LUE = LUE_{max} (for optimal VPD)
	$Tmin_{min}$	°C	Daily minimum temperature at which LUE = 0 (for any VPD)
	VPD_{max}	Pa	Daylight average VPD at which LUE = LUEmax (for optimal Tmin)
	VPD_{min}	Pa	Daylight average VPD at which LUE = 0.0 (for any Tmin)
Daily MR	LAI_{max}	m^2leaf m^2ground	Potential maximum LAI
	SLA	m^2kg C^{-1}	Leaf area per unit mass of leaf carbon
	Fine Root-Leaf Ratio	na	Fine root carbon to leaf carbon ratio
	Base Leaf MR	kg C kg $C^{-1}day^{-1}$	Maintenance respiration per unit leaf carbon per day at 20 °C
	Base Fine Root MR	kg C kg $C^{-1}day^{-1}$	Maintenance respiration per unit fine root carbon per day at 20 °C
	Q_{10}MR	na	Exponent shape parameter controlling respiration as a function of temp
Annual MR	Live Wood-Leaf Ratio	na	Live wood carbon to annual maximum leaf carbon ratio
	Base Livewood MR	kg C kg $C^{-1}day^{-1}$	Maintenance respiration per unit live wood carbon per day at 20 °C
	Q_{10}MR	na	Exponent shape parameter controlling respiration as a function of temp

Table 2.S4: Reclassification scheme for National Land Cover Database (NLCD). Grassland and pasture/hay are combined as grassland.

Class	Reclassified Value	NLCD Values	NLCD Classes
Evergreen Needleleaf Forest (ENF)	1	42	Evergreen Forest
Deciduous Broadleaf Forest (DBF)	2	41	Deciduous Forest
Mixed Forest (MF)	3	43	Mixed Forest
Shrublands (SH)	4	52, *51	Shrub/Scrub, *Shrubland
Grasslands (GR)	5	71, 81	Grassland, Pasture/hay
Croplands (CR)	6	82, *83	Crops, *Small grains

*** Indicates unique class in NLCD 1992**

Figure 2.S1: Illustration of the linear ramp functions for scaling minimum temperature and vapor pressure deficit.

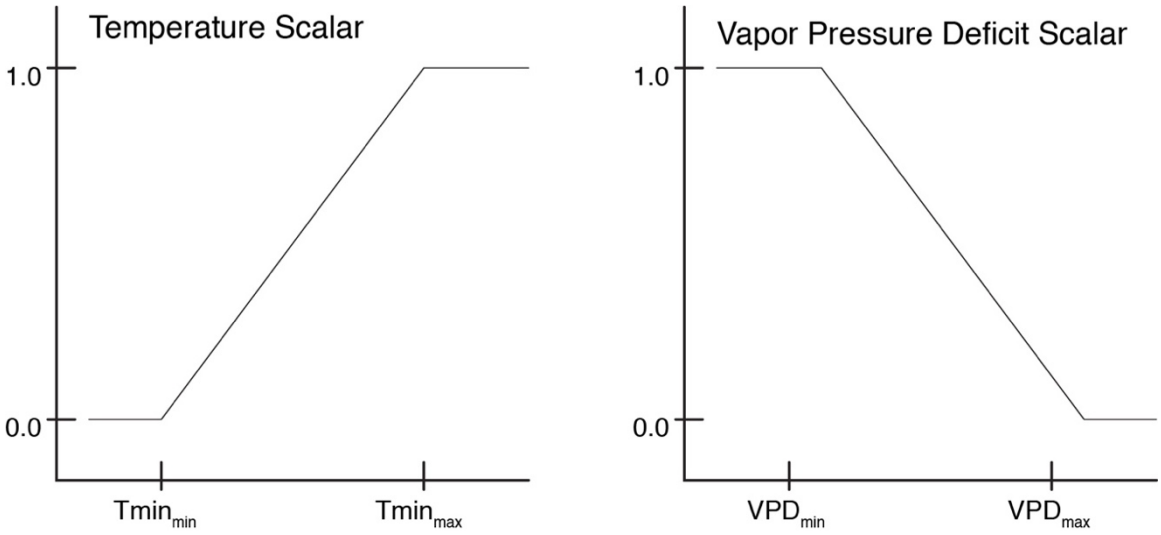

Figure 2.S2: Map of individual flux tower sites used for the GPP parameter optimization. The numbers correspond with individual flux towers described in Table 2.S1.

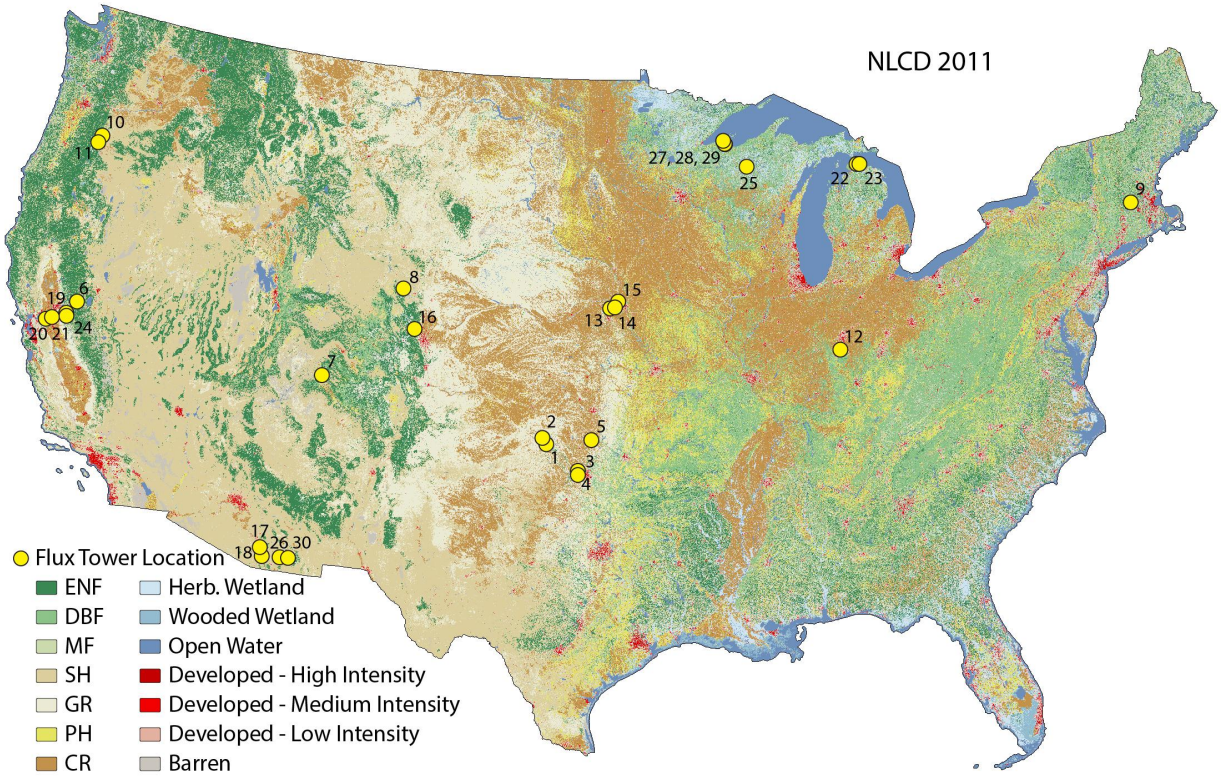

Figure 2.S3: (A) The NLCD within a 1 km buffer of the Wi4 flux tower located in Northern Wisconsin, demonstrating heterogeneous land cover cover at 30 m resolution. (B) Only FPAR values from pixels of the dominant land cover (evergreen needleleaf forest for this tower) are used in the parameter optimization process.

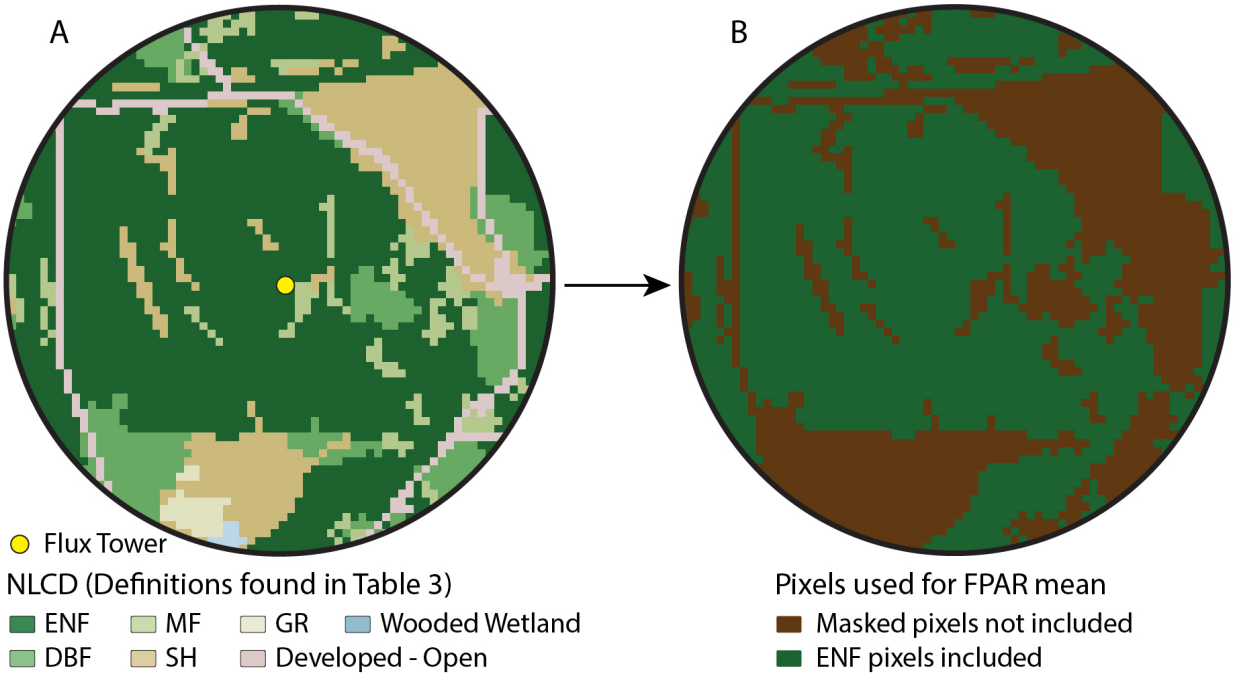

Figure 2.S4: Time series of NPP anomalies including the MODIS and Landsat derived NPP calculated with respiration as a fixed ratio (50%) of GPP. Using the fixed ratio approach, large anomalies in NPP are reduced for both the MODIS and Landsat derived datasets.

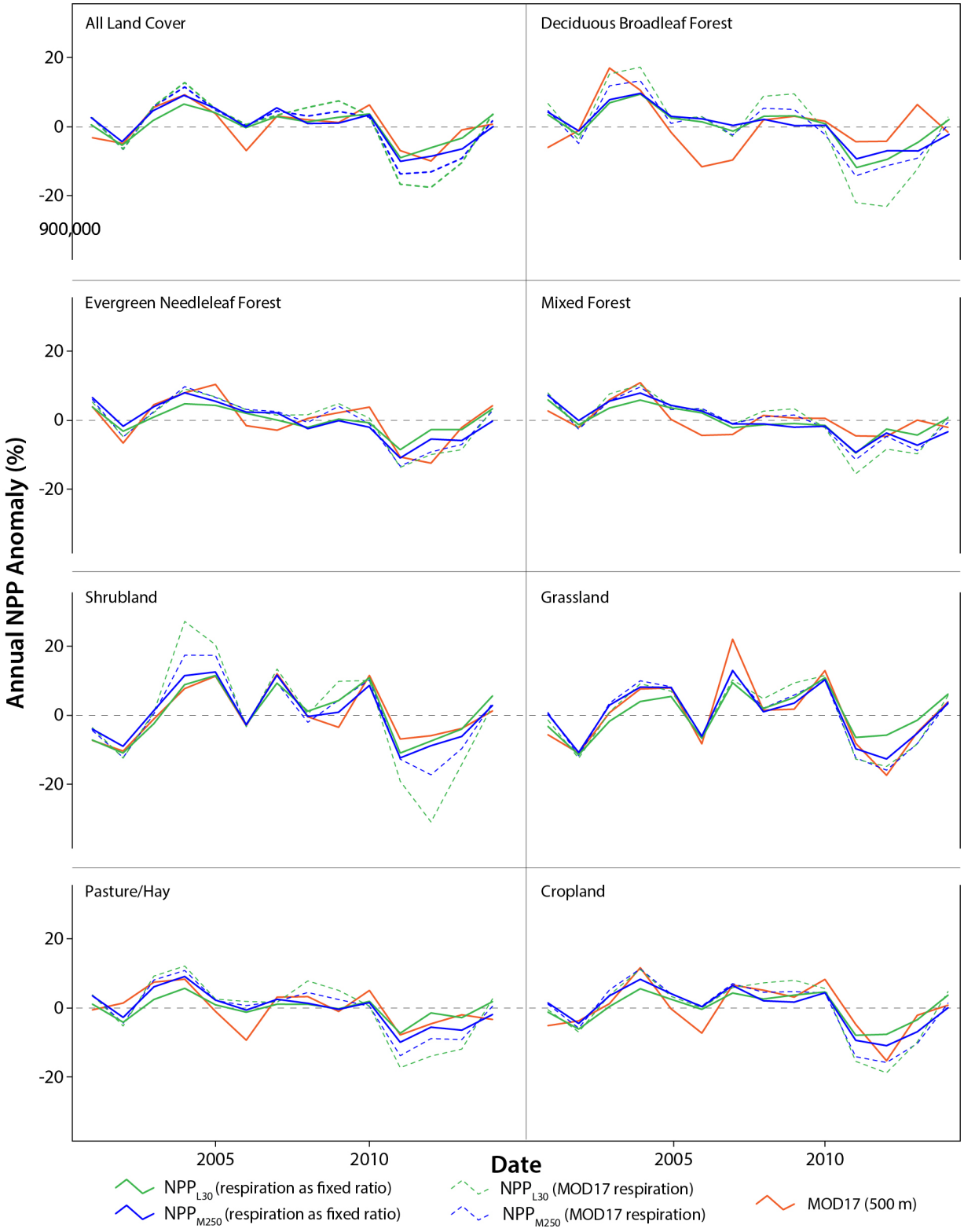

CHAPTER 3: OWNERSHIP DYNAMICS OF TERRESTRIAL PRODUCTION ACROSS THE CONTERMINOUS UNITED STATES: IMPLICATIONS FOR CONSERVATION

3.1 Introduction

Within the conterminous United States (CONUS), public land across federal, state, and local jurisdictions accounts for over 450 million acres (~ 30% total land area), the remainder predominantly under private ownership, with a small fraction (~ 2%) under Native American jurisdiction. The resulting landscape–particularly in the western US–is often a mosaic of ownership, with varying ranges of management objectives and protection levels, that may or may not correspond to underlying ecological patterns or processes. As the predominant conservation paradigm operating in the United States centers around the network of public lands (Knight, 1999; Scott *et al.*, 2001), including national parks, forests, and wildlife refuges, it is critical to assess and understand the extent to which public lands conserve key components.

Quantifiable and meaningful metrics of ecosystem structure and function are not readily available at broad spatio-temporal scales. Many conservation assessments focus on narrowly defined questions across limited spatio-temporal scales, resulting in management actions that are therefore narrow and limited in scope (Hiers *et al.*, 2016). For example, assessments often rely on single metrics, like biodiversity, demonstrating that public lands do not adequately cover the distributions or requirements of key threatened or endangered species (Groves *et al.*, 2000; Jenkins *et al.*, 2015). Subsequent policy, management, and conservation actions follow suit and result in overly precise prescriptions–often confined to the specific species of concern–failing to account for broader ecological processes. A critical and expanding area of research is the development of quantifiable variables across broad spatio-temporal scales that relate to key ecological processes and ecosystem functions (Maron *et al.*, 2015). Compelling

approaches integrate satellite remote sensing (SRS) data and process-based models to produce datasets of relevant biological variables (Pereira *et al.*, 2013). Terrestrial net primary production (NPP) is a key biological variable that can be modelled using SRS data (Potter *et al.*, 1993; Running *et al.*, 2000).

NPP is a fundamental component of the carbon cycle, marking the sequestration of CO_2 into biomass through photosynthesis (Roy *et al.*, 2001). As the entry point of carbon into ecosystems and the ultimate source of energy for all terrestrial species, NPP is linked not just to biodiversity across trophic levels, but is a supporting ecosystem service that is necessary for the production of all other ecosystem services (Field *et al.*, 1995; Loreau *et al.*, 2001). Largely controlled by climate, land cover, disturbance regime, and land-use practices, NPP is highly variable across space and time and is easily influenced by human activity (Piao *et al.*, 2009). SRS derived estimates of terrestrial NPP and can be applied toward defining healthy ecosystem function (Costanza & Mageau, 1999), for assessing change and degradation across landscapes (Running *et al.*, 2004), quantifying broader cumulative effects of landuse and management practices (Allred *et al.*, 2015), and implementing effective conservation strategies (Turner *et al.*, 2003).

Given the need for essential metrics across broad spatio-temporal scales and the fundamental role of NPP, we use NPP to examine the effectiveness of the public land system in conserving ecosystem structure and function. Despite the substantial amount of public land within CONUS, its distribution is unequal and acreage increases from east to west. Production–largely driven by rainfall patterns at the continental scale–follows an opposite course and generally increases from the west to east (Figure 3.1). This inverse relationship, of production to public land acreage, is the direct result of historic policies

that drove settlement of the United States, whereby lands best suited for agriculture and industry (i.e., the most productive) were settled and transferred out of the public domain (Scott *et al.*, 2001). The premise that public lands tend to represent the least productive areas across CONUS has long been surmised, particularly for rangelands. We are the first to actually quantify this. The objectives of this paper are twofold: first, we examine ownership patterns of America's terrestrial production. Second, we examine the role of the public lands system in conserving America's terrestrial production and ensuing ecological processes and ecosystem services. The production-ownership relationship highlights key challenges and opportunities for conservation in the United States, providing a strong basis for programs and actions to be integrated across land ownership.

3.2 Methods

3.2.1 DATA

To examine production-ownership relationships, we utilized a new high resolution NPP dataset specifically developed for CONUS (Robinson et al. 2017). This dataset, adapted from the global MOD17 NPP model (Running & Zhao, 2015), incorporates high resolution (30 m) Landsat estimates of vegetation dynamics, along with high resolution land cover and meteorological datasets specific to CONUS. These improvements produce a dataset well suited for monitoring the spatio-temporal variability of NPP across ownership, land-use, and management regimes at ecologically relevant scales. We obtained land ownership from the Protected Areas Database of the US (PAD-US CBI edition, version 2), a GIS dataset containing polygons of land ownership across CONUS, designated as federal, state, local, tribal, and private (The Conservation Biology Institute, 2012). We classified ownership into three broad categories: public (aggregating federal,

state, and municipal ownership), tribal (Native American reservations) and private. The PAD-US represents ownership as of 2016; we assumed the transfer of land across the three major categories to be minimal during our study period (1993 to 2016).

We used the 30 m National Land Cover Database (NLCD) (Homer *et al.*, 2007, 2015; Fry *et al.*, 2011) to disaggregate production-ownership results by dominant land cover class. We aggregated evergreen, deciduous, and mixed forests into a single forest category, and shrublands and grasslands into a single rangeland category. Croplands, pasture/hay, and built-up (e.g., urban) areas were excluded from the analysis. For a given year, we used land cover from the closest subsequent NLCD year (2001, 2006, or 2011). To compare production- ownership results across similar ecoclimate zones, we utilized the Level I Ecoregions of North America (hereafter ecoregions) (Omernik & Griffith, 2014).

3.2.2 MULTI-SCALE ANALYSIS

To explore our first objective of overall ownership patterns of terrestrial production across CONUS, we calculated total production and average productivity annually from 1993 to 2016 for each ownership category at the CONUS scale. Total production is the cumulative amount of carbon allocated to plant tissue annually over a given area, often measured in Pg (10^{15}) of carbon, while average productivity is the mean rate of allocation over a given area (kg C m^{-2} y^{-1}). We used linear regression to determine temporal trends in both total production and average productivity. We also calculate a deviation metric, the percent departure from expected production or PDE, quantifying the degree to which total production for each ownership category and land cover class departs from the expected amount of production given the relative areas (Equation 1).

$$PDE = \frac{NPP_{owner_i lc_j}}{NPP_{total}} - \frac{Area_{owner_i lc_j}}{Area_{total}} \; x \; 100 \qquad (1)$$

Positive values indicate that total production is higher than expected for a given ownership class and land cover based on the area, while negative values indicate the opposite.

To explore our second objective of assessing the role of public lands in conserving production, we quantified the ownership-production relationships at both the state and ecoregion scales. Dynamics at the state scale are important, as states represent relevant jurisdictional boundaries for both private and public land. Comparisons within ecoregions restrict analysis to ecologically similar areas and may highlight dynamics that are not apparent at the broader CONUS scale. We used Spearman's rank-order correlation analysis to test for a correlation between the acreage of public lands and the average productivity of the public lands. At the state scale, this analysis is aggregated across land covers (forest and rangeland) while at the ecoregion scale it is disaggregated by land cover. At the ecoregion scale, we also calculated the total production, average productivity, trends from 1993 to 2016, and the PDE metric for ownership category and land cover class. Using finer resolution Level IV ecoregions, we calculated and mapped the PDE metric for private lands across for forests and rangelands. All analyses were done in Google Earth Engine (Gorelick *et al.*, 2016) and R (R Core Team, 2015).

3.3 Results

Across CONUS private lands exhibit both higher total production and higher average productivity than public and tribal lands (Figure 3.2, Table 3.1). Production on privately

owned rangelands and forests accounts for approximately 67.3% (1.310 Pg C) of forest and rangeland NPP across CONUS, while production on public and tribal forests and rangelands accounts for 30.4% (0.591 Pg C) and 2.4% (0.046 Pg C) respectively. Average productivity of forests and rangelands is also substantially higher on private land than on public and and tribal land (0.455, 0.323, and 0.234 kg C m^{-2} y^{-1}, respectively). Disaggregating by land cover yields similar results, with the exception of rangelands, where tribal ownership exhibits higher average productivity than public ownership (Table 3.1). Additionally, PDE across CONUS reveals that privately owned land have 8.5% more total production than expected, given their respective area, while public and tribal land show less than expected production (-6.9% and -1.6% respectively). By land cover, private forests across CONUS are 3.2% more productive than expected while private rangelands are 14.1% more productive than expected. Public and tribal forests show less than expected production (-2.8% and -0.4%, respectively) as do public and tribal rangelands (-13.2% and -0.9%, respectively).

At the state level there is a significant inverse relationship between the total area and the average productivity of public land (Figure 3.3a; $\rho = -0.53$; $p < 0.01$). This trends also occurs for rangelands at the ecoregion scale (Figure 3.3c; $\rho = -0.79$; $p \leq 0.01$) but is not evident for forests (Figure 3.3b; $\rho = 0.082$; $p = 0.72$). Average productivity across forests and rangelands is higher on private than on public lands within most ecoregions (Table 3.1). Eastern Temperate Forests, Southern Semi-Arid Highlands, and Temperate Sierras are the only ecoregions where productivity of public forests exceeds that of private forests. Likewise, productivity on public rangelands exceeds private rangelands in Marine West Coast Forests and Eastern Temperate Forests. Rangeland productivity on tribal

lands exceeds that of private and public lands within the Temperate Sierras, Southern Semi-Arid Highlands, Great Plains, and Eastern Temperate Forests. Total production across tribal lands, however, remains less that private and public lands simply due to total area. These dynamics are similarly reflected in the PDE.

Within the CONUS domain, moderate trends were in total production and average productivity were present for some land covers. Private forests experienced a moderate decline in total production over the time period (slope = -0.0004 Pg C y^{-1}; $p = 0.14$) while public forests increased in average productivity (slope = 0.002 kg C $m^{-2} y^{-1}$; $p \leq 0.05$). At the ecoregion scale, two dominantly forested ecoregions appear to be driving the decrease in private forest total production, Marine West Coast Forest (slope = -0.0002 Pg C y^{-1}; $p \leq 0.01$) and Eastern Temperate Forests (slope = -0.000341 Pg C y^{-1}; $p \leq 0.10$). The increasing trend in the average productivity in public forests can be attributed to Northern Forests (slope = 0.003 kg C $m^{-2} y^{-1}$; $p \leq 0.05$), Northwestern Forested Mountains (slope = 0.003 kg C $m^{-2} y^{-1}$; $p \leq 0.01$), and Marine West Coast Forests (slope = 0.003 kg C $m^{-2} y^{-1}$; $p \leq 0.05$).

3.4 Discussion

Public lands are a central feature of the American conservation paradigm. Wilderness areas, national and state parks, wildlife refuges, national forests, and other publically owned lands are invaluable assets, conserving vast amounts of acreage and ecosystem structure and function. Public lands however, are only a portion a broader mosaic of land ownership, all with varying degrees of conservation value. Across CONUS, the vast majority of this mosaic is privately owned with considerable conservation value but

minimal conservation incentive or protection (Knight, 1999). The need for the integration of private lands into the broader conservation paradigm is well recognized, simply due to acreage and distribution (Groves *et al.*, 2000; Scott *et al.*, 2001; Donnelly *et al.*, 2016). Our analysis of the ownership of terrestrial production adds compelling evidence to this discussion. As a supporting ecosystem service, terrestrial production is necessary for the production of all other ecosystem services, and thus the ownership–and ultimately management and responsibility–of terrestrial production is a critical component of broader ecosystem sustainability.

Total production on private forests and rangelands across CONUS is more than double that of production on public and tribal lands combined. While not entirely unexpected, subtle dynamics highlight key points for ecological conservation. Not only does total production of private lands exceed that of public and tribal lands, average productivity is likewise greater; 13 and 32% greater across forests and 83 and 46% greater across rangelands, for public and tribal lands, respectively. When focusing on the ecoregions of the western United States, where public lands are predominant, the average productivity of private lands exceeds that of public lands for nearly every ecoregion (Table 3.1). Despite total production being greater on public lands (simply due to area), the most productive land is generally in the private domain, while the least productive is in the public domain. At the state scale, there is a clear inverse association between the total acreage of public land and its productivity (Figure 3.3a). This dynamic largely relates to the historic processes which drove the settlement of the country, where land suitable for agriculture and industry (i.e., most of the eastern United States and select areas in

proximity to water and with good soils in the western United States) were privatized first (Scott *et al.*, 2001).

The extent to which private land is disproportionately associated with higher productivity is especially apparent across western rangelands (Figures 3.3c, 3.4b). Although discussed and surmised for many years, we are the first to quantify that private rangelands are indeed more productive than public rangelands. While variable, productivity can be 2 to 42% greater on private lands, suggesting that despite the vast acreage of western rangelands in the public domain, rangelands under private ownership are vital components of the ecological processes and ecosystem services that rangelands provide. Across the arid and semi-arid rangelands that are characteristic of the American west, these areas of higher productivity are often associated with water availability and higher quality soils, and have a disproportionate importance for broader ecological processes given their area within the landscape (Patten, 1998; McKinstry *et al.*, 2004). Productive rangelands are critical for both wildlife and livestock, providing heterogeneity to the landscape (Fuhlendorf & Engle, 2001), are key to maintaining rangeland resilience (Bestelmeyer & Briske, 2012), and serving as critical microrefugia for drought, fire, climate change, and harsh winters (Berry *et al.*, 2007; Mackey *et al.*, 2012).

Average productivity of tribal rangelands exceeded that of private and public productivity across Great Plains, Southern Semi-Arid Highlands, Temperate Sierras, and Eastern Temperate Forests ecoregions. The greater productivity found on these tribal rangelands may arise from integration into an innovative ecosystem management scheme (Liu *et al.*, 2007) or from a lack of mechanisms and incentives to develop or alter tribal land, which are more substantial on surrounding privately and publically owned lands (McNeeley,

2017). As with private rangelands, tribal rangelands contribute to the overall heterogeneity of rangelands across the ecological mosaic. Heterogeneity at these scales is an integral component of maintaining rangeland resilience (Fuhlendorf *et al.*, 2012), and is shown through the lack of significant trends in either production or productivity. Ownership classes capture constituent parts of this heterogeneity, prompting the need for rangeland conservation paradigms to reflect this.

Through examining the ownership-production relationship across CONUS, it is clear that maintaining terrestrial production–which is vital for conserving broader ecological processes and ecosystem functions–is not simply about conserving acreage. The United States public lands system is invaluable, conserving vast acreage, particularly across the western states; yet it insufficiently conserves production in the eastern United States and key areas of productivity in the western United States. Incorporating strategies of both private and tribal land conservation into broader conservation paradigms will be critical to maintain fundamental ecosystem functions such as terrestrial production. Developing conservation strategies on private lands presents unique challenges, as private landowners, whether individual or corporate, hold substantial liberties to manage land as they see fit. Management actions can be driven by a suite of factors, and are more often than not socio-economic rather than ecological. For example, the western United States continues substantial growth and development due to rapid population influxes (Maestas *et al.*, 2001), resulting in subdivision, expanding exurban growth, and added pressure on privately held areas of high productivity. Across the eastern United States, current rates of forest loss are approximately 2.5 times greater than the national average (Drummond & Loveland, 2010), mostly occurring on private land and resulting in net losses of forest

cover and subsequently total production. Except under certain regulatory circumstances (e.g., endangered species, hazardous or toxic substances), little can be done through policy or regulation to broadly implement conservation strategies that function across private and public lands.

Primary production is one of America's greatest natural assets, providing the foundation for numerous ecosystem services, biodiversity, and habitat. The majority of production across the conterminous United States occurs in the private domain. Despite challenges, private land conservation presents unique opportunities for partnerships, innovative solutions, and perhaps more sustainable outcomes built on consensus and choice (Endicott, 1993). These solutions can be more readily contextualized to both local ecological and socio-economic conditions than imposed regulatory solutions (Morrisette, 2001). They can be applied beyond single species or single metric approaches to incorporate ecosystem services, landscape heterogeneity, and key resource areas (Villamagna *et al.*, 2015), all of which can be measured and monitored through production dynamics (Running *et al.*, 2004). Furthermore, these solutions often connect with people's livelihoods, creating mutually beneficial outcomes for both conservation and private landowners (Endicott, 1993; Morrisette, 2001). Many of these partnerships, programs, and solutions are already being implemented across the United States with exceptional results. For example, the Natural Resources Conservation Service (NRCS) led Sage Grouse Initiative, works collaboratively with private landowners and partners across the western United States to improve rangeland productivity and Greater sage-grouse (*Centrocercus urophasianus*) habitat while maintaining economic viability of the landscape. The success of this initiative was a major contributor to the "unprecedented

conservation cooperation" (White House 2015) that ensured the Greater sage-grouse was not listed under the Endangered Species Act. Conservation efforts that cross ownership boundaries and integrate working landscapes can improve our broader conservation paradigm to not only conserve biodiversity, habitat, and species, but also the key ecological functions and processes on which they depend.

3.5 References

Allred BW, Smith WK, Twidwell D, Haggerty JH, Running SW, Naugle DE, Fuhlendorf SD (2015) Ecosystem services lost to oil and gas in North America. *Science*, **348**, 401–402.

Berry S, Mackey B, Brown T (2007) Potential applications of remotely sensed vegetation greenness to habitat analysis and the conservation of dispersive fauna. *Pacific Conservation Biology*, **13**, 120–127.

Bestelmeyer BT, Briske DD (2012) Grand challenges for resilience-based management of rangelands. *Rangeland Ecology & Management*, **65**, 654–663.

Costanza R, Mageau M (1999) What is a healthy ecosystem? *Aquatic Ecology*, **33**, 105–115.

Donnelly JP, Naugle DE, Hagen CA, Maestas JD (2016) Public lands and private waters: scarce mesic resources structure land tenure and sage-grouse distributions. *Ecosphere*, **7**.

Drummond MA, Loveland TR (2010) Land-use pressure and a transition to forest-cover loss in the eastern united states. *Bioscience*, **60**, 286–298.

Endicott E (1993) Land Conservation Through Public/Private Partnerships. Island Press.

Field CB, Randerson JT, Malmström CM (1995) Global net primary production: Combining ecology and remote sensing. *Remote Sensing of Environment*, **51**, 74–88.

Fry JA, Xian G, Jin S et al. (2011) Completion of the 2006 national land cover database for the conterminous United States. *Photogrammetric Engineering and Remote Sensing*, **77**, 858–864.

Fuhlendorf SD, Engle DM (2001) Restoring heterogeneity on rangelands: ecosystem management based on evolutionary grazing patterns. *Bioscience*, **51**, 625–632.

Fuhlendorf SD, Engle DM, Elmore RD, Limb RF, Bidwell TG (2012) Conservation of pattern and process: developing an alternative paradigm of rangeland management. *Rangeland Ecology & Management*, **65**, 579–589.

Gorelick N, Hancher M, Dixon M, Ilyushchenko S, Thau D, Moore R (2017) Google Earth Engine: Planetary-scale geospatial analysis for everyone. *Remote Sensing of Environment, **2016***.

Groves CR, Kutner LS, Stoms DM et al. (2000) Owning up to our responsibilities: Who owns lands important for biodiversity? In: *Precious Heritage: The Status of Biodiversity in the United States* (eds Stein BA, Kutner LS, Adams JS), pp. 275–300. Oxford University Press.

Hiers JK, Jackson ST, Hobbs RJ, Bernhardt ES, Valentine LE (2016) The precision problem in conservation and restoration. *Trends in Ecology & Evolution*, **31,** 820-830.

Homer C, Dewitz J, Fry J et al. (2007) Completion of the 2001 national land cover database for the counterminous United States. *Photogrammetric Engineering and Remote Sensing*, **73**, 337.

Homer CG, Dewitz JA, Yang L et al. (2015) Completion of the 2011 National Land Cover Database for the conterminous United States-Representing a decade of land cover change information. *Photogrammetric Engineering and Remote Sensing*, **81**, 345–354.

Jenkins CN, Van Houtan KS, Pimm SL, Sexton JO (2015) US protected lands mismatch biodiversity priorities. *Proceedings of the National Academy of Sciences of the United States of America*, **112**, 5081–5086.

Knight RL (1999) Private Lands: The Neglected Geography. *Conservation Biology*, **13**, 223–224.

Liu J, Dietz T, Carpenter SR et al. (2007) Complexity of coupled human and natural systems. *Science*, **317**, 1513–1516.

Loreau M, Naeem S, Inchausti P et al. (2001) Biodiversity and ecosystem functioning: current knowledge and future challenges. *Science*, **294**, 804–808.

Mackey B, Berry S, Hugh S, Ferrier S, Harwood TD, Williams KJ (2012) Ecosystem greenspots: identifying potential drought, fire, and climate-change micro-refuges. *Ecological Applications*, **22**, 1852–1864.

Maestas JD, Knight RL, Gilgert WC (2001) Biodiversity and land-use change in the American mountain west. *Geographical Review*, **91**, 509–524.

Maron M, Gordon A, Mackey BG (2015) Agree on biodiversity metrics to track from space. *Nature*, **523**, 403–405.

McKinstry MC, Hubert WA, Anderson SH (2004) *Wetland and Riparian Areas of the Intermountain West: Ecology and Management*. University of Texas Press, Austin.

McNeeley SM (2017) Sustainable Climate Change Adaptation in Indian Country. *Weather, Climate, and Society*, **9**, 393–404.

Morrisette PM (2001) Conservation easements and the public good: Preserving the environment on private lands. *Natural Resources Journal*, **41**, 373–426.

Omernik JM, Griffith GE (2014) Ecoregions of the conterminous United States: evolution of a hierarchical spatial framework. *Environmental Management*, **54**, 1249–1266.

Patten DT (1998) Riparian ecosytems of semi-arid North America: Diversity and human impacts. *Wetlands*, **18**, 498–512.

Pereira HM, Ferrier S, Walters M et al. (2013) Ecology. Essential biodiversity variables. *Science*, **339**, 277–278.

Piao S, Ciais P, Friedlingstein P, de Noblet-Ducoudré N, Cadule P, Viovy N, Wang T (2009) Spatiotemporal patterns of terrestrial carbon cycle during the 20th century. *Global Biogeochemical Cycles*, **23**.

Potter CS, Randerson JT, Field CB, Matson PA, Vitousek PM, Mooney HA, Klooster SA (1993) Terrestrial ecosystem production: a process model based on global satellite and surface data. *Global Biogeochemical Cycles*, **7**.

R Core Team (2015) R: A language and environment for statistical computing.

Roy J, Mooney HA, Saugier B (2001) *Terrestrial Global Productivity*. Academic Press.

Running SW, Zhao M (2015) *MOD17 Users Guide 2015*. Numerical Terradynamic Simulation Group.

Running SW, Thornton PE, Nemani R, Glassy JM (2000) Global terrestrial gross and net primary productivity from the earth observing system. In: *Methods in Ecosystem Science*, pp. 44–57. Springer New York.

Running SW, Nemani RR, Heinsch FA, Zhao M, Reeves M, Hashimoto H (2004) A continuous satellite-derived measure of global terrestrial primary production. *Bioscience*, **54**, 547–560.

Scott JM, Davis FW, McGhie RG, Wright RG, Groves C, Estes J (2001) Nature reserves: do they capture the full range of America's biological diversity? *Ecological Applications*, **11**, 999–1007.

The Conservation Biology Institute (2012) PAD-US (CBI Edition) Version 2.

Turner W, Spector S, Gardiner N, Fladeland M, Sterling E, Steininger M (2003) Remote sensing for biodiversity science and conservation. *Trends in Ecology & Evolution*, **18**, 306–314.

Villamagna A, Scott L, Gillespie J (2015) Collateral benefits from public and private conservation lands: a comparison of ecosystem service capacities. *Environmental conservation*, **42**, 204–215.

Robinson, N., B.W. Allred, W.K. Smith, M.O. Jones, A. Moreno, T.A. Erickson, D.E. Naugle, & S.W. Running. In Review. Landsat 30 m and MODIS 250 m derived terrestrial primary production for the conterminous United States. Remote Sensing in Ecology and Conservation.

White House. 2015, September 22. Unprecedented Collaboration to Save Sage-Grouse is the Largest Wildlife Conservation Effort in U.S. https://obamawhitehouse.archives.gov/blog/2015/09/22/unprecedented-collaboration-save-sage-grouse-largest-wildlife-conservation-effort-us.

3.6 Tables

Table 3.1: Total production, average productivity, trends and p-values, and PDE for forests and rangelands across CONUS and for level I ecoregions.

	Forests							Rangelands						
	Total Production (billions kg C y^{-1})			Average Productivity (kg C m^{-2} y-1)				Total Production (billions kg C y^{-1})			Average Productivity (kg C m^{-2} y-1)			
Ecoregion & Ownership	Mean	Slope	p-value	Mean	Slope	p-value	PDE	Mean	Slope	p-value	Mean	Slope	p-value	PDE
CONUS														
Public	458.35	0.5966	0.45	0.65	0.0018	0.11	-2.82	132.58	0.3395	0.46	0.12	0.0002	0.63	-13.17
Private	932.82	-3.7612	0.14	0.74	-0.0013	0.51	3.22	361.11	-0.0045	1.00	0.22	-0.0003	0.70	14.05
Native American	22.68	-0.0005	0.99	0.56	0.0012	0.26	-0.40	23.49	0.0668	0.42	0.15	0.0004	0.50	-0.88
5. Northern Forests														
Public	55.28	0.1504	0.12	0.74	0.0027	0.04	-0.11	2.05	0.0223	0.00	0.34	0.0002	0.83	-0.44
Private	104.16	0.3306	0.04	0.75	0.0029	0.01	0.13	5.06	0.0433	0.00	0.35	0.0009	0.21	0.43
Native American	1.37	0.0004	0.91	0.73	0.0011	0.54	-0.02	0.05	0.0006	0.01	0.35	-0.0006	0.60	0.00
6. Northwestern Forested Mountains														
Public	218.97	0.7076	0.07	0.62	0.0031	0.01	-0.96	37.39	0.2874	0.00	0.21	0.0009	0.09	-2.68
Private	64.55	-0.0706	0.54	0.65	0.0015	0.19	0.91	26.83	0.1305	0.09	0.23	0.0005	0.43	2.54
Native American	8.76	-0.0066	0.67	0.64	0.0018	0.11	0.05	2.31	0.0173	0.01	0.23	0.0006	0.34	0.14
7. Marine West Coast Forests														
Public	20.60	0.0190	0.42	1.11	0.0027	0.03	-0.24	1.15	0.0147	0.00	0.56	-0.0004	0.56	0.27
Private	32.35	-0.1618	0.00	1.12	0.0030	0.01	0.27	5.98	0.1185	0.00	0.55	-0.0009	0.18	-0.27
Native American	1.07	-0.0019	0.22	1.10	0.0021	0.15	-0.03	0.15	0.0022	0.00	0.55	0.0008	0.35	0.00
8. Eastern Temperate Forests														
Public	98.46	-0.2929	0.29	0.80	-0.0016	0.47	0.60	3.18	0.0106	0.33	0.33	-0.0026	0.03	0.37
Private	659.05	-3.4096	0.10	0.76	-0.0022	0.36	-0.60	50.76	0.0612	0.78	0.31	-0.0030	0.02	-0.38
Native American	0.87	-0.0018	0.48	0.77	-0.0004	0.87	0.00	0.03	0.0006	0.00	0.36	0.0004	0.71	0.01
9. Great Plains														
Public	5.15	-0.0295	0.21	0.50	-0.0018	0.44	-0.94	23.41	0.0345	0.66	0.20	0.0003	0.66	-1.58
Private	54.38	-0.4527	0.18	0.57	-0.0038	0.29	1.14	221.57	-0.3008	0.74	0.24	-0.0003	0.79	0.98
Native American	1.17	-0.0015	0.73	0.49	0.0001	0.95	-0.20	13.15	0.0306	0.50	0.26	0.0006	0.49	0.60
10. North American Deserts														
Public	28.15	0.0627	0.32	0.38	0.0013	0.13	-1.36	52.11	-0.0174	0.95	0.07	0.0000	0.94	-6.16
Private	6.31	0.0143	0.37	0.43	0.0012	0.27	1.78	28.61	0.0075	0.96	0.10	0.0001	0.90	6.51
Native American	2.99	0.0021	0.78	0.36	0.0006	0.49	-0.42	6.57	0.0102	0.75	0.07	0.0001	0.76	-0.36
11. Mediterranean California														
Public	6.95	-0.0208	0.08	0.90	-0.0024	0.11	-0.15	7.20	-0.0433	0.06	0.33	-0.0019	0.07	-1.74
Private	9.50	-0.0124	0.52	0.91	-0.0007	0.71	0.22	19.58	-0.0686	0.23	0.36	-0.0011	0.30	1.89
Native American	0.12	-0.0003	0.33	0.82	-0.0017	0.40	-0.07	0.22	-0.0009	0.28	0.29	-0.0012	0.29	-0.14
12. Southern Semi-Arid Highlands														
Public	1.87	-0.0168	0.00	0.64	-0.0018	0.24	1.72	1.77	0.0009	0.95	0.08	0.0000	0.97	-1.70
Private	0.11	-0.0005	0.11	0.52	-0.0015	0.31	-1.00	0.89	-0.0005	0.94	0.09	0.0000	0.97	0.44
Native American	0.11	-0.0005	0.14	0.55	0.0009	0.57	-0.72	0.27	0.0007	0.76	0.10	0.0002	0.80	1.25
13. Temperate Sierras														
Public	22.69	0.0173	0.74	0.54	0.0013	0.29	1.16	4.28	0.0298	0.17	0.13	0.0006	0.34	-1.60
Private	2.39	0.0014	0.80	0.45	0.0006	0.53	-1.47	1.80	0.0045	0.57	0.14	0.0003	0.57	0.39
Native American	6.22	0.0095	0.53	0.54	0.0016	0.24	0.31	0.74	0.0056	0.12	0.15	0.0007	0.37	1.21
14. Tropical Wet Forests														
Public	0.22	-0.0003	0.61	0.80	-0.0013	0.54	-0.02	0.03	-0.0002	0.16	0.38	-0.0020	0.15	-2.81
Private	0.02	-0.0001	0.28	0.80	-0.0018	0.38	0.03	0.03	-0.0001	0.17	0.42	-0.0010	0.37	2.81
Native American	0.00	0.0000	0.98	0.71	-0.0001	0.98	-0.01	0.00	0.0000	0.03	0.34	-0.0030	0.03	-0.01

3.7 Figures

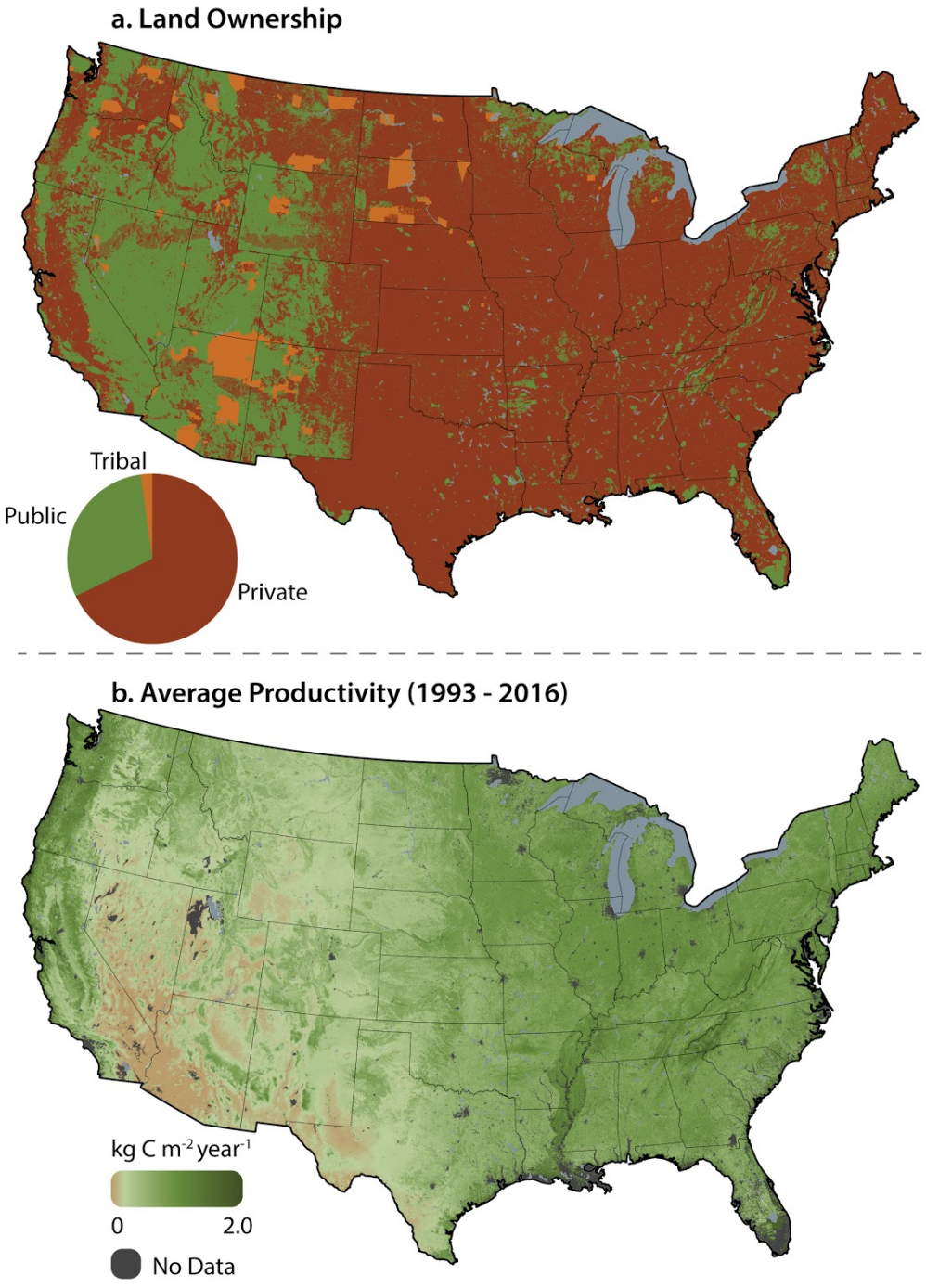
a. Land Ownership
Tribal
Public
Private
b. Average Productivity (1993 - 2016)
kg C m-2 year-1
0
2.0
No Data

Figure 3.1: Ownership categories across CONUS (a.) and average total annual production from 1993 to 2016 (b.). There is a distinct inverse longitudinal pattern of public land acreage and total production.

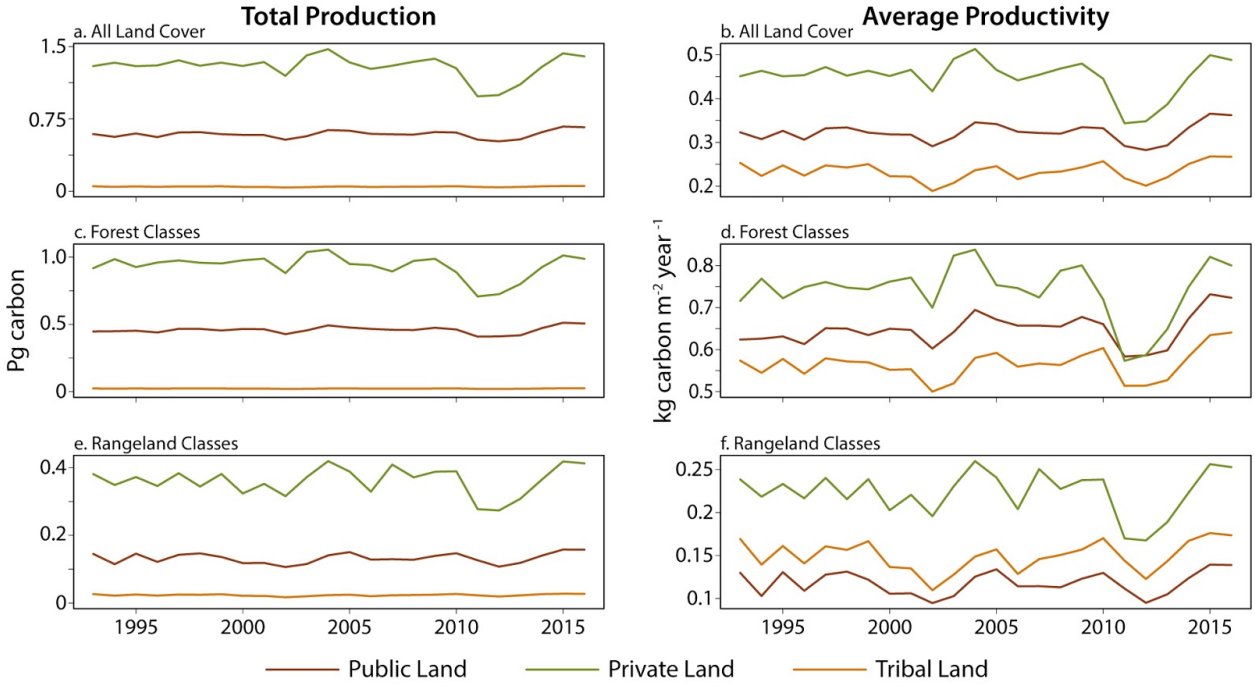

Figure 3.2: Time series plots of total production and average productivity across CONUS from 1993 to 2016 for land cover classes combined (a. and b.), forest classes (c. and d.), and rangeland classes (e. and f.). Total production and and average productivity on private lands is higher in all cases. Despite noticeable interannual variability, there are no significant temporal trends at the CONUS scale.

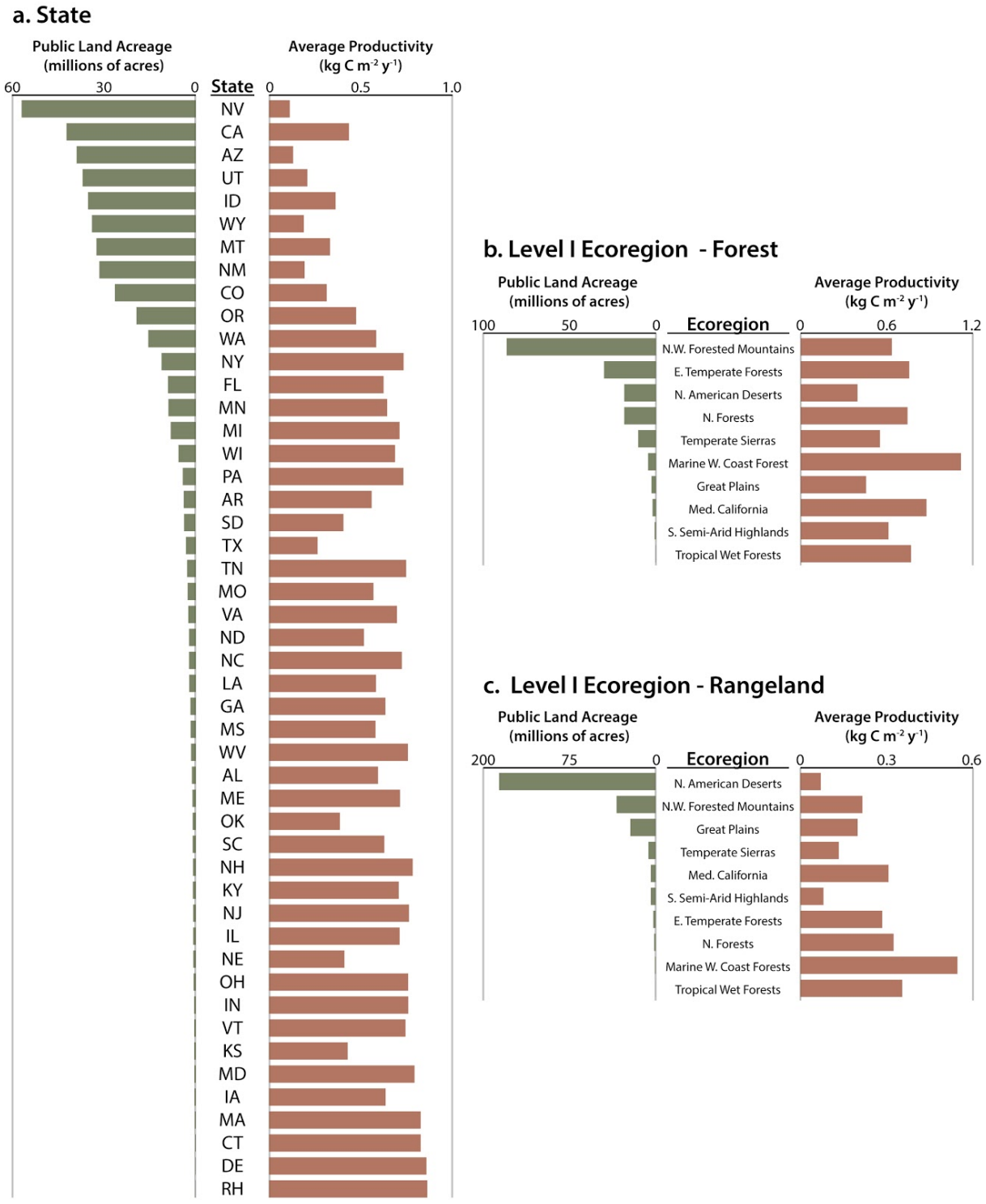

Figure 3.3: Ranking of public land acreage by state (a.), level I ecoregion forests (b.), and level 1 ecoregion rangelands (c.) vs the average productivity across public lands. Spearman's rank correlations (ρ) are significant at the state ($\rho = -0.53$; $p < 0.01$) and for rangeland ecoregion levels ($\rho = -0.79$; $p \leq 0.01$) but not forests ($\rho = 0.082$; $p = 0.72$).

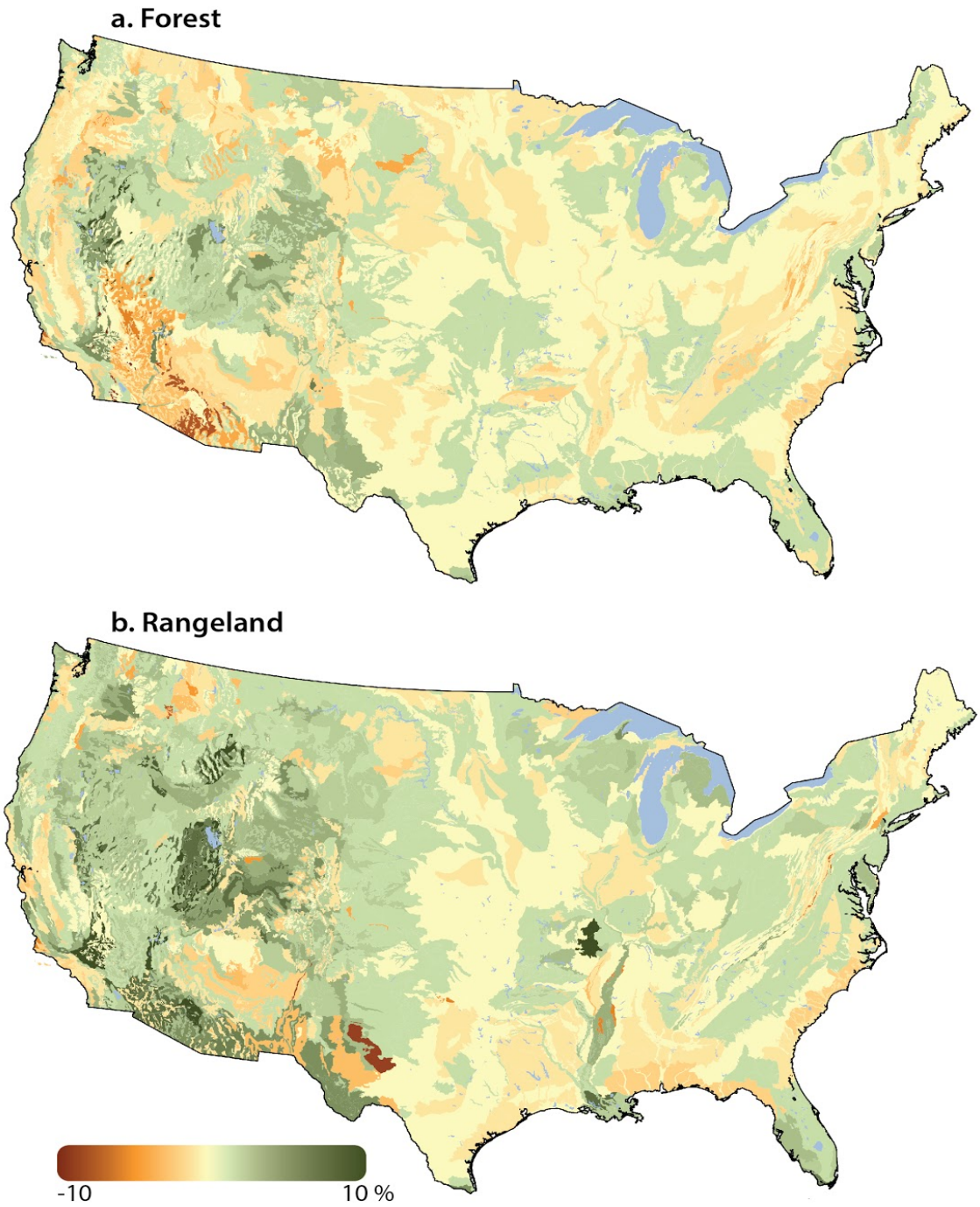

Figure 3.4: Percent departure from expected production (PDE) for private lands across level IV ecoregions for forests (a.) and rangelands (b.). PDE highlights the degree to which total production on private lands departs from the expected production given the respective area.